UNIVERSITY OF CALIFORNIA
RIVERSIDE

First Principles Studies of van der Waals Magnetic and Energy Materials

A Dissertation submitted in partial satisfaction
of the requirements for the degree of

Doctor of Philosophy

in

Electrical Engineering

by

Yuhang Liu

September 2022

Dissertation Committee:

Dr. Roger K. Lake, Co-Chairperson
Dr. Mahesh Raj Neupane, Co-Chairperson
Dr. Sinisa Coh

The Dissertation of Yuhang Liu is approved:

Committee Co-Chairperson

Committee Co-Chairperson

University of California, Riverside

Acknowledgments

I would like to thank my supervisor and mentor Roger K. Lake for his outstanding supervision throughout my PhD and for giving me the opportunity to work in an excellent research environment. I have learned a lot from him about independently doing research, studying new knowledge, and collaborating with others. When I was struggling with my research project, he encouraged me and gave me his insights to overcome the challenges. He has always been very supportive of my academic work and career development. Without his constant support, none of these works would have been possible.

I want to thank my co-advisor Dr. Mahesh Neupane and our collaborator Dr. Juchen Guo for providing me with grants and collaborating with me in doing research. Without your support, my PhD study could not be done easily. I want to thank my committee member Prof. Sinisa Coh, for giving me suggestions to improve my research plan. I would like to thank Dr. Alexander Balandin for all the collaborations with his NDL group. I have learned a lot about the experimental side of nano devices and Raman spectroscopy from Dr. Alexander Balandin and his group. I also want to thank Prof. Ran Cheng, as I have learned much theoretical knowledge from his classes on magnetism.

I would like to express my appreciation to my lab mates in LATTE, Chenyang Li, Nima Djavid, In Jun Park, Rakibul Akanda, Topojit Debnath, Sohee Kwon, and Hector Gomez, for their help and fruitful discussions. I will definitely miss those days we worked together.

I would like to take the opportunity to thank my family for all the support and encouragement over the years. My lovely wife Dr. Xiaoyu Wen, you are also my collaborator

in research and best friend in life. When I feel frustrated, you always give me courage and support me without hesitation. I would not be here without your patient help. I would like to thank my wife's parents for taking good care of Xiaoyu and me. You have saved me a lot of time on housework. Lastly, I would like to thank my parents for their guidance and support.

The text of this dissertation, in part or in full, is a reprint of the material as it appears in the following journal:

- Physical Review Material [1]. Reprinted with permission from [1]. ©[2022]. American Physical Society

The co-author Roger K. Lake, listed in the above publications directed and supervised the research which forms the basis of this dissertation. The remaining co-authors listed provided technical expertise and support as collaborators.

This work has been supported partially by Army Research Lab under the founding Cooperative Agreement (CA) W911NF-16-2-0008. The computational resource was provided by the Extreme Science and Engineering Discovery Environment (XSEDE), which is supported by National Science Foundation Grant No. ACI-1548562 and allocation TG-DMR130081.

To my wife Xiaoyu Wen.

ABSTRACT OF THE DISSERTATION

First Principles Studies of van der Waals Magnetic and Energy Materials

by

Yuhang Liu

Doctor of Philosophy, Graduate Program in Electrical Engineering
University of California, Riverside, September 2022
Dr. Roger K. Lake, Co-Chairperson
Dr. Mahesh Raj Neupane, Co-Chairperson

Two-dimensional chromium ditelluride ($CrTe_2$) is a promising ferromagnetic layered material that exhibits long-range ferromagnetic ordering in the monolayer limit. The formation energies of the different possible structural phases (1T, 1H, 2H) calculated from density functional theory (DFT) show that the 1T phase is the ground state and the energetic transition barriers between the phases, calculated by the nudged elastic band method, are large, on the order of 0.5 eV. The self-consistent Hubbard U correction parameters are calculated for all the phases of $CrTe_2$. The calculated magnetic moment of 1T-$CrTe_2$ with ≥ 2 layers lies in the plane, whereas the magnetic moment of a monolayer is out-of-plane. Band filling and tensile bi-axial strain cause the magnetic moment of a monolayer to switch from out-of-plane to in-plane, and compressive bi-axial strain in a bilayer causes the magnetic moment to switch from in-plane to out-of-plane. The magnetic anisotropy is shown to originate from the large spin orbit coupling (SOC) of the Te atoms and the anisotropy of the exchange coupling constants J_{xy} and J_z in an XXZ type Hamiltonian. Renormalized spin wave theory using experimental values for the magnetic anisotropy energy and Curie

temperatures provides a range of values for the nearest neighbor exchange coupling.

The self-intercalated $Cr_{1+x}Te_2$ is a ferromagnetic layered material with complex structure and magnetic configurations. It is composed of alternating $CrTe_2$ and intercalated Cr layers. The calculated formation energies show that $Cr_{1+x}Te_2$ is more stable when both the top and bottom surfaces are the $CrTe_2$ layers. The exchange coupling constants are extracted by calculating the energies of different magnetic configurations. The direction of magnetic anisotropy depends on the inversion symmetry in $Cr_{1+x}Te_2$. The perpendicular magnetic anisotropy only exists in the structures with broken inversion symmetry. The exchange coupling constant J_1, that is between the intercalated Cr atom and its nearest neighbor Cr atom in the $CrTe_2$ layer, responds to applied strain in different ways in structures with different symmetries.

A systematic theoretical study of dopants in a half-delithiated lithium nickel oxide ($Li_{0.5}NiO_2$) cathode is performed to determine the preferred occupation sites, dopant ion migration, the improvement of structural stability, and the suppression of oxygen evolution. Dopants considered include Li, B, Na, Mg, Al, Si, Ca, Ti, V, Cr, Mn, Fe, Co, Ni, Cu, Zn, Ga, Ge, As, Y, Zr, Nb, Mo, In, Sn, Sb, La, Ce, Ta, and W. For the non-transition metal dopants, the energy barrier governing dopant migration is correlated with the number of valence shell electrons, so that it increases from left to right across a row of the periodic table. For these dopants, the energy barrier also decreases moving down a column of the periodic table. For transition metal dopants, the energy barrier depends on the number of unpaired valence electrons of the dopant, so that the energy barrier is maximum near the middle of a transition metal row. The energy required in oxygen evolution is linearly

correlated with the change in charge of the oxygen resulting from the neighboring dopant ions. In particular, oxygen release is enhanced most by cobalt doping and suppressed most by boron doping.

Contents

List of Figures

List of Tables

Chapter 1

Motivation

1.1 Objectives

The synthesis of monolayer graphene has brought a research boom in 2D materials due to their exotic electronic properties and potential applications in new generation electronic devices [2, 3, 4]. Among all the 2D materials, the 2D magnets have gained enormous attention [5, 6]. Theoretically, in 2D systems, spontaneous long-range magnetization does not exist at a finite temperature according to the Mermin-Wagner theorem [7]. However, the Mermin-Wagner is based on a 2D isotropic Heisenberg model. When magnetic anisotropy exists in 2D materials, the restriction is lifted. Thus, magnetic anisotropy is the key factor to realize 2D ferromagnetic materials.

The 2D van der Waals (vdW) ferromagnetic materials are an important part of the 2D material family. Their unique electronic and magnetic properties make them promising for spintronics [8]. For example, monolayer CrI_3 has been found to be a ferromagnet with perpendicular magnetic anisotropy [9]. Besides its intrinsic properties, the ferromagnetic-

to-antiferromagnetic transition can be induced by pressure [10, 11]. However, CrI_3's Curie temperature of 45K is much lower than the room temperature of 300K, which has limited its application in spintronics [9]. 1T-$CrTe_2$ is a recently found 2D magnetic material, which has one of the highest Curie temperature 310K among all the 2D magnetic materials [12]. Its ferromagnetism was maintained above 300K in thin films down to 8 nm [13]. The magnetic anisotropy of 1T-$CrTe_2$ has been extensively studied. However, different and contradicting experimental results for 1T-$CrTe_2$'s magnetic anisotropy were obtained from different growth conditions and substrates, which indicates a sensitivity of this material to external perturbations such as strain, band filling, and screening. A systemic study of its magnetic anisotropy under different external perturbations is strongly needed. Another interesting vdW magnetic material $Cr_{1+x}Te_2$ [14, 15] is a self-intercalated transition metal chalcogenide. It is often referred to as its bulk form's chemical formula Cr_2Te_3. With different number of layers and surface layer type, $Cr_{1+x}Te_2$ can stably exist in many different forms, including, Cr_2Te_3 [14, 16, 17, 18], Cr_4Te_5 [19], Cr_5Te_8 [20, 21], $Cr_{5+x}Te_8$ [22], and $Cr_{12-x}Te_{16}$ [23], which are promising room temperature 2D ferromagnet with high Curie temperature ranging between 170 and 350 K. However, the absence of a deeper understanding of its layer-dependent and surface-dependent magnetism has limited its potential for engineering magnetic phases.

Another type of vdW material is the $LiNiO_2$ based cathode material. In the era of all-electric vehicles, the importance of stability, capacity, and safety of batteries has increased continually. However, the performance of a $LiNiO_2$ based cathode is limited by many challenges: cation mixing, phase transition, lattice instability, oxygen release, etc

[24, 25]. Cation doping is a promising approach to improve the stability of $LiNiO_2$ based cathode material [26, 27, 28]. Nevertheless, there is still a lack of systematic theoretical studies on the properties of various dopants in $LiNiO_2$ including the preferred occupation site, dopant ion migration, and the mechanism of dopants to improve structural stability and suppress oxygen evolution.

Thus the main object of this work is to systemically study the structural, electronic, and magnetic properties of 2D magnetic materials including layered $CrTe_2$ and self-intercalated $Cr_{1+x}Te_2$, and the ion migration and oxygen stability in doped $LiNiO_2$ based cathode material.

1.2 Organization

The rest of the dissertation is organized as follows. Chapter 2 presents the theoretical background of density functional theory, magnetism, and phonon dispersion. Chapter 3 presents the 2D ferromagnetic material $CrTe_2$'s structural, electronic, and magnetic properties. Chapter 4 presents the preliminary work on the structural properties, formation energy, and magnetic properties of the self-intercalated magnetic material $Cr_{1+x}Te_2$. Chapter 5 presents the ion migration and oxygen stability in doped $LiNiO_2$ based cathode material. Chapter 6 is a summary of all the interesting findings and an outlook for future work. In the Appendix, the python codes for modeling doped half-delithiated cathode $Li_{0.5}NiO_2$ are documents.

Chapter 2

Theoretical Background

This chapter provides a brief description of the theories and methods used in this thesis. The first part introduces density functional theory (DFT), which has become the most popular tool for the simulation of electronic structure, magnetism, structural stability, and phase transition in solid states. Several fundamental elements of DFT including many body problem, Khon-Sham equation, exchange correlation functionals, pseudopotential, and Hubbard U correction are included in this part. The second part discusses the origin of spin-orbit coupling and its role in magnetic anisotropy. The third part introduces simulating phonon spectra from first principles calculation.

2.1 Density functional theory

2.1.1 Many body problem

Solid state is many-particle system consisting of interacting atomic nuclei and electrons. The most fundamental problem in condensed matter physics is describing a solid

state system using the non-relativistic Schrödinger equation

$$H\Psi = E\Psi \tag{2.1}$$

where Ψ is the total wave function of all ions (including nuclei) and electrons in the system, E is the total energy of the system. H is the Hamiltonian which contains kinetic terms and interaction terms of both nuclei and electrons, it can be expressed as

$$H = -\sum_I \frac{\hbar^2}{2m_I}\nabla_I^2 + \frac{1}{2}\sum_{I\neq J}\frac{Z_I Z_J e^2}{|\mathbf{R}_I - \mathbf{R}_J|} - \sum_i \frac{\hbar^2}{2m_e}\nabla_i^2 + \frac{1}{2}\sum_{i\neq j}\frac{e^2}{|\mathbf{r}_i - \mathbf{r}_j|} - \sum_{i,I}\frac{Z_I e^2}{|\mathbf{R}_I - \mathbf{r}_i|} \tag{2.2}$$

where $\mathbf{R}_I$, $\mathbf{r}_i$ represent the positions of nuclei and electrons, m_I and m_e represent the mass of the nuclei and electrons respectively. Z_I is the atomic number. In this Hamiltonian, the first term is the kinetic energy of all nuclei, the second term is the Coulomb interaction between nuclei, the third term is the kinetic energy of all electrons, the fourth term is the Coulomb interaction between electrons and the last term is the Coulomb interaction between electrons and nuclei.

Solving the exact solution of the Hamiltonian of all nuclei and electrons is almost impossible. The most simple but powerful approximation to be made is the Born-Oppenheimer Approximation. The mass of electron is only 1/1836 of proton mass, so they are much lighter than nuclei and move much faster than nuclei. Therefore the electrons respond almost instantaneously to any movement of nuclei, the nuclei are almost static compared to electrons. This approximation makes it possible to separate the nuclei part from the Hamiltonian and wavefunction. Thus, the Hamiltonian of electrons can be expressed as,

$$H = -\sum_i \frac{\hbar^2}{2m_e}\nabla_i^2 + \frac{1}{2}\sum_{i\neq j}\frac{e^2}{|\mathbf{r}_i - \mathbf{r}_j|} - \sum_{i,I}\frac{Z_I e^2}{|\mathbf{R}_I - \mathbf{r}_i|} \tag{2.3}$$

The problem is simpler to work out the electrons wavefunction $\psi_{\mathbf{R}}(\mathbf{r})$ which is governed by the kinetic energy, electron-electron Coulomb interaction, and the static Coulomb potential field of nuclei. However, this Schrödinger equation is still unsolvable due to the complexity of the electron-electron Coulomb interaction. Thus a better method is needed to describe electrons.

2.1.2 Khon-Sham equation

According to Hohenberg-Kohn theorems [29], an interacting electron in an external potential V_{ext} follows two theorems:

Theorem 1 The external potential V_{ext} can be uniquely determined by the ground state density $n_0(\mathbf{r})$ except for a constant.

Theorem 2 The total energy can be written as a functional of the density E[n($\mathbf{r}$)]. The total energy functional is minimized at the exact ground state electronic density $n_0(\mathbf{r})$.

These theorems do not told us the exact form of the energy functional E[n($\mathbf{r}$)]. Kohn and Sham [30] derive the single-particle Schrödinger equation by the variational principle. Following their approach, We can write the total energy functional E[n] as

$$E[n] = T[n] + \int V_{ext}(\mathbf{r})n(\mathbf{r})d\mathbf{r} + \frac{1}{2}\int \frac{e^2 n(\mathbf{r})n(\mathbf{r}')}{|\mathbf{r}-\mathbf{r}'|}d\mathbf{r}d\mathbf{r}' + E_{xc}[n] \tag{2.4}$$

in which T[n] is the kinetic energy functional of the hypothetical non-interacting electrons, V_{ext} is the external potential due to the nuclei or ions, the third term is the Coulomb (Hartree) energy, and $E_{xc}[n]$ is the exchange-correlation energy which includes all many-body effects. The exchange-correlation part of kinetic energy T_{xc} is included in E_{xc} We can use the variational principle on the total energy functional E[n] and the minimization of the

energy functional results in the Kohn-Sham(KS) equation,

$$\left[-\frac{\hbar^2}{2m}\nabla^2 + V_{eff}(\mathbf{r})\right]\phi_i(\mathbf{r}) = \epsilon_i\phi_i(\mathbf{r}) \tag{2.5}$$

where the effective potential V_{eff} is defined as

$$V_{eff}(\mathbf{r}) = V_{ext}(\mathbf{r}) + \int \frac{e^2 n(\mathbf{r}')}{|\mathbf{r}-\mathbf{r}'|}d\mathbf{r}' + V_{xc}(\mathbf{r}) \tag{2.6}$$

where the exchange-correlation potential is expressed as

$$V_{xc} = \frac{\delta E_{xc}[n]}{\delta n(\mathbf{r})} \tag{2.7}$$

The electron density is expressed as

$$n(\mathbf{r}) = \sum_i^N |\phi_i(\mathbf{r})|^2 \tag{2.8}$$

If the exact form of E_{xc} is known, the ground state energy $E[n_0]$ can be obtained from the Kohn-Sham approach. It should be noted that the eigenvalues ϵ_i of the Kohn-Sham orbital ϕ_i have no significant physical meaning and the sum of these energy eigenvalues does not equal to the total energy but is related as

$$\sum_i^N \epsilon_i = E + \frac{1}{2}\int \frac{e^2 n(\mathbf{r})n(\mathbf{r}')}{|\mathbf{r}-\mathbf{r}'|}d\mathbf{r}d\mathbf{r}' - E_{xc}[n] + \int \frac{\delta E_{xc}[n]}{\delta[n(r)]}n(\mathbf{r})d\mathbf{r} \tag{2.9}$$

2.1.3 Exchange correlation functionals: LSDA and GGA

The DFT theory successfully separates the single particle kinetic energy and the Coulomb (Hartree) energy from the many-body exchange-correlation functional, which can be expressed in many different approaches, such as the local spin density approximation (LSDA) and the generalized gradient approximations (GGA).

Hohenberg and Kohn have suggested the local density approximations in their first DFT paper [29]. They pointed out that electrons in solids can be often considered as homogeneous electron gas. The LDA exchange-correlation functional has a quite simple form.

$$E_{xc}^{LDA}[n(\mathbf{r})] = \int n(\mathbf{r})\epsilon_{xc}(n(\mathbf{r}))d\mathbf{r} \tag{2.10}$$

Where $\epsilon_{xc}(n)$ represents the exchange-correlation energy density of a homogeneous electron gas with density $n(r)$. The local spin-density approximation (LSDA) is a generalization of LDA formulated in terms of two spin densities $n\uparrow(r)$ and $n\downarrow(r)$.

$$E_{xc}[n_\uparrow, n_\downarrow] = \int n(r)\epsilon_{xc}(n_\uparrow, n_\downarrow)dr \tag{2.11}$$

The exchange-correlation energy E_{xc} can be decomposed into exchange part $E_x[n(r)]$ and correlation part $E_c[n(r)]$

$$E_{xc}[n(r)] = E_x[n(r)] + E_c[n(r)] \tag{2.12}$$

The analytic form of E_x term of homogeneous electron gas can be derived from Dirac's work in 1930 [31].

$$E_x[n(\mathbf{r})] = -k\int n^{\frac{4}{3}}(\mathbf{r})dr \tag{2.13}$$

where $k = \frac{3}{2}(\frac{3}{4\pi})^{\frac{1}{3}}$ for LSDA and $k = 2^{-\frac{1}{3}}\frac{3}{2}(\frac{3}{4\pi})^{\frac{1}{3}}$ for LDA.

In respect of E_c unfortunately we only know analytic expressions for the correlation part $E_c$in the high [32, 33] and low [34] density limits. A commonly used form is the interpolation formula of Perdew and Zunger [35] in which the interpolation coefficients are derived from the data of quantum Monte Carlo of the homogeneous electron gas generated by Ceperley and Alder [36].

Despite LDA's simplicity, it gives good predictions for systems with slowly varying charge densities. Predicted lattice constants by LDA are accurate to within a few percent. But LDA has several deficiencies. It tends to give higher binding energy. In magnetic systems, LDA may give a wrong prediction of magnetic order, such as Fe is predicted to be fcc paramagnetic by LDA, but it has bcc ferromagnetic order in experiments. In strongly correlated systems LDA gives inaccurate results. For instance, LDA predicts transition metal oxides FeO, CoO, NiO and MnO to be metals or semiconductors, but they are all Mott insulators.

LDA is limited by its bad performance in systems with rapidly changing charge density. An improvement that can be easily considered is to include the gradient of the electron density, then we have the generalized gradient approximations (GGA). The general form of GGA is:

$$E_{xc}^{GGA}[n(r)] = \int f(n(r), \nabla n(r)) dr \tag{2.14}$$

Most GGAs are based on corrections on LDA, the gradient of electron density $\nabla n(r)$ can be considered as the effect of the velocity of electron's movement. The PBE [37] is a commonly used form of GGA, in which all parameters are constants, it is a simplification of the PW91 [38]. Compared with LDA, GGAs correct the overestimated binding energy, give correct predictions for magnetic systems such as Fe's bcc ferromagnetic order, and perform better for bulk phase stability, etc. Thus, GGAs have become the most common choice of exchange functional for studying magnetic materials.

2.1.4 DFT+U: On-site Coulomb repulsion correction

The self-interaction of localized electrons is not correctly described by L(S)DA or GGA, which makes the L(S)DA and GGA fail in predicting the band structures of materials with **d** and **f** orbitals such as transition metal oxides and rare earth compounds. This deficiency is remedied by introducing the on-site Coulomb repulsion term into the standard DFT total energy functional E_{DFT} in a Hatree-Fock like approach. Then, the localized orbitals can be shifted to the correct energy levels by the repulsion term. In our calculations, a simplified form of LDA+U introduced by Dudarev [39] et al is used. In Dudarev's approach, the energy functional is expressed as

$$\begin{aligned} E_{DFT+U} &= E_{DFT} + \frac{U-J}{2}\sum_{\sigma}[Tr(\rho^{\sigma}) - Tr(\rho^{\sigma}\rho^{\sigma})] \\ &= E_{DFT} + \frac{U-J}{2}\sum_{\sigma}[(\sum_{i}\rho^{\sigma}_{i,i}) - (\sum_{i,j}\rho^{\sigma}_{i,j}\rho^{\sigma}_{j,i})] \end{aligned} \tag{2.15}$$

where $\rho^{\sigma}_{i,j}$ is the density matrix element of **d** of **f** electrons with spin state σ. In Dudarev's approach, only the effective U value $U_{eff} = U - J$ is of significance.

2.2 Magnetism

2.2.1 Heisenberg Hamiltonian and exchange interactions

The spontaneous magnetic ordering originates from the interaction between atomic magnetic moments. Two types of interactions exist between atomic magnetic moments: dipole-dipole interaction and exchange interaction. Dipole-dipole interaction is the classic interaction between two magnetic dipoles. In solid states, the dipole-dipole interaction is typically very weak and has negligible effects on the magnetic ordering at room temperature.

Thus, it can be totally ignored without concern in FM, AFM, and other types of magnetic materials. The exchange interaction is a quantum effect due to the overlap of antisymmetric electron wavefunctions between neighboring atomic sites. It is described by the Heisenberg Hamiltonian,

$$H_{Heisenberg} = -\sum_{i \neq j} J_{ij} \mathbf{S}_i \cdot \mathbf{S}_j \tag{2.16}$$

where J_{ij} is the exchange coupling constant between atomic spins $\mathbf{S}_i$ on site i and $\mathbf{S}_j$ on site j. In a simple magnetic material where J_{ij} keeps the same value for all pairs of neighboring sites, the magnetic ordering is decided by the sign of J_{ij}. Positive J_{ij} makes neighboring spins tend to align parallel to each other, which results in the FM ordering. On the contrary, with a negative J_{ij} anti-parallel spins become the ground state, i.e. the AFM ordering.

2.2.2 Spin-Orbit coupling

According to the Mermin-Wagner theorem [7], finite temperature long-range magnetic ordering in 2D materials cannot exist without magnetic anisotropy. Magnetocrystalline anisotropy is a special case of magnetic anisotropy. It means the total energy of an FM material depends on the magnetization direction. In this thesis, magnetic anisotropy always refers to magnetocrystalline anisotropy. The magnetocrystalline anisotropy originates from the relativistic properties of electrons, i.e. spin-orbit coupling (SOC), which describes the interaction between the electron spins and the magnetic field generated by the orbital motion of electrons around the nucleus. Relativistic electrons are described by the Dirac equation, but it is beyond the scope of this thesis. In the non-relativistic limit $v/c \ll 1$, the

Dirac equation is reduced to the relativistic Hamiltonian,

$$H = \frac{(\mathbf{p}+e\mathbf{A})^2}{2m} - eV - \frac{e}{m}\mathbf{S}\cdot\mathbf{B} - \frac{(\mathbf{p}+e\mathbf{A})^4}{8m^3c^3} - \frac{e\hbar^2}{8m^2c^2}\boldsymbol{\nabla}^2 V$$
$$- \frac{e}{2m^2c^2}\mathbf{S}\cdot(\boldsymbol{\nabla}V\times(\mathbf{p}+e\mathbf{A})) \tag{2.17}$$

where $\mathbf{S} = \frac{\hbar}{2}\boldsymbol{\sigma}$ is the spin operator, V is the potential, $\mathbf{p}$ is the canonical momentum operator, c is the speed of light, and $\mathbf{A}$ is the magnetic vector potential. The first term $\frac{(\mathbf{p}+e\mathbf{A})^2}{2m} - eV$ is the non-relativistic Hamiltonian. The second term is the Zeeman effect,

$$H_{Zeeman} = -\frac{e}{m}\mathbf{S}\cdot\mathbf{B} \tag{2.18}$$

it describes the interaction between spins and the external magnetic field $\mathbf{B}$. The following two terms $-\frac{(\mathbf{p}+e\mathbf{A})^4}{8m^3c^3}$ and $-\frac{e\hbar^2}{8m^2c^2}\boldsymbol{\nabla}^2V$ are the relativistic kinetic energy correction and the Darwin term, respectively. The last term is the SOC term.

$$H_{SOC} = -\frac{e}{2m^2c^2}\mathbf{S}\cdot(\boldsymbol{\nabla}V\times(\mathbf{p}+e\mathbf{A})) \tag{2.19}$$

Replacing the kinetic momentum term $(\mathbf{p}+e\mathbf{A})$ by $m\mathbf{v}$, we can obtain

$$H_{SOC} = -\frac{e}{2m^2c^2}\mathbf{S}\cdot(\boldsymbol{\nabla}V\times m\mathbf{v}) \tag{2.20}$$

Assuming the potential V is spherically symmetric scalar potential, then the SOC Hamiltonian becomes

$$\begin{aligned} H_{SOC} &= -\frac{e}{2m^2c^2}\mathbf{S}\cdot(\frac{\mathbf{r}}{r}\frac{dV(r)}{dr}\times m\mathbf{v}) \\ &= -\frac{e}{2m^2c^2r}\frac{dV(r)}{dr}\mathbf{S}\cdot(m\mathbf{r}\times\mathbf{v}) \\ &= -\frac{e}{2m^2c^2r}\frac{dV(r)}{dr}\mathbf{L}\cdot\mathbf{S} \\ &= \xi(r)\mathbf{L}\cdot\mathbf{S} \end{aligned} \tag{2.21}$$

where $\xi(r)$ is the SOC constant. Switching $\mathbf{L}$ with $\mathbf{S}$ does not change the H_{SOC}, because $\mathbf{L}$ and $\mathbf{S}$ commute with each other.

For a hydrogen-like atom with the spherical potential $V(r) = eZ/4\pi\varepsilon_0 r$, the expectation value of SOC constant in the non-relativistic eigenstate $|n, l\rangle$ with principal quantum number n and orbital quantum number l can be expressed as

$$\begin{aligned} \xi_{n,l} &= \langle n, l | \, \xi(r) \, | n, l \rangle \\ &= \frac{Z^4 \alpha^4 mc^2}{2\hbar^2 n^3 l(l+\frac{1}{2})(l+1)} \end{aligned} \tag{2.22}$$

where Z is the atomic number, $\alpha = \frac{1}{4\pi\varepsilon_0}\frac{e^2}{\hbar c}$ is the fine structure constant. From this expression, we can see that the SOC constant is quite large for states with small l and large Z. Specially, when $l = 0$ the $\xi_{n,l}$ becomes 0, but the $\mathbf{L} \cdot \mathbf{S}$ term also becomes 0 which make the expectation value of H_{SOC} always be 0.

To obtain the expectation value of $\mathbf{L} \cdot \mathbf{S}$ in state $|n, l\rangle$, the following transformation is performed by using this relation $\mathbf{J} = \mathbf{L} + \mathbf{S}$,

$$\mathbf{L} \cdot \mathbf{S} = \frac{1}{2}(\mathbf{J}^2 - \mathbf{L}^2 - \mathbf{S}^2) \tag{2.23}$$

where $\mathbf{J}$ is the total angular momentum operator. Then the expectation value is

$$\langle n, l | \, \mathbf{L} \cdot \mathbf{S} \, | n, l \rangle = \frac{\hbar^2}{2}(j(j+1) - l(l+1) - s(s+1)) \tag{2.24}$$

where j, l, and s are the total angular momentum number, orbital angular momentum number, and the spin angular momentum number, respectively. Combining the Eq. (2.22) and Eq. (2.24), we can obtain the SOC energy of a given state $|n, l\rangle$

$$E_{SOC}(n, l) = \frac{Z^4 \alpha^4 mc^2 (j(j+1) - l(l+1) - s(s+1)))}{4n^3 l(l+\frac{1}{2})(l+1)} \tag{2.25}$$

By using the following ladder operators

$$S_+ = S_x + iS_y$$

$$S_- = S_x - iS_y$$

$$L_+ = L_x + iL_y$$

$$L_- = L_x - iL_y \tag{2.26}$$

The $\mathbf{L} \cdot \mathbf{S}$ term in the SOC Hamiltonian can be transformed to

$$\mathbf{L} \cdot \mathbf{S} = \frac{1}{2}(L_+S_- + L_-S_+) + L_zS_z \tag{2.27}$$

Since S_+ and S_- contain the off-diagonal terms in the spinor space and the L_+ and L_- contain off-diagonal terms in the orbital angular momentum space when $l > 0$, $\mathbf{L} \cdot \mathbf{S}$ is the only term in Eq. (2.17) coupling states with different S_z and L_z together.

2.2.3 Magnetic anisotropy

In the transition metal compounds, the SOC constant ξ is typically much smaller than the bandwidth. Thus, the H_{SOC} can be treated as the perturbation. In this approach, the SOC energy shift $\Delta E_{n,m}^{SOC}$ of a particular state $|n\rangle$ caused by a state $|m\rangle$ is

$$\Delta E_{n,m}^{SOC} = \xi \langle n| \mathbf{L} \cdot \mathbf{S} |n\rangle + \xi^2 \sum_{m \neq n} \frac{|\langle n| \mathbf{L} \cdot \mathbf{S} |m\rangle|^2}{E_n - E_m} \tag{2.28}$$

where $|n\rangle$ and $|m\rangle$ are eigenstates of the unperturbed Hamiltonian with energy levels E_n and E_m. The $\langle n| \mathbf{L} \cdot \mathbf{S} |n\rangle$ only allow states with either different spins or different orbital angular momentum couple to each other, so the first term in Eq. (2.28) has zero contribution to $\Delta E_{n,m}^{SOC}$. The numerator of the second term depends on the direction of spin quantization

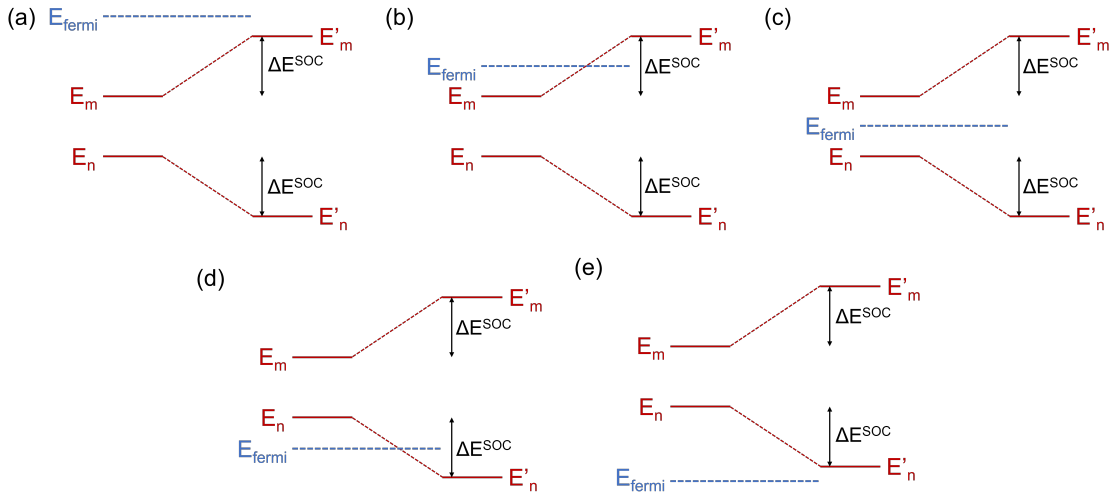

Figure 2.1: The effect of SOC on the energy levels of states $|n\rangle$ and $|m\rangle$ with Fermi level at various positions.

axis $\hat{\mathbf{n}} = (\sin\theta\cos\phi, \sin\theta\sin\phi, \cos\theta)$, which brings the anisotropy. The denominator depends on the energy difference between two states, which means the SOC coupling is stronger between states on closer energy levels. The sign of Eq. (2.28) changes when swapping $|n\rangle$ and $|m\rangle$, which indicates the two states are shifted the same amount by SOC but in opposite directions. For the SOC between degenerate states, the degenerate perturbation is needed, which gives

$$\Delta E_{n,m}^{SOC} = \pm|\xi \langle n| \mathbf{L} \cdot \mathbf{S} |m\rangle| \tag{2.29}$$

It is noteworthy that the degenerate SOC energy shift is of the first order in ξ, which makes degenerate states have stronger SOC coupling than non-degenerate states. The ΔE^{SOC} varies from 0 to its maximum value as the spin quantization axis rotates [40]. It affects the MAE in different ways depending on the position of the Fermi level. In Fig. 2.1 (a), the two states $|n\rangle$ and $|m\rangle$ are occupied before and after the SOC coupling is included. The total energy of these two states is not affected by the SOC coupling in this situation. The case in

Fig. 2.1 (b) is more complicated, $|m\rangle$ becomes unoccupied and $|n\rangle$ decreases in energy with SOC perturbation. This situation contributes to the MAE, but the changed total energy does not equal to ΔE_{SOC} because the electrons in $|m\rangle$ are redistributed after the SOC effect is included. In Fig. 2.1 (c), $|n\rangle$ is occupied and $|m\rangle$ is unoccupied with and without SOC. The total energy is changed by the amount of ΔE_{SOC} in this situation. In Fig. 2.1 (d), $|n\rangle$ changes from unoccupied to occupied, which increases the total energy. Similarly to the case in Fig. 2.1 (b), electrons re-distribution happens when SOC is included. In Fig. 2.1 (e), the two states $|n\rangle$ and $|m\rangle$ are always unoccupied before and after the SOC is included, so they have no contribution to the total energy.

2.3 First principles phonon dispersion calculation

The harmonic approximation is commonly used in phonon frequency calculation. Atoms are assumed oscillating around their equilibrium positions **r** with displacements **d**. The total energy function Φ is assumed to be a function of the displacements around equilibrium positions up to the second order. The total energy is expressed in the following series form:

$$\Phi = \Phi_0 + \sum_{a=x,y,z} \sum_{l,n} \Phi_a(l,n) d_a(l,n) + \frac{1}{2!} \sum_{a,b} \sum_{l,n,l',n'} \Phi_{a,b}(l,n,l',n') d_a(l,n) d_b(l',n') \quad (2.30)$$

where a, b = x, y, z represent directions of three Cartesian coordinate axes. l and n are the labels of unit cell and atom in that unit cell respectively. Φ_0 is the zeroth order force constant which does not depend on the positions of atoms, it is set to be 0 by default. $\Phi_a(l,n)$ is the first order force constant acting on the nth atom in the lth unit cell along direction a. $\Phi_a(l,n)$ only depends on the position of one atom and one direction. $\Phi_{a,b}(l,n,l',n')$ is the

more complicated second order force constant which is determined by two atoms and two directions. $d_a(l,n)$ is the displacement of the nth atom in the lth unit cell along direction a.

The finite displacement method is used to calculate these force constants. Potential energies of unit cells with small displacements along different directions at constant volume are calculated by first principles method such as DFT. A force $F_a(l,n)$and a second-order constant $\Phi_{a,b}(ln,l'n')$ are obtained by partial derivatives of potential energy.

$$F_a(l,n) = -\frac{-\partial\Phi}{\partial d_a(l,n)} \tag{2.31}$$

$$\Phi_{a,b}(l,n,l',n') = \frac{\partial^2\Phi}{\partial d_a(l,n) d_b(l',n')} = -\frac{\partial F_b(l',n')}{\partial d_a(l,n)} \tag{2.32}$$

With the finite displacement method, the force is given approximately by the total energy difference between the unchanged and displaced unit cell as

$$F_a(l,n) = \frac{V - V^{d_a(l,n)}}{d_a(l,n)} \tag{2.33}$$

and the second-order derivative is also replaced by

$$\Phi_{a,b}(l,n,l',n') = \frac{F_b(l',n') - F_b^{d_a(l,n)}(l',n')}{d_a(l,n)} \tag{2.34}$$

where the superscript $d_a(l,n)$ means the nth atom is displaced d along the a direction. The forces on atoms at equilibrium positions are all zero. With these second-order force constants, the dynamical matrix D(q) is constructed as

$$D_{a,b,n,n'}(\mathbf{k}) = \sum_{l'} \frac{\Phi_{a,b}(0,n,l',n')}{\sqrt[2]{m_n m_{n'}}} e^{i\mathbf{k}\cdot[\mathbf{r}(l',n') - \mathbf{r}(0,n)]} \tag{2.35}$$

The dynamical matrix describes the interaction between the nth atom with a mass of m_n in one unit cell and the n'th atom with a mass of $m_{n'}$ in all unit cells. The sum of the unit

cells usually runs over the nearest neighbors in practical calculations in order to reduce the cost.

The phonon frequency $\omega_{\mathbf{k}}$ and polarization vector $\mathbf{p}_{\mathbf{k}}$ are obtained by solving eigenvalue equation of dynamical matrix D($\mathbf{k}$),

$$\sum_{b,n'} D_{a,b,n,n'}(\mathbf{k})\mathbf{p}_{\mathbf{k}j,b,n'} = \omega^2_{\mathbf{k}j}\mathbf{p}_{\mathbf{k}j,a,n} \tag{2.36}$$

where j is the index of the jth phonon band. The displacement vector of the nth atom in the lth unit cell can be derived from its corresponding polarization vector,

$$\mathbf{d}(l,n) = \frac{A}{\sqrt{m_n}}\mathbf{p}_{kj,n}e^{i\mathbf{q}\cdot\mathbf{r}(l,n)} \tag{2.37}$$

where A is the complex constant.

The displacement vectors $\mathbf{d}(l,n)$ are used for analyzing and visualizing the vibration modes. The phonon dispersion is plotted from phonon frequencies at $\mathbf{k}$ points connecting high-symmetry points in reciprocal space. The potential energy Φ is at its minimum if the crystal is in the ground state, which means any displacement of an atom from the equilibrium position increase the energy. The phonon frequencies of a stable phase are real at all $\mathbf{k}$ points. The imaginary frequencies (always shown as negative frequencies in the dispersion curve) indicate the current unit cell is not in the ground state and has the possibility of phase transition.

Chapter 3

Structural, Electronic, and Magnetic Properties of $CrTe_2$

3.1 Introduction

The recent discovery of monolayer two-dimensional (2D) ferromagnetic (FM) material [41, 42], the compatibility of 2D FM materials with other 2D materials, and their susceptibility to external control of their magnetic properties have made 2D FM materials a topic of high current interest. For example, the magnetic anisotropy can be controlled by applying an external electric field [43], strain [44], and band filling [45]. The ground state magnetic ordering can be switched among ferromagnetic (FM), anti-ferromagnetic (AFM), collinear, and noncollinear by stacking pattern [46], strain [47], and electric field [48, 49]. Moreover, the formation of heterostructures with other 2D materials, breaks time reversal symmetry, which can be exploited for valleytronics [50] or the Chern insulator [51].

A relatively new class of layered magnetic materials such as $CrTe_2$, CrI_3 and $CrGeTe_3$ have extended the applicability of the layered materials in the field of spintronics [52]. One material of particular interest is $CrTe_2$ in which Cr hexagonal planes are sandwiched by Te layers. Several studies [53, 54] suggested the non-magnetic 2H phase was the ground state, whereas recent studies all find the 1T phase to be the ground state [12, 13, 55, 56, 57, 58]. 1T-$CrTe_2$ has one of the highest Curie temperatures among the 2D magnetic materials. The discovery that bulk 1T-$CrTe_2$ is a layered metallic ferromagnet with a Curie temperature of $\sim$ 310 K [12], led to a number of further studies. Mechanical exfoliation of 1T-$CrTe_2$ with either h-BN or Pt encapsulation in a glove box produced samples in which easy-plane ferromagnetism was maintained in thin-films down to $\sim$ 8 nm while maintaining a Curie temperature above 300 K [13]. This study also showed that $CrTe_2$ rapidly oxidizes in ambient conditions and that the pristine Raman peaks at 100 cm^{-1} and 134 cm^{-1} shift to 125 cm^{-1} and 145 cm^{-1} after a few hours in air [13]. A number of studies of epitaxial grown material quickly followed. Thin film 1T-$CrTe_2$ was grown by molecular beam epitaxy (MBE) on bilayer graphene (BLG)/SiC and capped with a 5 nm Te layer to prevent the oxidation [55]. Ultrathin films ($\leq$ 7 monolayers (ML)) posessed perpendicular magnetic anisotropy (PMA) with T_c dropping from 300 K for thicker films down to 200 K for a monolayer. A large PMA constant of $K_u = 5.63 \times 10^6$ erg/cm^3 was measured for a 7 ML film. In a separate work, this value of K_u was also found for 80 nm thick films of $Cr_{1.3}Te_2$ [15]. In thin films of 1T-$CrTe_2$ grown by chemical vapor deposition (CVD) on SiO_2, the magnetic easy axis changed from in-plane to perpendicular as the thickness was reduced below approximately 10 nm ($\approx$ 17 MLs) [56]. Reflectance magneto

circular dichroism measurements showed that T_c increased from approximately 165 K to 212 K as the film thickness decreased from 48 nm to 7.5 nm. This last trend of *increasing* T_c with *decreasing* film thickness is unique to these samples and experiments. The majority of the data in this study was taken from oxidized samples based on the Raman peaks at 123 cm^{-1} and 143 cm^{-1}, however a comparison was made between samples with and without h-BN encapsulation; the values for T_c remained essentially the same, and both sets of films exhibited strong PMA [56]. The authors theoretically found that the sign of the magnetic anisotropy energy (MAE) in ML 1T-$CrTe_2$ switches from in-plane to out-of-plane with increasing magnitude of the on-site Coulomb potential (U), with switching occurring at $U \sim 3.2$ eV; and they discuss the possibility that thinner samples provide less screening, larger electrostatic interaction with the substrate, larger values of U, and thus PMA [56]. MBE grown 1T-$CrTe_2$ on (111) GaAs exhibited a Curie temperature that dropped from $T_c = 205$ K for a 35 ML film to 191 K for a 4 ML film, and, unique to these samples, all thicknesses exhibited PMA [57]. No information on a capping layer or other protection from oxidation was provided [57]. A most recent study of MBE grown 1T-$CrTe_2$ on BLG/SiC found that ML 1T-$CrTe_2$ had a zigzag AFM (z-AFM) ground state accompanied by a 2×1 reconstruction of the lattice resulting from relatively large substrate induced strain (-5% along a_1 and +3% along a_2) [59].

The intense interest in 1T-$CrTe_2$ also motivated many theoretical investigations based on density functional theory calculations. Calculations using the Perdew-Burke-Emzerhof (PBE) functional [37] without a Hubbard U correction or spin orbit coupling found that 1% compressive strain caused ML 1T-$CrTe_2$ to transition from an FM to an

AFM ground state [60]. Simulations of ML 1T-$CrTe_2$ with the all electron code WIEN2k [61] using the PBE functional found unstable modes in the phonon spectrum which were removed in a $\sqrt{3}\times\sqrt{3}$ charge density wave (CDW) state [62]. In both the normal and CDW phase, tensile strain was required to obtain PMA, and the magnetic anisotropy switched from in-plane to out-of-plane for a lattice constant of $\gtrsim$ 3.8 Å in the CDW phase and $\gtrsim$ 3.86 Å in the normal phase [62]. PBE+U calculations, with $U = 2$ eV, found a stable phonon spectrum for ML 1T-$CrTe_2$ and in-plane FM magnetization [63]. The finding of in-plane magnetization results from the use of the value $U = 2$ eV [56]. PBE level calculations without a Hubbard U correction found an AFM ground state for ML 1T-$CrTe_2$, and a reduction of the lattice constant from 3.79 Å in the bulk to 3.68 Å in ML [64]. The ML AFM ground state was attributed to the reduction of the lattice constant. The thickness dependence of the magnetization of 1T-$CrTe_2$ was investigated [65] using the opt-B86b-vdW functional [66] implemented in VASP [67, 68]. The ML ground state was found to be z-AFM with a corresponding reduction of the in-plane lattice constant from $\sim$ 3.8 Å for bulk to $\sim$ 3.57 Å for ML [65]. The FM ML CDW ground state [62] was found to be higher in energy than the z-AFM state. The results are qualitatively similar to those of Ref. [64]. AFM interlayer coupling was found in 2 through 4 MLs, and FM interlayer coupling for 5 MLs or more [65]. PBE-D3 + (U=2 eV) calculations of bilayer 1T-$CrTe_2$ found a g-type AFM ground state with both intra-layer and inter-layer AFM coupling [69]. Compressive strain greater than 4% caused the interlayer coupling to become FM while the intra-layer coupling remained AFM.

CrI_3 is another 2D magnetic material with many similarities to $CrTe_2$. The Cr

ion is in octahedral coordination with the I anions resulting in the same e_g, t_{2g} crystal field splitting and superexchange coupling through the Cr-I-Cr bonds at near 90° bond angles. The origin of the large out-of-plane magnetic anisotropy in CrI_3 has been investigated in detail [70, 71]. It was found that the MAE is primarily from the SOC on the I atoms, and, therefore, anisotropic superexchange is the source of the magnetic anisotropy [70]. Further investigation found that the MAE was very sensitive to the deviation of the dihedral angle θ_D between the plane formed by the Cr-I-Cr bonds and a vertical plane through the Cr-Cr pair [71], which is a measure of the trigonal distortion of the edge-sharing $CrTe_6$ octahedra. In the undistorted octahedron, the dihedral angle $\theta_{O_h} \approx 35.3°$, and the deviation is defined as $\delta\theta \equiv \theta_{O_h} - \theta_D$. In CrI_3, positive values for $\delta\theta_D$ resulted in out-of-plane magnetic anisotropy and negative values resulted in in-plane magnetic anisotropy.

The variety of different and contradicting experimental data for 1T-$CrTe_2$ originating from different growth conditions and substrates indicates a sensitivity of the thin layer material to external perturbations such as strain, band filling and screening. The variety of different and contradictory theoretical predictions resulting from different models and, particularly, from the use of different values of U possibly indicate a sensitivity to screening, which is affected by different environments as discussed in [56]. In few monolayer films, both the interlayer magnetic coupling and the sign of the magnetic anisotropy are affected in incompatible ways by the value of U. For few layer films, small U values give, what appears to be at this time, the experimentally correct sign of the interlayer magnetic coupling coupling (i.e. FM), but the incorrect sign for the magnetic anisotropy (i.e. prediction of easy-plane magnetic anisotropy). Conversely, larger values of U predict the correct

magnetic anisotropy (PMA), but the incorrect interlayer magnetic coupling (i.e. AFM). Thus, to address the question of the magnetic anisotropy in a monolayer, a value for U must be chosen that reproduces the observed magnetic anisotropy, which, experimentally, is found to be out-of-plane.

In this work, we first quantify the energy differences and energy barriers separating the different crystallographic phases: 1T, 1H, and 2H. We then focus on the magnetic anisotropy of bilayer and monolayer 1T-$CrTe_2$ and understand how it is affected by strain and band filling. We investigate the source of the magnetic anisotropy originating from the large SOC of the Te atoms. Based on the insights gained from prior work on CrI_3 [70, 71], we analyze the SOC matrix elements and distortion of dihedral angle, and their relationships to the sign of the MAE. Finite temperature long range magnetic order in 2D monolayer 1T-$CrTe_2$ is subject to the Mermin-Wagner theorem [7]. As such, an energy gap is required in the magnon excitation spectrum to prevent the magnetic order from being destroyed by thermal fluctuations. This energy gap results from the magnetic anisotropy. The interdependence of the MAE, exchange coupling, and Curie temperature in ML 1T-$CrTe_2$, is analyzed using renormalized spin wave theory (RSWT) [72]. RSWT provides a mean field self-consistent calculation of the magnon mode occupation and the average magnetic moment as a function of temperature. Examples of RSWT applied to other 2D magnetic materials can be found in Refs [42, 70, 49]. Finally, an inverse calculation is performed in which the experimentally measured value for T_c is used to determine all pairs of values for the MAE and exchange coupling constants that result in T_c.

3.2 Computational methods

The first-principle calculations use spin-polarized density functional theory (DFT) with the projector augmented wave (PAW) [73, 74] method and a plane-wave basis, as implemented in the Vienna ab initio simulation package (VASP) [67, 68]. The Perdew-Burke-Enzerhof's (PBE) [37] version of the generalized gradient approximation (GGA) is used for the exchange-correlation density functional. The vdW corrections are included with the PBE+D3 model [75]. All structural relaxation calculations use the PBE+D3 level of theory. The lattice is fully relaxed until the force on each atom is smaller than 0.001 eV/Å. For finite thickness slabs, 15 Å vacuum layers are added. Energy barriers between the ground state and the metastable states of $CrTe_2$ are determined using the nudged elastic band (NEB) method [76, 77].

For calculation of the electronic and magnetic properties, the Hubbard U correction (PBE+U) [39]. and spin orbit coupling (SOC) are included. The values of the U parameter for the different phases of $CrTe_2$ are calculated using the linear response method [78], and the values are given in Table 3.1. In this method, the linear behavior of the total energy with respect to the occupation number is imposed to correct the local and semi-local functionals. Prior to the implementation of the Linear Response method, the standard DFT calculation was first performed to obtain the converged charge. Following that, the interacting response of one single Cr atom was calculate by performing self-consistent DFT calculations with a series of Lagrange multipliers for the energy window from -0.08 to 0.08 eV, which usually falls within the linear region of number of d electrons versus Lagrange multipliers. The bare response of a single Cr atom was calculated by performing a non-self-consistent charge

Table 3.1: U parameters of the Cr atom in $CrTe_2$ calculated from linear response method.

Phases	1T bulk	1H bulk	2H bulk	1T 1L	1H 1L	2H 2L
U (eV)	5.80	5.59	5.85	5.92	5.91	5.59

calculation with the same Lagrange multipliers as the self-consistent calculations. To avoid the interaction between the Cr atom and its periodic image within the unit cell, a 2×2×2 supercell was used during the U parameters calculations. The U parameter is then given by the difference between the second derivatives of the self-consistent energy, α^{scf} and the non-charge-self-consistent energy, $\alpha^{non-scf}$, with respect to the localized occupation of a single site [78],

$$U = \frac{\partial \alpha_i^{scf}}{\partial q_i^{scf}} - \frac{\partial \alpha_i^{non-scf}}{\partial q_i^{non-scf}} \tag{3.1}$$

where α is the Lagrange multiplier, q_i is the number of d electrons of the single Cr atom. The first term in the right-hand side of the equation represents the interacting case, whereas the second term represents non-interacting case. The accuracy of DFT+U calculations depends on the choice of the system dependent parameter, U. In general, the value of U parameter is determined empirically to match experimental structural and electronic properties of a given material.

For all calculations of the magnetic properties of 1T-$CrTe_2$, the value of U= 5.8 eV is used. Because with U = 5.8 eV, the magnetic moment per formula unit of 1T-$CrTe_2$ is 3.05 μ_B for monolayer and 3.08 μ_B for bulk, which are closest to the typical value 3 μ_B. Calculated magnetic moments as a function of U is provided in Table. 3.2. This method has been used for other 2D Cr based materials such as CrX_3(X = Cl, Br, I) monolayers

Table 3.2: DFT calculated magnetic moment (μ_B) per Cr atom in 1T-$CrTe_2$ with different U values.

U (eV)	0	1	2	3	4	4.5
Mono-layer	2.390	2.548	2.667	2.769	2.860	2.913
Bi-layer	2.406	2.562	2.692	2.806	2.903	2.949
Bulk	2.385	2.528	2.661	2.781	2.884	2.933
U (eV)	4.8	5	5.8	6	7	8
Mono-layer	2.953	2.978	3.085	3.110	3.208	3.285
Bi-layer	2.976	2.993	3.059	3.074	3.148	3.216
Bulk	2.958	2.981	3.053	3.070	3.147	3.219

[79]. 12 valence electrons are included for Cr ($3p^6 3d^5 4s^1$), and 6 valence electrons for Te ($5s^2 5p^4$). The cutoff energy is 500 eV. A 24×24×12 Monkhorst-Pack k-grid mesh [80] for bulk structures and a 28×28×1 mesh for layered structures are used to ensure that the magnetic anisotropy energies are well converged. The convergence tests are shown in Fig. 3.1. The Gaussian smearing method is employed with a width of 0.05 eV for the structure, magnetic, and energy barrier calculations for insulating systems. For metallic systems, the Methfessel-Paxton smearing method is employed with a width of 0.05 eV.

3.3 Results

3.3.1 Ground state and energy barrier in phase transition

$CrTe_2$ can potentially crystalize into various layered phases such as 1T, 1T_d, 1H, and 2H phases [81, 82], as illustrated in Fig. 3.2. The geometry-optimized in-plane lattice

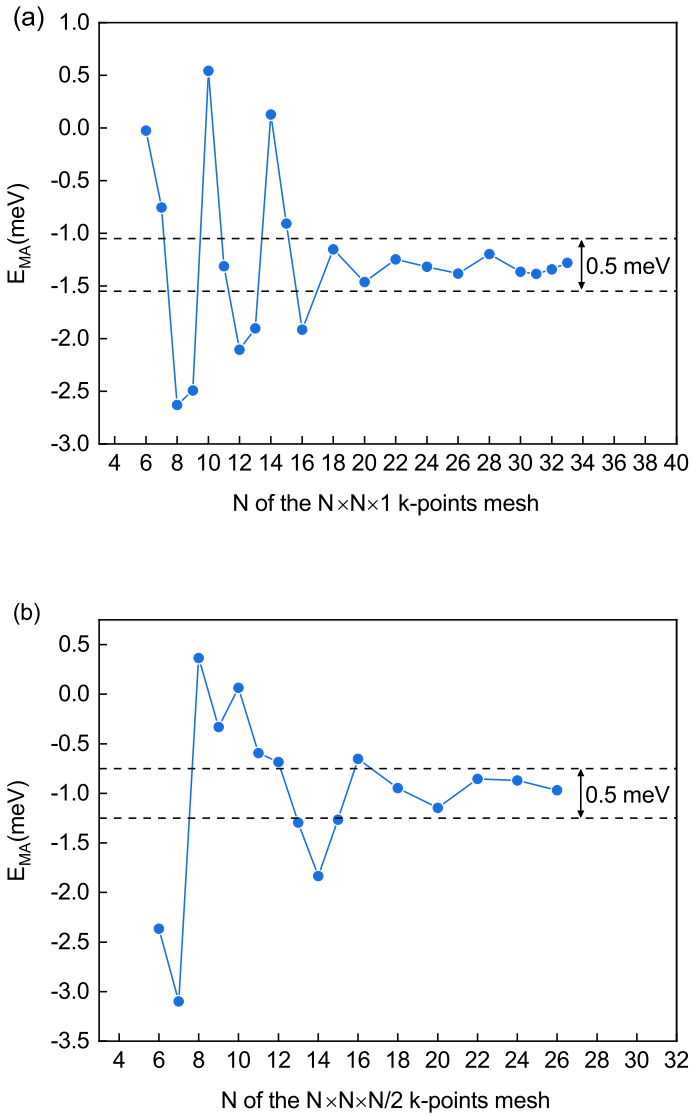

Figure 3.1: K-point convergence test on the magnetic anisotropy energy in (a) layered and (b) bulk 1T-$CrTe_2$

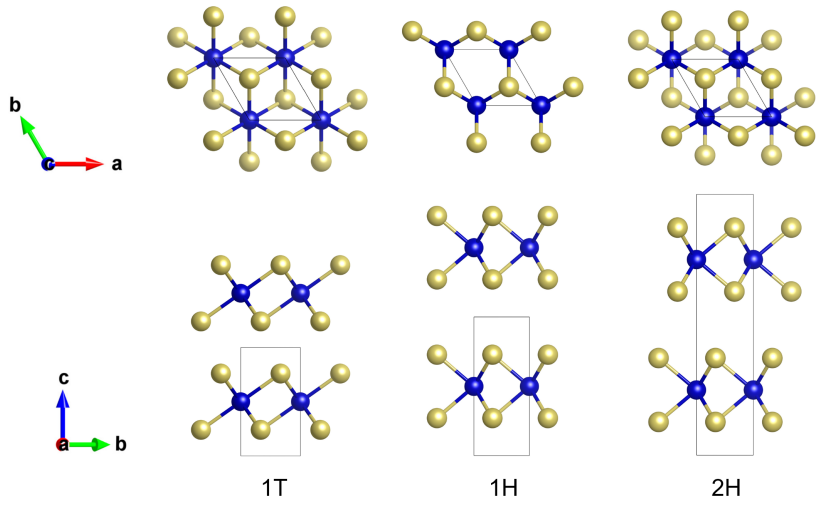

Figure 3.2: Top and lateral views of 1T, 1H, and 2H phases of $CrTe_2$. The unit cells are shown by the thin lines. Blue and golden balls represent Cr and Te atoms, respectively. The 1T phase contains one formula unit (f.u.) per unit cell in a hexagonal lattice belonging to the $P\bar{3}m1$ space group with each Cr atom surrounded by Te atoms in octahedral coordination. The 1H and 2H phases are hexagonal, trigonal prismatic, and the difference between the two phases is in their interlayer stacking. In the 1H structure, layers are stacked directly on top of each other so that the 1H structure contains 1 f.u. / unit cell and belongs to the $P\bar{6}m2$ space group. The 2H structure contains 2 f.u. / unit cell and belongs to the $P6_3/mmc$ space group.

constant a and the interlayer distance d for each phase is shown in Table. 3.3. Among all of the possible phases, the $1T_d$ phase of $CrTe_2$ in both the bulk and monolayer forms is unstable during the structure optimization step, and hence is excluded from this study. Experimental values are only known for the 1T bulk phase, and our calculated values match well with the experimental ones of $a = 3.7887$ Å and $c = 6.0955$ Å [12].

To determine the energetic stability of each phase, the formation energy E_{form} is calculated from the energy difference between the material and isolated atoms per chemical formula, which is defined as

$$E_{form} = E_{total} - \sum_{i}^{n} E_i \tag{3.2}$$

Table 3.3: Formation energies E_{form} (eV) and relaxed lattice constants for different phases of $CrTe_2$ in bulk, monolayer (1L) and bilayer (2L) geometries. For the bilayer structure, c corresponds to the interlayer Cr-Cr distance.

Phases	E_{form}	a	c
1T bulk	-10.44	3.787	5.967
1T 2L	-10.18	3.759	-
1T 1L	-10.09	3.692	-
1H bulk	-10.04	3.491	7.493
1H 1L	-9.75	3.646	-
2H bulk	-10.14	3.498	6.951
2H 2L	-9.98	3.493	7.001

where E_{total} is the total energy of the material, E_i is the energy of a single constituent atom, and n is the total number of atoms in the unit cell of the material. A more negative E_{form} corresponds to a more stable system. As shown in the Table. 3.3, the 1T phase is the ground state for both the bulk and the monolayer forms. Quantitatively, the formation energy of the 1T bulk phase is lower than those of the 2H and 1H phases by 0.30 and 0.40 eV, respectively. The energetic barriers separating the ground state from the metastable states, calculated from the NEB method, are shown in Fig. 3.3 for (a) bulk and (b) monolayer. The energies of the 1T bulk and monolayer serve as the reference energies and are set to be 0 eV. The energetic barriers for the bulk phase transitions from 1T to 2H and 1H are 0.99 eV and 0.95 eV, respectively. The energetic barrier for the monolayer transition from 1T to 1H is 0.78 eV. The large magnitudes of energy barriers separating the 1T phase from

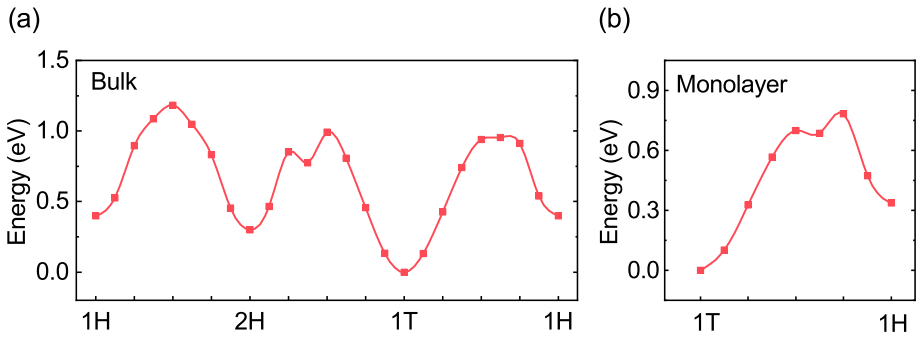

Figure 3.3: (a)The energy barrier between 1H, 2H, and 1T phases of bulk $CrTe_2$. (b)The energy barrier between 1T and 1H phases of monolayer $CrTe_2$.

the other metastable phases combined with the large energy differences of the ground states, indicate that the 1T phase, in both bulk and monolayer forms, should be very stable, and transitions to other phases difficult to achieve.

To verify the stability of 1T phase monolayer, the phonon spectrum is calculated using different U parameters as shown in Fig. 3.4. As found previously [63], the unstable modes vanish with the inclusion of a non-zero Hubbard U parameter. It is also found from our calculation that the phonon becomes insensitive to the Hubbard U parameter when $U > 1$ eV.

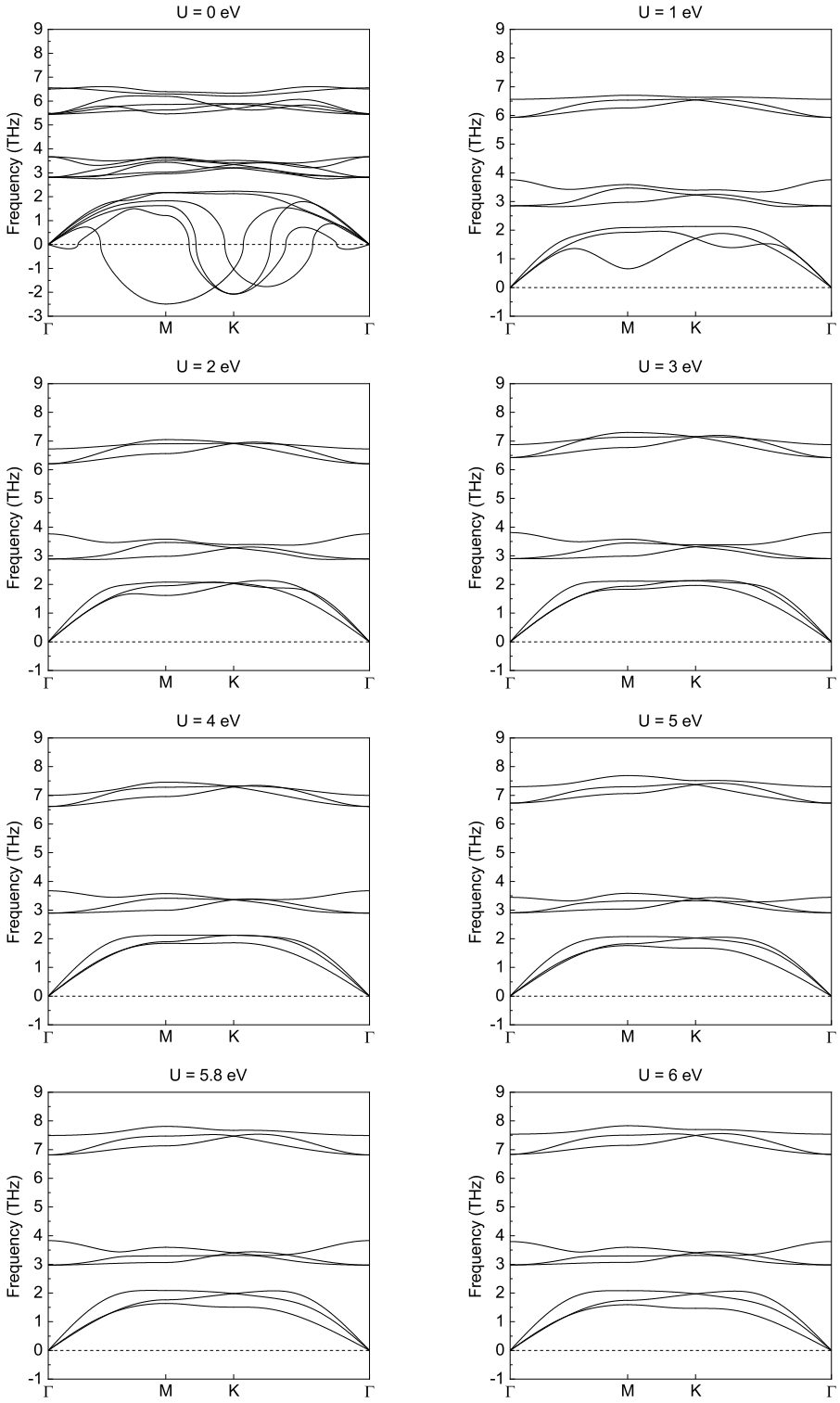

Figure 3.4: Phonon spectra of monolayer 1T-$CrTe_2$ calculated with different values of U.

3.3.2 The magnetic anisotropy of layered and bulk 1T-$CrTe_2$

The magnetic anisotropy energy plays a crucial role in the stability of the magnetic ordering in low dimensional materials, and there is great interest in controlling it with externally applied fields and strain. We therefore investigate the sensitivity of the MAE to strain and band filling in both few-layer and bulk 1T-$CrTe_2$. Since, the energy differences and energy barriers between the 1T phase and the other phases are large, we only consider the magnetic properties of the 1T phase.

The MAE (Δ_{MA}) is defined as the energy difference between the total energies E_{total} when the magnetization $\mathbf{m}$ lies along the x axis or the z axis, i.e.

$$\Delta_{\mathrm{MA}} = E_{\mathrm{total}}(\mathbf{m}\|\hat{x}) - E_{\mathrm{total}}(\mathbf{m}\|\hat{z}). \tag{3.3}$$

The sign of MAE is very sensitive to the Hubbard U parameter, as shown in Fig. 3.5. U = 5.8 eV is used to calculated the MAE of all different structures of $CrTe_2$. As shown in the Table. 3.4, in the FM ground state, the magnetization easy axis of monolayer 1T-$CrTe_2$ is out-of-plane while the multilayer and bulk 1T-$CrTe_2$ have in-plane magnetic easy axes.

Device applications require external control of the MAE, so we therefore consider the effects of strain and band filling in monolayer, bilayer, and bulk 1T-$CrTe_2$. As shown in the Fig. 3.6(a) the MAE of a monolayer is sensitive to tensile bi-axial strain, and the MAE of a bilayer is sensitive to compressive bi-axial strain. The easy axis of monolayer 1T-$CrTe_2$ switches from out-of-plane (z-axis) to in-plane (x-axis) at 2.3% bi-axial tensile strain. The easy axis of bilayer 1T-$CrTe_2$ switches from in-plane (x-axis) to out-of-plane (z-axis) at 3% bi-axial compressive strain. The MAE of the bulk structure is relatively insensitive to the

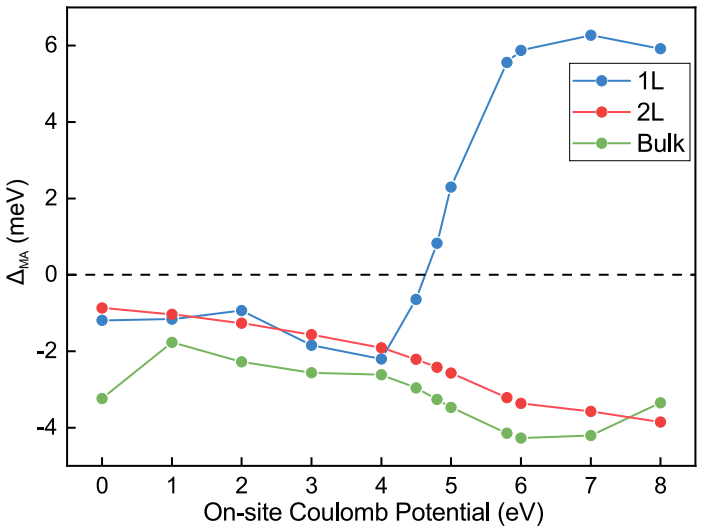

Figure 3.5: DFT calculated magnetic anisotropy energy (Δ_{MA}) as a function of on-site Coulomb potential U for monolayer, bilayer, and bulk 1T-$CrTe_2$.

Table 3.4: Magnetic anisotropy energies of 1T-$CrTe_2$ in layered and bulk forms.

Structure	MAE per f.u. (meV)	Easy axis
1L	5.56	out-of-plane
2L	-4.15	in-plane
3L	-3.61	in-plane
4L	-2.88	in-plane
5L	-3.37	in-plane
6L	-3.29	in-plane
Bulk	-3.22	in-plane

applied uniaxial or biaxial strain. As shown in Fig. 3.6(b), band filling also switches the magnetic moment of monolayer of 1T-$CrTe_2$ from out-of-plane (z-axis) to in-plane (x-axis). The sign of the MAE switches at a filling of 0.22 electrons per unit cell, corresponding to a sheet carrier concentration of $n_s = 1.9 \times 10^{14}$ cm^{-2}.

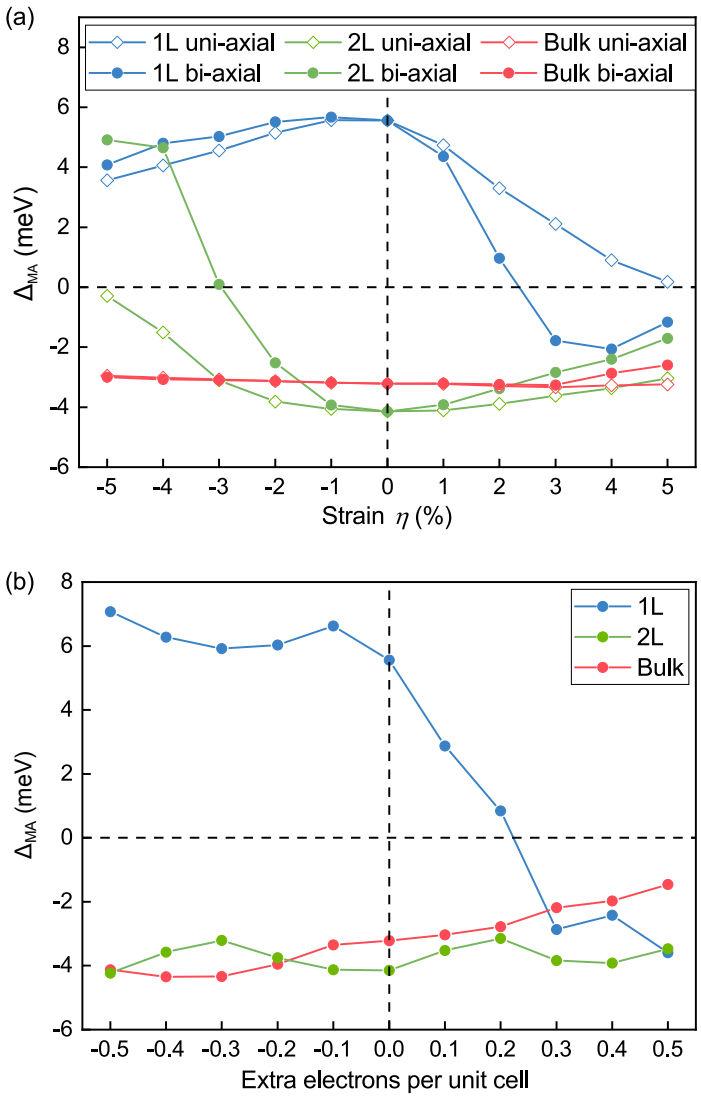

Figure 3.6: The MAE as a function of (a) strain and (b) band filling of 1L, 2L, and bulk 1T-$CrTe_2$

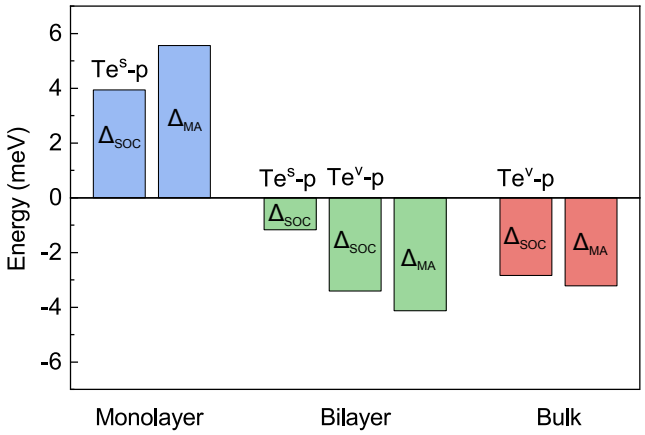

Figure 3.7: Magnetic anisotropy energy Δ_{MA} (per f.u.) and difference in SOC energies Δ_{SOC} (per f.u.) of Te-5p orbitals between the x (in-plane) and z (out-of-plane) magnetization orientations. Te^s and Te^v denote the Te atoms on the surface and at the vdW gap of the bilayer, respectively.

To obtain insight into the source of the magnetic anisotropy in 1T-$CrTe_2$, we consider the SOC matrix elements of Cr-3d and Te-5p orbitals. The Cr d-orbitals' contributions to SOC matrix elements are negligible in comparison with those of the Te p-orbitals, so they will be ignored. We abbreviate the p-orbital matrix elements of the SOC term in the Hamiltonian as $\langle p_i|p_j\rangle$. Similar to the definition of the MAE in Eq. (3.3), we define

$$\Delta_{\mathrm{SOC}} = E_{\mathrm{SOC}}(\mathbf{m}\|\hat{x}) - E_{\mathrm{SOC}}(\mathbf{m}\|\hat{z}) \tag{3.4}$$

where E_{SOC} is the energy associated with the SOC matrix elements.

In Fig. 3.7, $E_{\mathrm{SOC}}(\mathbf{m}\|\hat{x},\hat{z})$ is calculated from the sum of the SOC matrix elements, i.e.

$$E_{\mathrm{SOC}}(\mathbf{m}\|\hat{x},\hat{z}) = (\langle p_y|p_x\rangle + \langle p_y|p_z\rangle + \langle p_x|p_z\rangle)|_{\mathbf{m}\|\hat{x},\hat{z}} \tag{3.5}$$

and the difference Δ_{SOC} is plotted. Fig. 3.7 shows Δ_{MA} and Δ_{SOC} for monolayer, bilayer and bulk 1T-$CrTe_2$. It is clear that the difference in the SOC energy Δ_{SOC} tracks both

the magnitude and sign of the MAE, Δ_{MA}. In the bilayer structure, the Te atoms on the outer surfaces (Te^s) and the ones adjacent to the vdW gap (Te^v) are in different chemical environments, and thus they contribute different amounts to the total MAE.

The changes in individual SOC matrix elements with different magnetization directions are shown in Fig. 3.8. Here, $\Delta_{\langle p_i|p_j\rangle} = \langle p_i|p_j\rangle|_{\mathbf{m}\|\hat{x}} - \langle p_i|p_j\rangle|_{\mathbf{m}\|\hat{z}}$. In the FM ground state (zero strain) of monolayer 1T-$CrTe_2$, $\langle p_y|p_z\rangle$ contributes the most to Δ_{SOC}, while in the FM ground states of bilayer and bulk, the dominant matrix element is $\langle p_y|p_x\rangle$. A dominant $\Delta_{\langle p_y|p_z\rangle}$ matrix element anisotropy coincides with an out-of-plane easy axis, and a dominant $\Delta_{\langle p_y|p_x\rangle}$ matrix element anisotropy coincides with an in-plane magnetic easy axis.

Fig. 3.8(a) also shows the effect of strain on the dihedral angle θ_D between the Cr-Te-Cr plane and a vertical plane through the Cr-Cr pair illustrated in Fig. 3.9. Positive values of $\delta\theta_D = \theta_{O_h} - \theta_D$ correspond to the Cr-Te-Cr plane becoming more vertical. For the monolayer and bilayer, an out-of-plane easy axis occurs at more positive values of $\delta\theta_D$, which is qualitatively consistent with the results for CrI_3 described in Ref. [71], although the dependence is far from linear. For the monolayer in equilibrium, $\delta\theta_D = 2.6°$ is relatively large and positive, the $\Delta_{\langle p_y|p_z\rangle}$ matrix element anisotropy is dominant, and the easy axis is out of plane. For the bilayer in equilibrium, two values of $\delta\theta_D$ are given, one for the Te atom at the surface (1.0°) and one for the Te atom at the van der Waals gap (0.8°). The angles are similar, $\delta\theta_D \sim 1°$, the matrix element anisotropy is dominated by $\Delta_{\langle p_y|p_x\rangle}$, and the easy axis is in plane. As compressive bi-axial strain is applied to the bilayer, $\delta\theta_D$ becomes more positive, the SOC matrix element anisotropy $\Delta_{\langle p_y|p_z\rangle}$ becomes dominant,

and the easy plane rotates from in-plane to out-of-plane. For the bulk, compressive strain increases $\delta\theta_D$ to 3.3°, however in the bulk, the anisotropy of the SOC matrix elements and the magnetic anisotropy are insensitive to strain and the dihedral angle.

In terms of percent change, strain has the largest effect on the dihedral angle θ_D, the second largest effect on the Cr-Te-Cr bond angles, and minimal effect on the bond lengths. The distortion produced by in-plane strain or a reduction of the equilibrium in-plane lattice constant is primarily absorbed by the dihedral angles and bond angles. The decrease in the dihedral angle θ_D is accompanied by a reduction of the Cr-Te-Cr bond angle. For example, the equilibrium in-plane lattice constant of a monolayer (3.692 Å) is 2.5% smaller than that of the bulk (3.787 Å), the Cr-Te-Cr bond angle of the ML (86.3°) is 4% smaller than that of the bulk (89.9°), and the dihedral angle (32.7°) is 7% smaller than that of the bulk (35.2°). Even though the lattice constants of the ML are 2.5% smaller than those of the bulk, the Cr-Te bond lengths of the ML (2.70 Å) are 0.7% longer than those of the bulk (2.68 Å), since the Te atoms in the ML are free to move into the vacuum. The bond angles and bond lengths of the equilibrium bilayer lie in between those of the monolayer and bulk. The bilayer Cr-Te$^{v(s)}$ bond lengths are 2.68(2.69) Å, the Cr-Te$^{v(s)}$-Cr bond angles are 88.9°(88.5°), and the Cr-Te$^{v(s)}$-Cr dihedral angles are 34.5°(34.3°). When the bilayer is compressed 4% in-plane, the Cr-Te$^{v(s)}$ bond lengths are reduced by 0.6%(0.09%), the Cr-Te$^{v(s)}$-Cr bond angles are reduced by 4.3%(4.8%), and the Cr-Te$^{v(s)}$-Cr dihedral angles are reduced by 9%(10%).

As shown in Fig. 3.8(b), band filling in the monolayer switches the $\langle p_y|p_x\rangle$ anisotropy from positive to negative, and it decreases the magnitudes of the other two

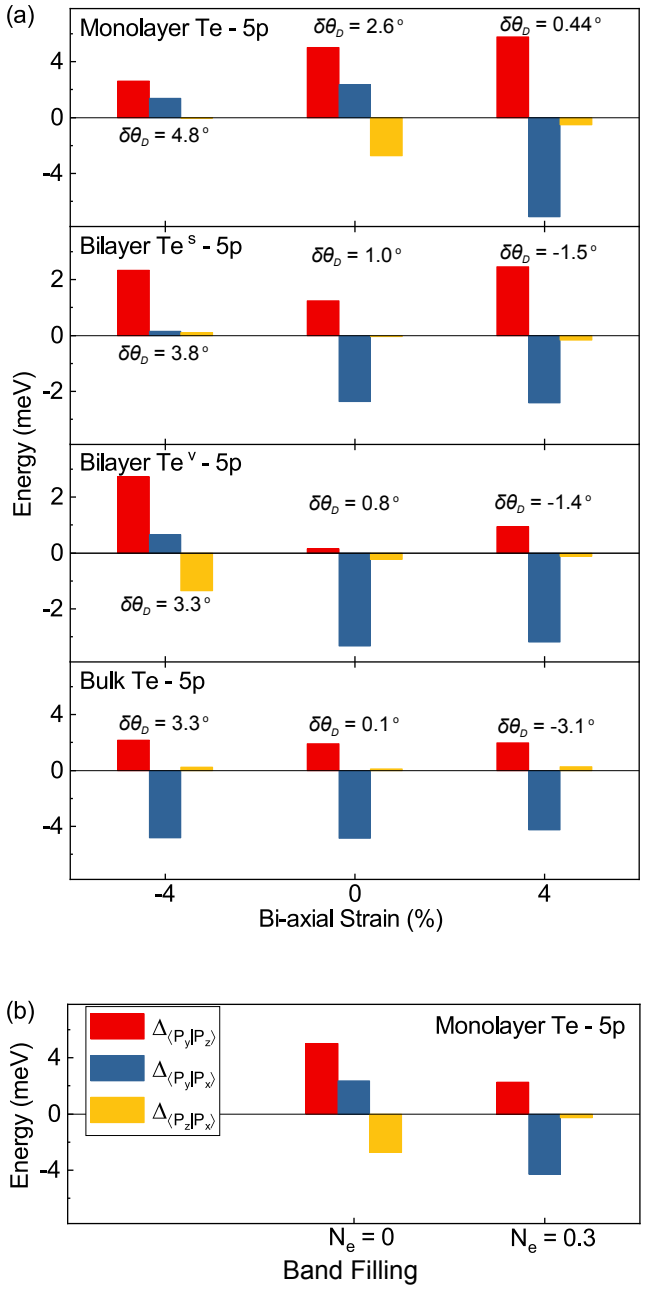

Figure 3.8: Difference in SOC matrix elements $\Delta_{\langle p_i|p_j\rangle}$ (per atom) of the Te-5p orbitals. (a) $\Delta_{\langle p_i|p_j\rangle}$ of 1L, 2L, and bulk 1T-$CrTe_2$ versus strain. At each strain, the values for $\delta\theta_D$ are also shown. Positive and negative values of strain correspond to tensile and compressive strain, respectively. For the bilayer, values for Te atoms at the van der Waals gap (Te^v) and Te atoms at the free surface Te^s are shown. (b) $\Delta_{\langle p_i|p_j\rangle}$ of 1L 1T-$CrTe_2$ versus filling. The legend is shown at left.

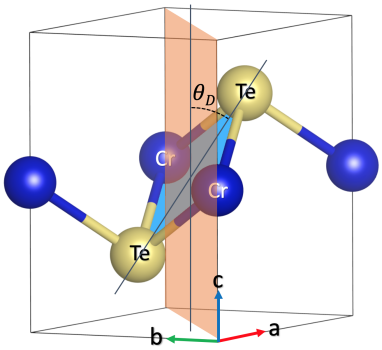

Figure 3.9: Illustration of the dihedral angle θ_D between the plane (blue) formed by a Cr-Te-Cr bonds and the perpendicular plane through the Cr-Cr pair (orange).

terms. The net result is that the MAE becomes dominated by the $\Delta_{\langle p_y|p_x\rangle}$ term, and the easy axis switches from out-of-plane to in-plane. In the band-filling calculation, the structure is not relaxed after charging, so all of the dihedral angles and bond angles remain the same as in the charge neutral state. Thus, this switching is a purely electronic effect.

The mechanism of strain and band filling's effect on the MAE can also be analyzed from the band structures with different magnetization directions. As shown in Fig. 3.10, when the magnetization direction in 1L 1T-$CrTe_2$ switches from $\hat{x}$ to $\hat{z}$, one of the occupied Te band around Γ moves to lower energy levels, which decreases the total energy and make $\hat{z}$ become the magnetic easy axis. This is the case illustrated in Fig. 2.1(c). The band structures of 1L 1T-$CrTe_2$ with +3% strain applied are shown in Fig. 3.12. When the magnetization axis turns from $\hat{x}$ to $\hat{z}$, one occupied Te band around Γ becomes partial unoccupied, another occupied Te band moves to lower energy levels. However, the electron redistribution makes other bands move to higher energy levels and eventually increases the total energy, which makes $\hat{x}$ the magnetic easy axis. This is similar to the case illustrated in Fig. 2.1(b). The band structures of 1T-$CrTe_2$ with -3% strain applied are shown in Fig.

3.12. This is similar to the case in unperturbated 1T-$CrTe_2$, they both have the $\hat{z}$ as the magnetic easy axis. As shown in Fig. 3.13, in the 1L 1T-$CrTe_2$ with 0.3 filled electrons per unit cell, when magnetization axis switches from $\hat{x}$ to $\hat{z}$, a complex electron redistribution happens and finally increases the total energy. Thus, its magnetic easy axis is $\hat{x}$. This is similar to the case illustrated in Fig. 2.1(d).

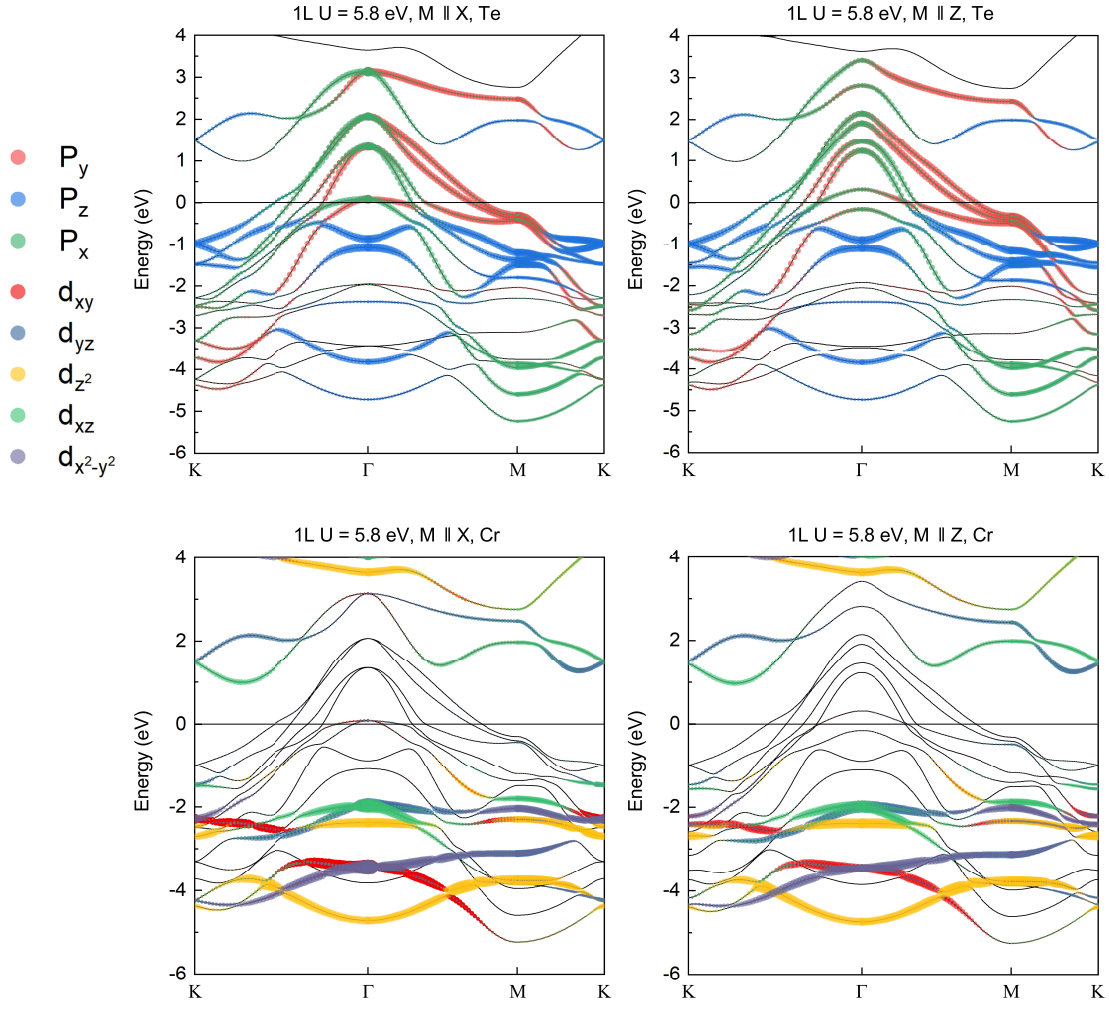

Figure 3.10: Band structures of 1L 1T-$CrTe_2$.

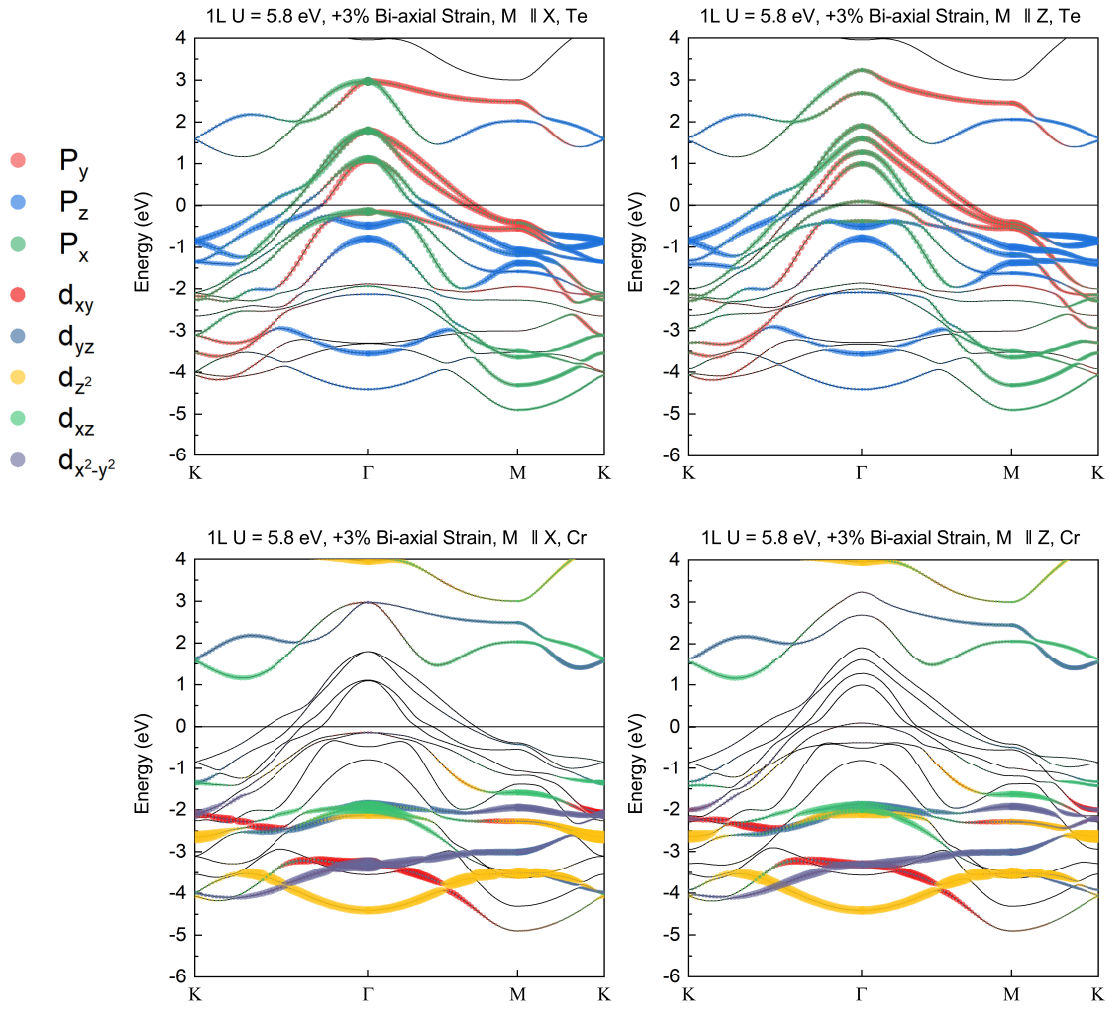

Figure 3.11: Band structures of 1L 1T-$CrTe_2$ with +3% bi-axial strain.

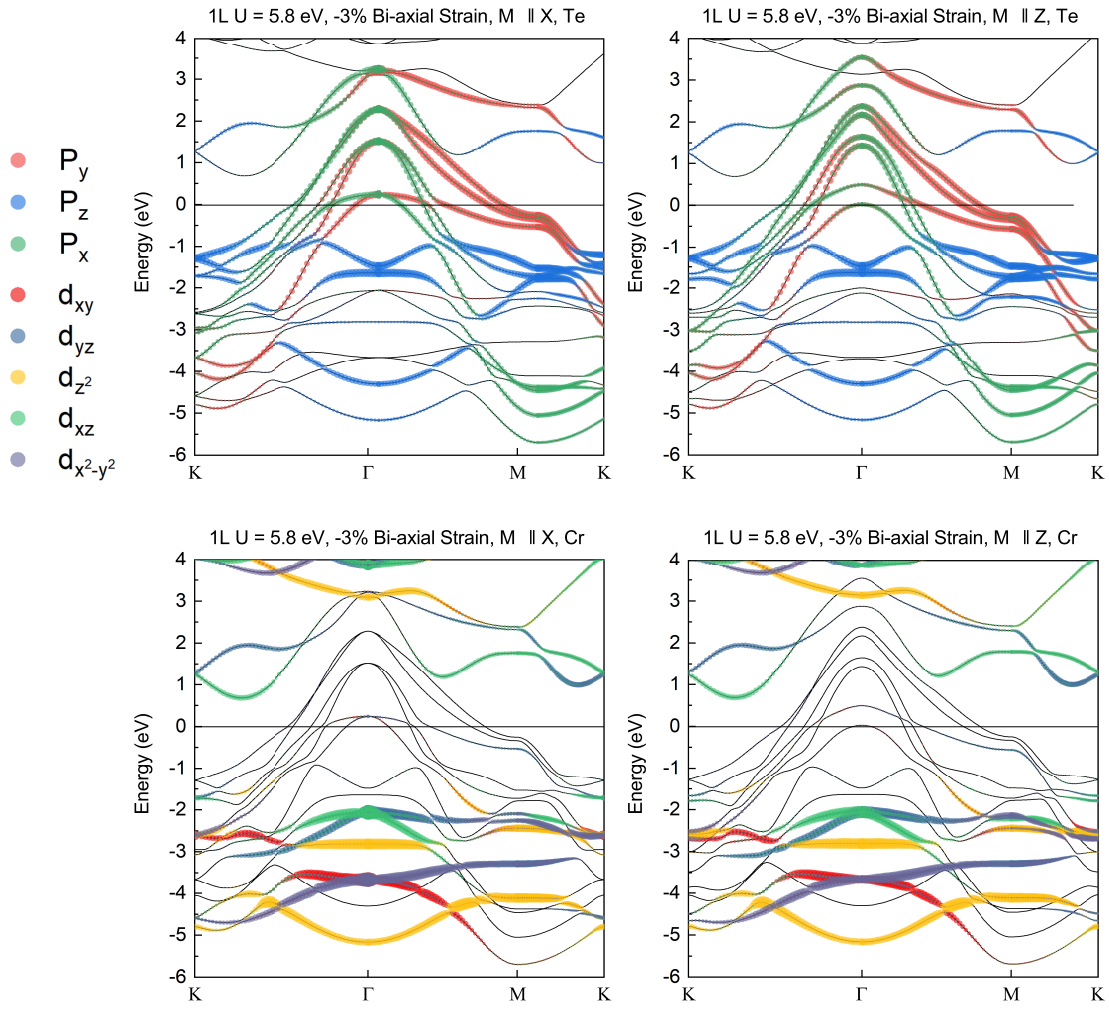

Figure 3.12: Band structures of 1L 1T-$CrTe_2$ with -3% bi-axial strain.

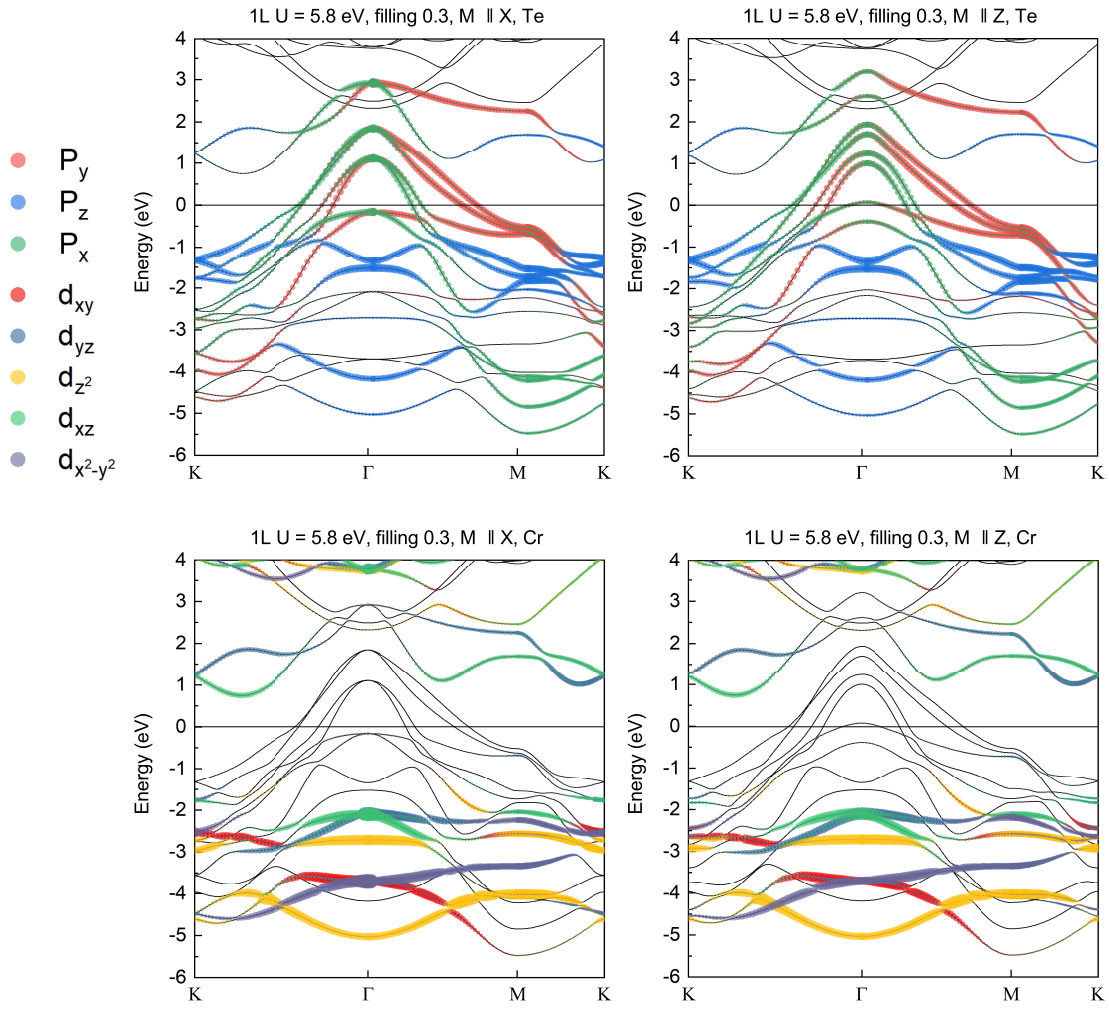

Figure 3.13: Band structures of 1L 1T-$CrTe_2$ with 0.3 electrons filled per unit cell.

3.3.3 XXZ Spin Hamiltonian

Magnetic anisotropy originating from the nonmagnetic ligand p electrons is induced by the superexchange mechanism [71, 70, 83] through the Cr-Te-Cr channel. Magnetic anisotropy of this kind is exchange anisotropy, in which the exchange coupling constants of the Heisenberg Hamiltonian depend on the directions of the magnetic moments. A suitable model is the XXZ Hamiltonian in which the the exchange coupling constant for the in-plane component of the spins J_{xy} differs from the out-of-plane component J_z [84]. This model has been shown to apply to CrI_3 [70]. Other sources of anisotropy include single ion anisotropy and dipolar coupling. The effect of dipolar coupling is known to be small, so below, we consider a XXZ type Hamiltonian for the energy per unit cell of monolayer 1T-$CrTe_2$ that also includes a single-ion anisotropy term and an external magnetic field directed in the $\pm z$ direction (along the c axis),

$$H = -J_{xy}\frac{1}{N}\sum_{i\neq j}(S_i^x S_j^x + S_i^y S_j^y) - J_z\frac{1}{N}\sum_{i\neq j}(S_i^z S_j^z)$$
$$- K_u\frac{1}{N}\sum_j (S_j^z)^2 + g\mu_B B_z\frac{1}{N}\sum_j S_j^z. \tag{3.6}$$

Since 1T-$CrTe_2$ is ferromagnetic, the exchange coupling constants J_{xy} and J_z are positive. For perpendicular magnetic anisotropy in a monolayer, K_u is positive. The spin magnetic moment $M_j^z = -g\mu_B S_j^z$, so that the last term is $-\frac{1}{N}\sum_j \mathbf{M}_j \cdot \mathbf{B}$ with $\mathbf{B}$ directed along the $\pm z$ direction. Exchange coupling is included for nearest neighbor Cr ions.

The magnon dispersion is determined by first performing the Holstein-Primakoff transformation [85] defined by the operator substitution $S_j^z = S - \hat{n}_j$, where $\hat{n}_j = a_j^\dagger a_j$ is the magnon number operator. One can then show that the spin ladder operators, $S_j^+ = S_j^x + iS_j^y$

and $S_j^- = S_j^x - iS_j^y$, are given by $S_j^+ = \sqrt{2S}\sqrt{1-\frac{\hat{n}_j}{2S}}\, a_j$, and $S_j^- = \sqrt{2S}a_j^\dagger\sqrt{1-\frac{\hat{n}_j}{2S}}$. At low temperatures such that $\langle \hat{n}_j \rangle \ll S$, one expands out the square root terms to first order in $\hat{n}_j$ to obtain

$$\begin{aligned} \hat{S}_j^z &= S - \hat{n}_j \\ \hat{S}_j^+ &\approx \sqrt{2S}\left(1 - \frac{\hat{n}_j}{4S}\right) a_j \\ \hat{S}_j^- &\approx \sqrt{2S} a_j^\dagger \left(1 - \frac{\hat{n}_j}{4S}\right) \end{aligned} \tag{3.7}$$

These are the equations used to transform the Hamiltonian in Eq. (3.12). Keeping terms to first order in $\hat{n}_j$, and substituting the Fourier representation of the operators $a_j = \frac{1}{\sqrt{N}}\sum_{\mathbf{k}} e^{-i\mathbf{k}\cdot\mathbf{R}_j} a_{\mathbf{k}}$ (see SM for details), the Hamiltonian governing the magnon dynamics is

$$H_m = \frac{2S}{N}\sum_{\mathbf{k}} \left[J_z Z + K_u - \frac{g\mu_B B_z}{2S} - J_{xy}\mathrm{Re}\{f(\mathbf{k})\} \right] a_{\mathbf{k}}^\dagger a_{\mathbf{k}}, \tag{3.8}$$

where $Z = 6$ is the number of nearest neighbor Cr atoms, and $f(\mathbf{k}) \equiv \sum_{\boldsymbol{\delta}} e^{-i\mathbf{k}\cdot\boldsymbol{\delta}} \in \mathbb{R}$ is the form factor resulting from the sum over the 6 nearest Cr neighbors located at the vertices of the hexagon given explicitly by $f(\mathbf{k}) = 2\left[\cos(k_x a) + 2\cos\left(\frac{k_x a}{2}\right)\cos\left(\frac{\sqrt{3}}{2}k_y a\right)\right]$. In the limit of small ka, the magnon energy given by Eq. (3.8) reduces to

$$E_m(k) = 12S\left(J_z - J_{xy}\right) + 2SK_u - g\mu_B B_z + 3SJ_{xy}k^2a^2. \tag{3.9}$$

The parameters J_{xy}, J_z, and K_u are extracted from the DFT calculated total energies of structures with different spin configurations as shown in Fig. 3.14. From the Hamiltonian of Eq. (3.6), the total energies for each spin configuration for two unit cells (2 Cr atoms) are $E_{FM,z} = 24S^2J_z + 2S^2K_u + E_0$, $E_{AFM,z} = -4S^2J_z + 2S^2K_u + E_0$, $E_{FM,x} = 12S^2J_{xy} + E_0$, and $E_{AFM,x} = -4S^2J_{xy} + E_0$.

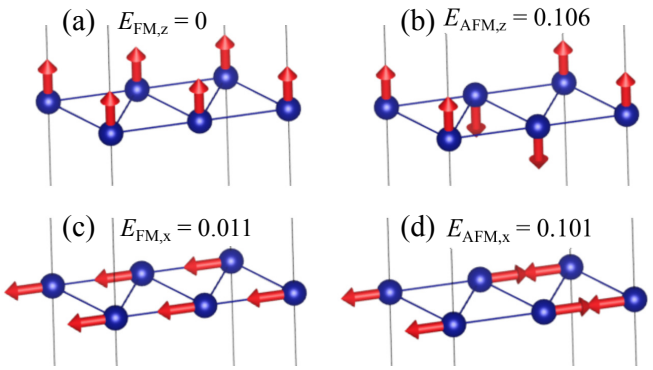

Figure 3.14: Different spin configurations in a $2 \times 1 \times 1$ supercell, showing only the Cr atoms, used for determining the exchange and anisotropy parameters in Eq. (3.6). The 2×1 supercell is shown with the solid black line. Nearest neighbors for the 2 atoms in the supercell are shown with the thinner blue lines. The total energy (in eV) with respect to $E_{FM,z}$ is shown for each spin configuration.

The exchange and anisotropy constants are obtained as follow:

$$J_{xy} = (E_{FM,x} - E_{AFM,x})/(16S^2)$$

$$J_z = (E_{FM,z} - E_{AFM,z})/(16S^2)$$

$$K = (E_{FM,z} - E_{FM,x} - 12J_zS^2 - 12J_{xy}S^2)/(2S^2). \tag{3.10}$$

The values obtained with $U = 5.8$ eV are $J_z = 2.93$ meV, $J_{xy} = 2.50$ meV, and K_u = -0.0959 meV.

Eq. (3.9) shows that the effective anisotropy governing the spin gap in the magnon dispersion is

$$K_{\text{eff}} = (J_z - J_{xy})Z + K_u = 2.49 \text{ (meV)}. \tag{3.11}$$

We can confirm the assumption that the dipolar energy can be neglected, since an estimate for the magnitude of the dipolar energy is $\frac{\mu_0}{2}M_s^2 = \frac{\mu_0}{2}(g\mu_B S)^2 V_{uc} = 41$ μeV, where V_{uc} is the volume of one unit cell. This is one order of magnitude smaller than the effective anisotropy energy. With the definition of K_{eff}, the XXZ Hamiltonian of Eq. (3.6) maps

onto a Heisenberg Hamiltonian with isotropic exchange and single-ion anisotropy as

$$H = \frac{-J}{N}\sum_{i\neq j}\mathbf{S}_i\cdot\mathbf{S}_j - \frac{K_{\text{eff}}}{N}\sum_j (S_j^z)^2 + g\mu_B B_z \frac{1}{N}\sum_j S_j^z, \tag{3.12}$$

where $J = J_{xy}$, and the low energy magnon dispersion becomes

$$E_m(k) = 2SK_{\text{eff}} - g\mu_B B_z + 3SJk^2a^2. \tag{3.13}$$

Since the effect of anisotropic exchange and single ion anisotropy enter the equations governing the observables of magnetic anisotropy and magnon dispersion in exactly the same way, experimental measurements of effective anisotropy energies, spin-wave gaps, and the resulting transition temperatures do not help to separate these two effects. However, the experimental measurements of effective anisotropy and transition temperature can shed light on the relative magnitudes of J and K_{eff}. Two seperate experimental investigations extracted effective anisotropy constants from magnetization versus field curves of $K_{\text{exp}} = 5.6$ Merg/cm^3 $= 0.26$ meV/u.c., where, for the conversion, we use the volume of the bulk unit cell [15, 55]. The experimentally measured Curie temperatures of few layer 1T-$CrTe_2$ range from $T_c \sim 200 - 300$ K [13, 55, 56, 57]. From the value of K_{exp} and the range of values for T_c, we can extract a range of values for J using renormalized spin wave theory (RWST) [86, 70, 49].

Starting from the operator identity $S_j^z = S - \hat{n}_j$ and the saturation magnetization per unit cell $M_s = g\mu_B S$, the expected value of the magnetization as a function of temperature is

$$M(T) = M_s - g\mu_B \frac{1}{N}\sum_{\mathbf{k}}\langle\hat{n}_{\mathbf{k}}\rangle \tag{3.14}$$

where $\langle\hat{n}_{\mathbf{k}}\rangle = [e^{E_m(k)/k_BT} - 1]^{-1}$ is given by the Bose-Einstein factor. The renormalization is included by replacing S in the dispersion relation by $S - \frac{1}{N}\sum_{\mathbf{k}}\langle\hat{n}_{\mathbf{k}}\rangle = \frac{M(T)}{g\mu_B}$. With

this substitution, and using the expression for the low-energy dispersion (Eq. (3.13)), the equation for $M \equiv M(T)$ in units of μ_B becomes

$$M = M_s - \frac{gA_{uc}}{2\pi}\int_0^{k_{max}} dk \, \frac{k}{e^{\frac{M}{g}(2K_{\text{eff}}+3Jk^2a^2)/k_BT} - 1}, \tag{3.15}$$

where the sum over the two dimensional wavevector is converted into an integral, $A_{uc} = a^2\sqrt{3}/2$ is the area of a unit cell, and k_{max} is chosen to match the area of the first Brillouin zone, i.e. $\pi k_{max}^2 = \left(\frac{4\pi}{3a}\right)^2 \sqrt{3}/2$. Performing the integral gives

$$\frac{M}{g} = \frac{M_s}{g} - \frac{\sqrt{3}k_BT}{24\pi\frac{M}{g}J} \ln\left[\frac{1 - e^{-E_{\text{max}}/k_BT}}{1 - e^{-E_{\text{min}}/k_BT}}\right] \tag{3.16}$$

where $E_{\text{min}} = 2\frac{M}{g}K_{\text{eff}}$ and $E_{\text{max}} = E_{\text{min}} + \frac{8\pi}{\sqrt{3}}\frac{M}{g}J$.

Eq. (3.16) is solved for M, and $M(T)$ is plotted versus T in Fig. 3.15 with $J = 2.5$ meV and four different values of K_{eff}. The solid red curve with $T_c = 405$ K results from the DFT calculated parameters of $K_{\text{eff}} = 2.49$ meV and $J = 2.50$ meV. The other curves show the effect of reducing K_{eff}. As K_{eff} is reduced by factors of 2, 5, and 10, T_c decreases from 405 K to 311 K, 234 K, and 197 K, respectively. These curves illustrate the sensitivity of T_c to the parameters J and K_{eff}.

The pairs of parameters J and K_{eff} that result in a given value for T_c form a curve in the two dimensional $J - K_{\text{eff}}$ parameter space. We solve for that curve by setting $T = T_c$ and $M = 1.65\mu_B$ in Eq. (3.16). The value of $M = 1.65\mu_B$ is chosen, since we find it to be at the point, or extremely close to the point, where the maximum temperature occurs in all of the $M(T)$ versus T curves such as those shown in Fig. 3.15. The $J - K_{\text{eff}}$ curves showing all parameter pairs resulting in $T_c = 200$ K and $T_c = 300$ K calculated from Eq. (3.16) are shown in Fig. 3.16.

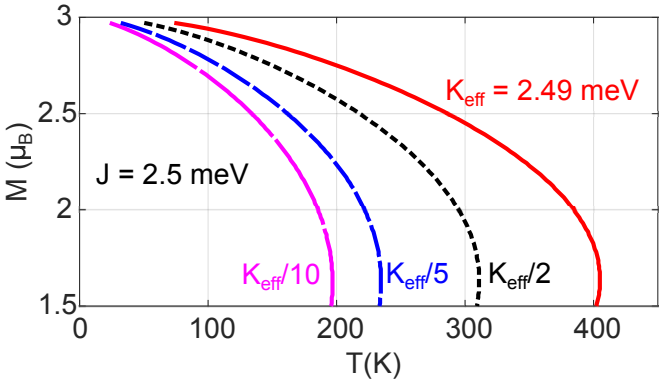

Figure 3.15: Magnetization versus temperature with $J = 2.5$ meV and four different values of K_{eff} as shown on the plot.

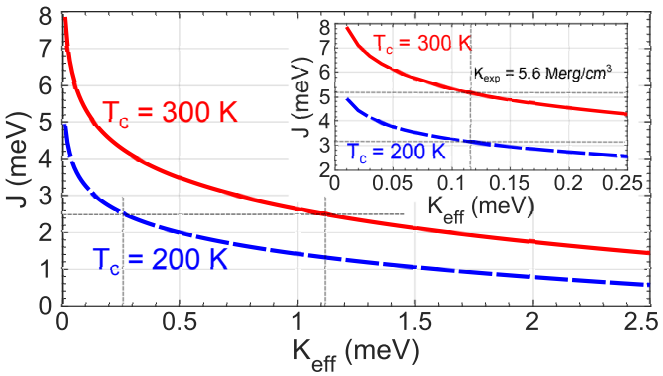

Figure 3.16: Values of J and K_{eff} that result in $T_c = 300$ K and 200 K calculated from Eq. (3.16). Inset: Enlarged view for small K_{eff}. To convert to values for experimentally determined anisotropy, $K_{\text{exp}} = S^2 K_{\text{eff}} = 2.25 K_{\text{eff}}$. The vertical dashed line in the inset designates the experimentally measured $K_{\text{exp}} = 5.6$ Merg/cm^3.

The expression $K_{\text{exp}} = -\frac{\mu_0 H_s M_s}{2}$ used to extract K_{exp} from experimental magnetization curves [55] is derived from the formula for the angular dependence of the energy of a magnetic thin film in the presence of an applied field H, $E = -K_{\text{exp}} \cos^2(\theta) - \mu_0 M_s H \cos(\phi - \theta)$, where ϕ and θ are the polar angles of the magnetic field and the magnetization, respectively [87]. Minimizing E with respect to θ, and letting H be in-plane, so that $\phi = \pi/2$, gives $K_{\text{exp}} = -\frac{\mu_0 H_s M_s}{2}$, where H_s is the saturation field. The angular dependence of our Heisenberg Hamiltonian with an arbitrary direction for B comes

from the two terms, $-K_{\text{eff}}(S^z)^2 + g\mu_B\mu_0\mathbf{H}\cdot\mathbf{S}$. Writing S as a classical vector gives $-K_{\text{eff}}S^2\cos^2(\theta) - \mu_0 H M_s\cos(\phi-\theta)$ where $\mathbf{M}_s = -g\mu_B\mathbf{S}$. Minimizing as before gives $K_{\text{eff}} = -\frac{\mu_0 H_s M_s}{2S^2}$, so that $K_{\text{eff}} = K_{\text{exp}}/S^2$.

The one experimental value of $K_{\text{exp}} = 5.6$ Merg/cm^3 is marked by the dashed vertical line on the inset. The experimentally measured range of T_c values between 200 K and 300 K then provides a range of J values between 3.1 meV and 5.2 meV. The dashed horizontal line on the main plot shows the DFT calculated value of $J = 2.5$ meV, which is slightly below the minimum extracted value from the experimental data. The calculated $K_{\text{eff}} = (J_z - J_{xy})Z = 2.5$ meV is too large. It is a result of the large value of magnetic anisotropy energy, $\Delta_{\text{MA}} = 5.56$ meV, and the large coordination number, $Z = 6$. We note that our values for Δ_{MA} are similar to and somewhat less than those calculated in Ref. [56] with similar values of U.

Care is required when comparing to other values for K_{eff} and J in the literature. Some authors define their Heisenberg Hamiltonian as $\frac{J'}{2}\sum_{i\neq j}\mathbf{S}_i\cdot\mathbf{S}_j$ [70, 88], in which case, their values for J must be scaled by a factor of 2 for comparison with our values. Many authors set $S = 1$ when extracting exchange constants from the DFT total energy calculations [63, 65] while other authors do not [70, 88]. Values for J' calculated with $S = 1$ must be scaled by S^2 to compare with our values for J, i.e. $J = J'/S^2$. The same also holds true for the anisotropy constant K. Below, we compare to other values in the literature appropriately scaled (i.e. by a factor of $\frac{1}{2}$ or by a factor of $S^2 = \frac{9}{4}$) to match the definition of our values, and we also convert to our sign convention in which positive J and K values correspond to FM coupling and PMA, respectively. Based on PBE+$U = 2$ eV total

energy calculations of ML 1T-$CrTe_2$ and fitting to a symmetric second neighbor Heisenberg model with single-ion anisotropy, Ref. [63] found a nearest neighbor exchange interaction of $J_1 = 5.9$ meV, a second neighbor interaction of $J_2 = 1.1$ meV, and an anisotropy constant of $K = -0.46$ meV. We note the large value of J_1, however, since the magnetic anisotropy is in-plane, RWST predicts $T_c = 0$ K. As noted above, ML CrI_3 has many similarities to ML $CrTe_2$ such as octahedral coordination, anions with large SOC, and PMA. PBE+U = 2.7 eV calculations of ML CrI_3 found $J = 1.1$ meV and $K_{\text{eff}} = 0.045$ meV [70]. The lower values are consistent with the lower value of T_c for CrI_3 with respect to that of $CrTe_2$. In general, the exchange constants straddle the ones predicted from experimental data analysed with RWST. The predicted anisotropy constants tend to have a stronger dependence and even change sign depending on the value of U.

3.4 Conclusions

In this study, we performed a systematic first principle DFT calculations of the structural, electronic, and magnetic properties of various phases of $CrTe_2$. A comparison of the formation energies of the different phases of $CrTe_2$ show that the 1T-$CrTe_2$ phase is the ground state. For the bulk and monolayer, the formation energy of the 1T phase lies 0.30 eV and 0.11 eV per formula unit below the next metastable phase, respectively. Furthermore, NEB calculations show that the energy barriers separating the phases are large, on the order of 0.5 eV for both the bulk and monolayer. Based on the linear response method, the calculated U value for the Cr atom in 1T-$CrTe_2$ is 5.8 eV. The magnetic anisotropy of 1T-$CrTe_2$ originates from the SOC of the Te atoms and the superexchange coupling between

the Cr-3d and Te-5p orbitals. For any number of layers ($n \geq 2$) of 1T-$CrTe_2$, the magnetic moment lies in-plane, however for a monolayer, the magnetic moment is out-of-plane. Band filling with a sheet carrier concentration more than $n_s = 1.5 \times 10^{14}$ cm^{-2} or a tensile bi-axial strain of 3% can cause the magnetic easy axis of monolayer 1T-$CrTe_2$ switch from out-of-plane to in-plane. Compressive bi-axial strain of -3%, causes the magnetic easy axis of bilayer 1T-$CrTe_2$ to switch from in-plane to out-of-plane. PMA is favored in structures with smaller dihedral angles consistent with the trend identified previously for CrI_3. An RWST analysis using experimental values for magnetic anisotropy and T_c, provides a range of expected values for the nearest neighbor exchange constant lying between 3.1 meV and 5.2 meV for values of T_c in the range of 200 K and 300 K, respectively.

3.5 Acknowledgments

This work was supported in part by the U.S. Army Research Laboratory (ARL) Research Associateship Program (RAP) Cooperative Agreement(CA) W911NF-16-2-0008. This work used the Extreme Science and Engineering Discovery Environment (XSEDE) [89], which is supported by National Science Foundation Grant No. ACI-1548562 and allocation ID TG-DMR130081. YL acknowledges helpful discussions with Prof. Ran Cheng.

Chapter 4

Layer and Symmetry Dependent Magnetism in Self-intercalated vdW Ferromagnet $Cr_{1+x}Te_2$

4.1 Introduction

Achieving long-range magnetism at low dimensions at high temperatures is of great importance for novel spintronics. According to the Mermin-Wagner theorem [7], magnetic anisotropy has a critical role in stabilizing long-range magnetic ordering in the two dimensional (2D) limit. From the perspective of applications, the perpendicular magnetic anisotropy (PMA) is more desired than the in-plane anisotropy. Previous studies showed PMA's advantages in scalability, thermal stability, and low switching current density [90, 91].

Recently, 2D ferromagnetism was observed in van der Waals (vdW) CrI_3 [9], however its low Curie temperature $T_C = 45$ K has limited its potential in spintronics. Binary chromium telluride $Cr_{1+x}Te_2$ including Cr_2Te_3 [14, 16, 17, 18], Cr_4Te_5 [19], Cr_5Te_8 [20, 21], $Cr_{5+x}Te_8$ [22], and $Cr_{12-x}Te_{16}$ [23] are promising candidates with high T_C ranging between 170 and 350K. The notation $Cr_{1+x}Te_2$ represents all the compounds with different fractions of Cr atoms self-intercalated between neighboring $CrTe_2$ layers. Compared to the ferromagnetic (FM) ordering in $CrTe_2$, more complicated magnetism are observed in $Cr_{1+x}Te_2$ such as antiferromagnetic (AFM) interaction, noncollinear spin textures, and tunable magnetic anisotropy [15, 23, 14]. $Cr_{1+x}Te_2$ is composed of alternating $CrTe_2$ and intercalated Cr layers. However, the absence of studying the effect of $Cr_{1+x}Te_2$'s surface layer type on its stability and magnetic properties has limited its potential for spintronics.

In this work, we investigate the evolution of formation energy as the number of $CrTe_2$ and intercalated Cr layers increase. The magnetic ground state and exchange coupling constants of $Cr_{1+x}Te_2$ are studied by calculating the energies of different magnetic configurations. The magnetic anisotropy is studied by performing DFT calculation with spin-orbit coupling. Finally, we analyze the effect of bi-axial strain on the exchange coupling constants in $Cr_{1+x}Te_2$.

4.2 Computational method

We performed first-principle calculations within the framework of density functional theory using the projector augmented wave (PAW) [73, 74] method and a plane-wave basis, as implemented in the Vienna ab initio simulation package (VASP) [67, 68]. The ex-

change correlation is included with the Perdew-Burke-Enzerhof's (PBE) [37] version of the generalized gradient approximation (GGA) functional. The DFT-D3 method [75] is used to model the vdW interactions between the layers of Cr_2Te_3. For finite thickness slabs, 15 Å vacuum layers are added to avoid interactions between the periodically repeated layers. A plane-wave basis cutoff of 500 eV is used. The energy convergence of self-consistent electronic loops is 10^{-8} eV. All structures are relaxed until the force on each atom is smaller than 0.01 eV/Å. A 8×8×4 Monkhorst-Pack k-grid mesh [80] for the bulk structure and a 8×8×1 k-grid mesh for the layers are used in the structural relaxation. To ensure that the magnetic anisotropy energies are well converged, a 17×17×8 k-grid mesh is used for bulk structure and a 17×17×1 mesh is used for layers in magnetic anisotropy calculations. Due to Cr_2Te_3's metallic band structure, the Methfessel-Paxton smearing method is used with a width of 0.1 eV. For calculation of the electronic and magnetic properties, the Hubbard U correction (DFT+U) [39] is included. A typical U value of 3.5 eV for the Cr atom is used. The Heisenberg Hamiltonian is used in extracting exchange coupling constants between neighboring Cr atoms. The spin number $S = \frac{3}{2}$ is used for Cr in exchange coupling constants calculations.

4.3 Results

4.3.1 Structural properties

Self-intercalated $Cr_{1+x}Te_2$ is composed of alternating $CrTe_2$ layers and intercalated Cr layers. Its bulk form has the chemical formula Cr_2Te_3, thus this material is commonly called Cr_2Te_3. Due to the alternating layers, the layered $Cr_{1+x}Te_2$ have three different

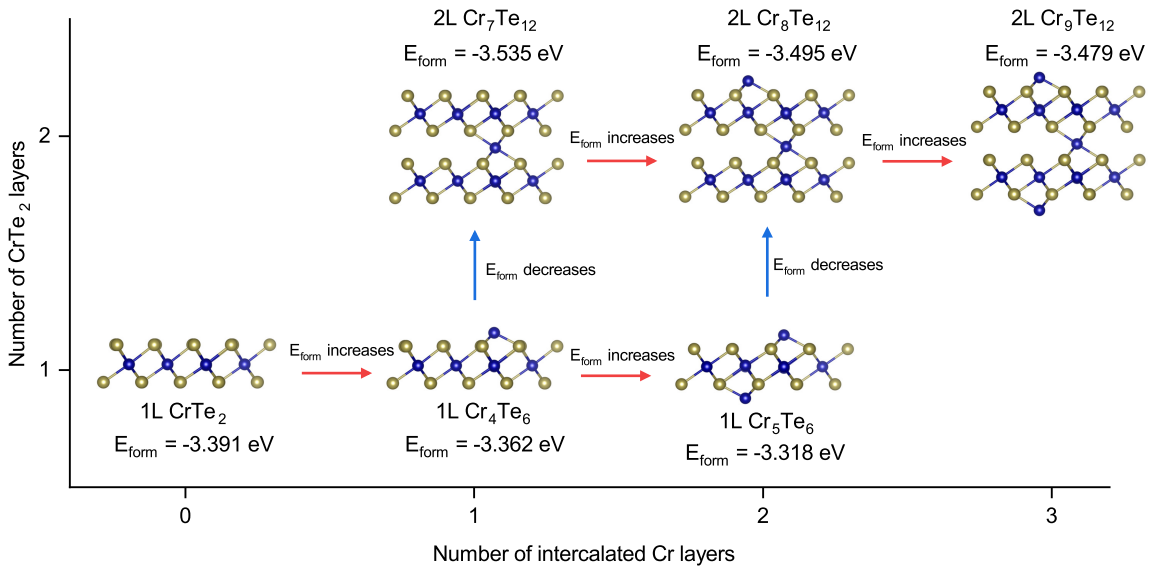

Figure 4.1: Structural evolution of layered $Cr_{1+x}Te_2$. Red arrows represent E_{form} increases and the material becomes less table. Blue arrows represent E_{form} increases and the material becomes more stable.

types of surfaces: (1) Both surfaces are $CrTe_2$ layers, (2) Both surfaces are intercalated Cr layers, and (3) One surface is $CrTe_2$ layer and the other surface is intercalated Cr layer. In addition to the surface type, the number of layers also gives variety to the structure of $Cr_{1+x}Te_2$.

To figure out the stable surface types of $Cr_{1+x}Te_2$, we calculated the formation energy per atom E_{form} as the structure evolves from the single layer (1L) $CrTe_2$ to the bi-layer (2L) Cr_9Te_{12} as shown in Fig. 4.1. The top view of $Cr_{1+x}Te_2$ is shown in Fig. 4.2. The optimized lattice constants are shown in Table. 4.1. It is found that adding an intercalated Cr layer always increases E_{form}, however adding a $CrTe_2$ layer decreases E_{form}. Lower E_{form} indicates better structural stability. Thus, we can conclude that the $Cr_{1+x}Te_2$ is more stable when both surfaces are $CrTe_2$ layers. However, $Cr_{1+x}Te_2$ with intercalated

Cr layers on the surface can also exist as the meta-stable phase.

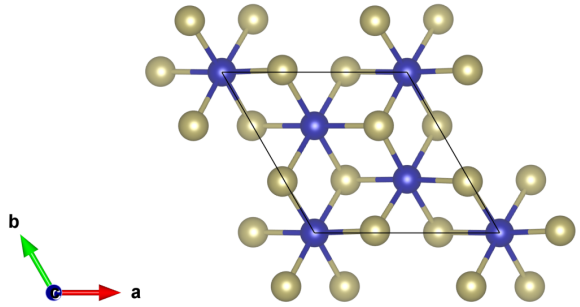

Figure 4.2: Top view of the $Cr_{1+x}Te_2$

Table 4.1: Optimized lattice constants of $Cr_{1+x}Te_2$

	1L $CrTe_2$	1L Cr_4Te_6	1L Cr_5Te_6	2L Cr_7Te_{12}	2L Cr_8Te_{12}	Bulk Cr_2Te_3
Lattice constant (Å)	6.645	6.569	6.850	6.685	6.711	6.800

The symmetry also varies as number of layers increases. In 1L $CrTe_2$, the inversion centers at Cr sites and the middle point of two adjacent Cr sites. The 1L Cr_4Te_6 has an intercalated Cr layer on one side, which breaks the inversion symmetry. The 1L Cr_5Te_6 has inversion symmetry, but its inversion centers are only located in the middle point of two adjacent Cr sites. The inversion centers in 2L Cr_7Te_{12} are at the intercalated Cr sites but not in the $CrTe_2$ layers. The 2L Cr_8Te_12 has twice more atoms than 1L Cr_4Te_6 in the unit cell. It either does not have inversion symmetry because the two surface layers are of different types. The two surface layers in 2L Cr_9Te_12 are both intercalated Cr layers, the inversion centers are at the Cr sites in the middle intercalated layer.

4.3.2 Magnetic properties

The magnetic ground state and exchange coupling constants are studied by calculating the energies of different magnetic configurations. The 3 types of Cr atoms in bulk Cr_2Te_3 are colored in different colors, as shown in Fig. 4.3(a). Different magnetic configurations of bulk Cr_2Te_3 and the energies with respect to the energy of the FM configuration E_{FM} are shown in Fig. 4.3(b) - (f).

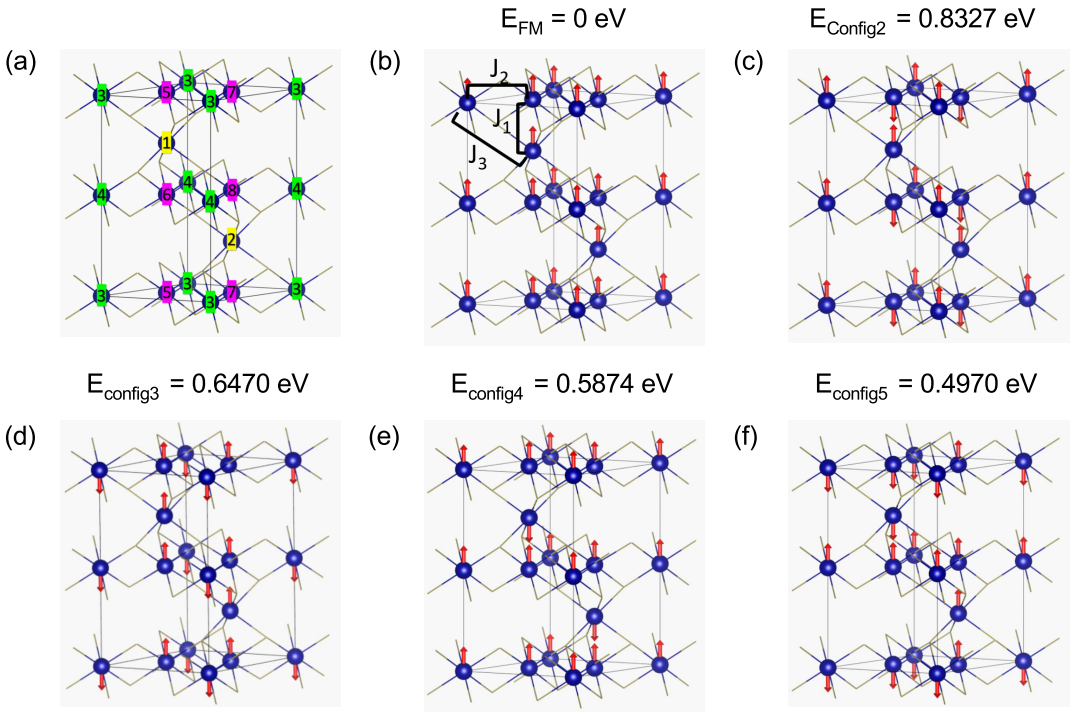

Figure 4.3: Magnetic configuration of bulk Cr_2Te_3

The following expressions are used to calculate the exchange coupling constants J_1, J_2, and J_3.

$$
\begin{aligned}
E_{FM} &= E_0 + S^2(8J_1 + 36J_2 + 48J_3) \\
E_{config2} &= E_0 + S^2(-8J_1 - 12J_2) \\
E_{config3} &= E_0 + S^2(8J_1 - 12J_2) \\
E_{config4} &= E_0 + S^2(-8J_1 + 36J_2 - 48J_3) \\
E_{config5} &= E_0 + S^2(4J_1 + 12J_2 - 12J_3) \\
J_3 &= (3E_{FM} + 2E_{config2} - E_{config4} - 4E_{config5})/(240S^2) \\
J_2 &= (E_{config4} - E_{config2} + 48J_3)/(48S^2) \\
J_1 &= (E_{config1} - E_{config4} - 96J_3)/(16S^2)
\end{aligned} \tag{4.1}
$$

The calculated results of exchange coupling constants and magnetic moments on Cr atoms are shown in Table. 4.2.

Table 4.2: Exchange coupling constants and magnetic moments in bulk Cr_2Te_3

	Energy (meV)
J_1	-6.20
J_2	-3.96
J_3	-1.68

Cr Atom	Magnetic moment (μB)
1, 2	3.152
3, 4	2.999
5, 6, 7, 8	3.062

The bulk Cr_2Te_3 has the in-plane magnetic anisotropy with a tiny anisotropic energy $E_{MAE} = E_x - E_z$ of -0.065 meV per Cr atom.

The 3 types of Cr atoms in 1L Cr_4Te_6 are colored in different colors, as shown in Fig. 4.4(a). Different magnetic configurations of 1L Cr_4Te_6 and the energies with respect to the energy of the FM configuration E_{FM} are shown in Fig. 4.4(b) - (f).

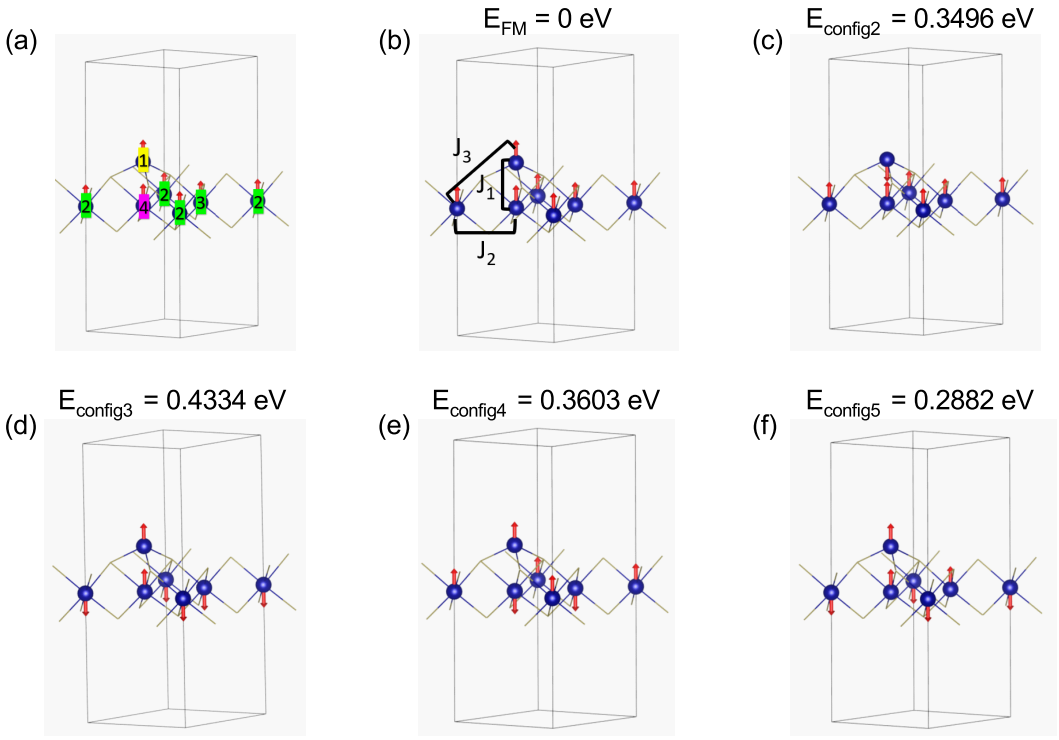

Figure 4.4: Magnetic configurations of 1L Cr_4Te_6

The following expressions are used to calculate the exchange coupling constants J_1, J_2, and J_3.

$$
\begin{aligned}
E_{FM} &= E_0 + S^2(2J_1 + 18J_2 + 12J_3) \\
E_{config2} &= E_0 + S^2(-2J_1 + 18J_2 - 12J_3) \\
E_{config3} &= E_0 + S^2(2J_1 - 6J_2 - 12J_3) \\
E_{config4} &= E_0 + S^2(-2J_1 - 6J_2) \\
E_{config5} &= E_0 + S^2(2J_1 - 6J_2) \\
J_1 &= (E_{config5} - E_{config4})/(4S^2) \\
J_3 &= (E_{FM} - E_{config2} - 4J_1)/(24S^2) \\
J_2 &= (E_{FM} - E_{config5} - 12J_3)/(24S^2)
\end{aligned} \tag{4.2}
$$

The calculated results of exchange coupling constants and magnetic moments on Cr atoms are shown in Table. 4.3.

Table 4.3: Exchange coupling constants and magnetic moments in 1L Cr_4Te_6

	Energy (meV)
J_1	-8.00
J_2	-2.77
J_3	-5.14

Cr Atom	Magnetic moment (μB)
1	3.608
2, 3	3.013
4	3.098

The 1L Cr_4Te_6 has the perpendicular magnetic anisotropy with an anisotropic energy $E_{MAE} = E_x - E_z$ of 0.75 meV per Cr atom.

The 3 types of Cr atoms in 1L Cr_5Te_6 are colored in different colors, as shown in Fig. 4.5(a). Different magnetic configurations of 1L Cr_5Te_6 and the energies with respect to the energy of the FM configuration E_{FM} are shown in Fig. 4.5(b) - (f).

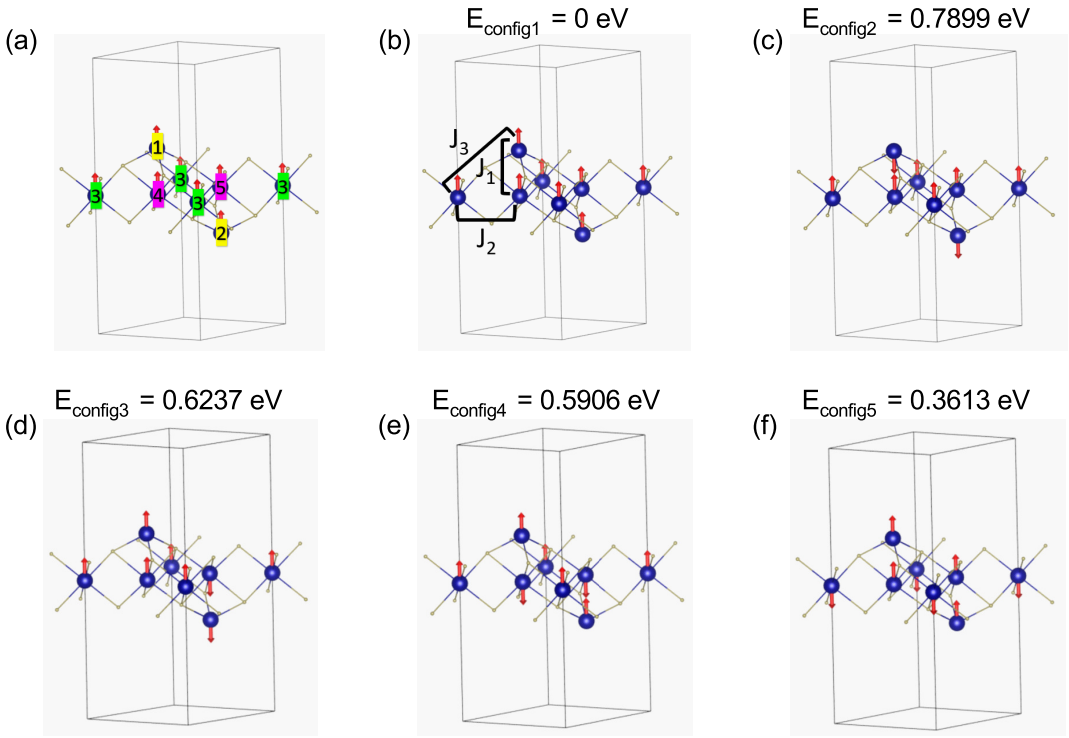

Figure 4.5: Magnetic configurations of 1L Cr_5Te_6

The following expressions are used to calculate the exchange coupling constants J_1, J_2, and J_3.

$$
\begin{aligned}
E_{FM} &= E_0 + S^2(4J_1 + 18J_2 + 24J_3) \\
E_{config2} &= E_0 + S^2(-4J_1 + 18J_2 - 24J_3) \\
E_{config3} &= E_0 + S^2(4J_1 - 6J_2 - 12J_3) \\
E_{config4} &= E_0 + S^2(-4J_1 - 6J_2) \\
E_{config5} &= E_0 + S^2(4J_1 - 6J_2) \\
J_1 &= (E_{config5} - E_{config4})/(8S^2) \\
J_3 &= (E_{FM} - E_{config2} - 8J_1)/(48S^2) \\
J_1 &= (E_{FM} - E_{config3} - 36J_3)/(24S^2)
\end{aligned} \tag{4.3}
$$

The calculated results of exchange coupling constants and magnetic moments on Cr atoms are shown in Table. 4.4.

Table 4.4: Exchange coupling constants and magnetic moments in 1L Cr_5Te_6

	Energy (meV)
J_1	-12.74
J_2	-3.76
J_3	-5.19

Cr Atom	Magnetic moment (μB)
1, 2	3.736
3	3.209
4, 5	3.270

The 1L Cr_5Te_6 has the in-plane magnetic anisotropy with an anisotropic energy $E_{MAE} = E_x - E_z$ of -2.39 meV per Cr atom.

The 3 types of Cr atoms in 2L Cr_7Te_{12} are colored in different colors, as shown in Fig. 4.6(a). Different magnetic configurations of 2L Cr_7Te_{12} and the energies with respect to the energy of the FM configuration E_{FM} are shown in Fig. 4.6(b) - (f).

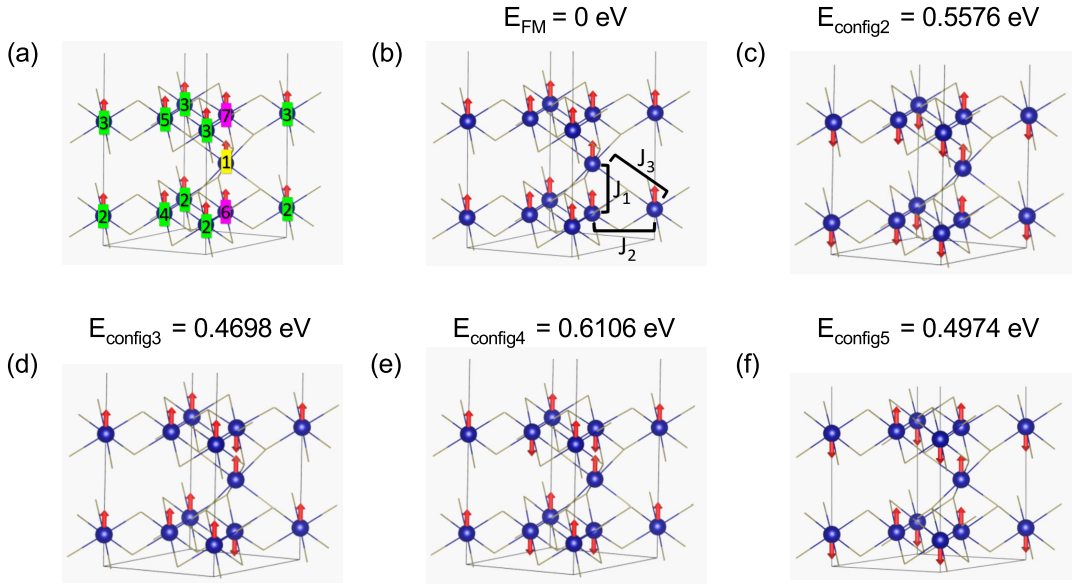

Figure 4.6: Magnetic configurations of 2L Cr_7Te_{12}

The following expressions are used to calculate the exchange coupling constants J_1, J_2, and J_3.

$$
\begin{aligned}
E_{FM} &= E_0 + S^2(4J_1 + 36J_2 + 24J_3) \\
E_{config2} &= E_0 + S^2(4J_1 - 12J_2 - 24J_3) \\
E_{config3} &= E_0 + S^2(-4J_1 - 12J_2 + 24J_3) \\
E_{config4} &= E_0 + S^2(-4J_1 - 12J_2) \\
E_{config5} &= E_0 + S^2(4J_1 - 12J_2) \\
J_1 &= (E_{config5} - E_{config4})/(8S^2) \\
J_3 &= (E_{config3} - E_{config4})/(24S^2) \\
J_2 &= (E_{FM} - E_{config2} - 48J_3)/(48S^2)
\end{aligned} \tag{4.4}
$$

The calculated results of exchange coupling constants and magnetic moments on Cr atoms are shown in Table. 4.5.

Table 4.5: Exchange coupling constants and magnetic moments in 2L Cr_7Te_{12}

	Energy (meV)
J_1	-6.29
J_2	-2.56
J_3	-2.61

Cr atom	Magnetic moment (μB)
1	3.051
2, 3, 4, 5	2.939
6, 7	3.041

The 2L Cr_7Te_{12} has the perpendicular magnetic anisotropy with an anisotropic energy $E_{MAE} = E_x - E_z$ of 0.09 meV per Cr atom.

From these results, it is found that in all the studied $Cr_{1+x}Te_2$ structures J_1 is the strongest coupling and the intercalated Cr atoms have larger magnetic moments than other Cr atoms. The overall exchange coupling in structures with multiple $CrTe_2$ layers, i.e. bulk Cr_2Te_3 and 2L Cr_7Te_{12}, are weaker than in structures with single $CrTe_2$ layer, i.e. 1L Cr_4Te_6 and Cr_5Te_6. The magnetic anisotropy in 1L Cr_4Te_6 and Cr_5Te_6 are significantly stronger than that in bulk Cr_2Te_3 and 2L Cr_7Te_{12}. Thus, the thinner films have more potential to have higher Tc than the thicker films. Bulk Cr_2Te_3 and 1L Cr_5Te_6 have inversion symmetry and they have in-plane magnetic anisotropy. 1L Cr_4Te_6 and 2L Cr_7Te_{12} do not have inversion symmetry and they have perpendicular magnetic anisotropy. Thus, the inversion symmetry could be a critical factor that affects magnetic anisotropy in the self-intercalated $Cr_{1+x}Te_2$. By contrast, the study of 1T-$CrTe_2$ in Ch. 3 shows the 1L and bulk $CrTe_2$ have different magnetic easy axes, even though the inversion symmetry exist in both of them. This indicates that the inversion symmetry dependent magnetic anisotropy is introduced by the intercalated Cr atoms.

The strain dependent exchange coupling constants for bulk Cr_2Te_3, 1L Cr_4Te_6, and 1L Cr_5Te_6 are shown in Fig. 4.7. Exchange coupling in bulk Cr_2Te_3 is not sensitive to bi-axial strain. In 1L Cr_4Te_6, J_1 is enhanced by both compressive and tensile strain, J_2 switches its sign when a compressive strain is applied, and J_3 is not sensitive to strain. In 1L Cr_5Te_6, J_2 and J_3 has similar response to strain as in 1L Cr_4Te_6, whereas J_1 increases monotonically as the strain changes from -5%(compressive) to +5%(tensile). J_1's different response to strain in 1L Cr_4Te_6 and Cr_5Te_6 is possibly related to the lack of inversion symmetry in 1L Cr_4Te_6.

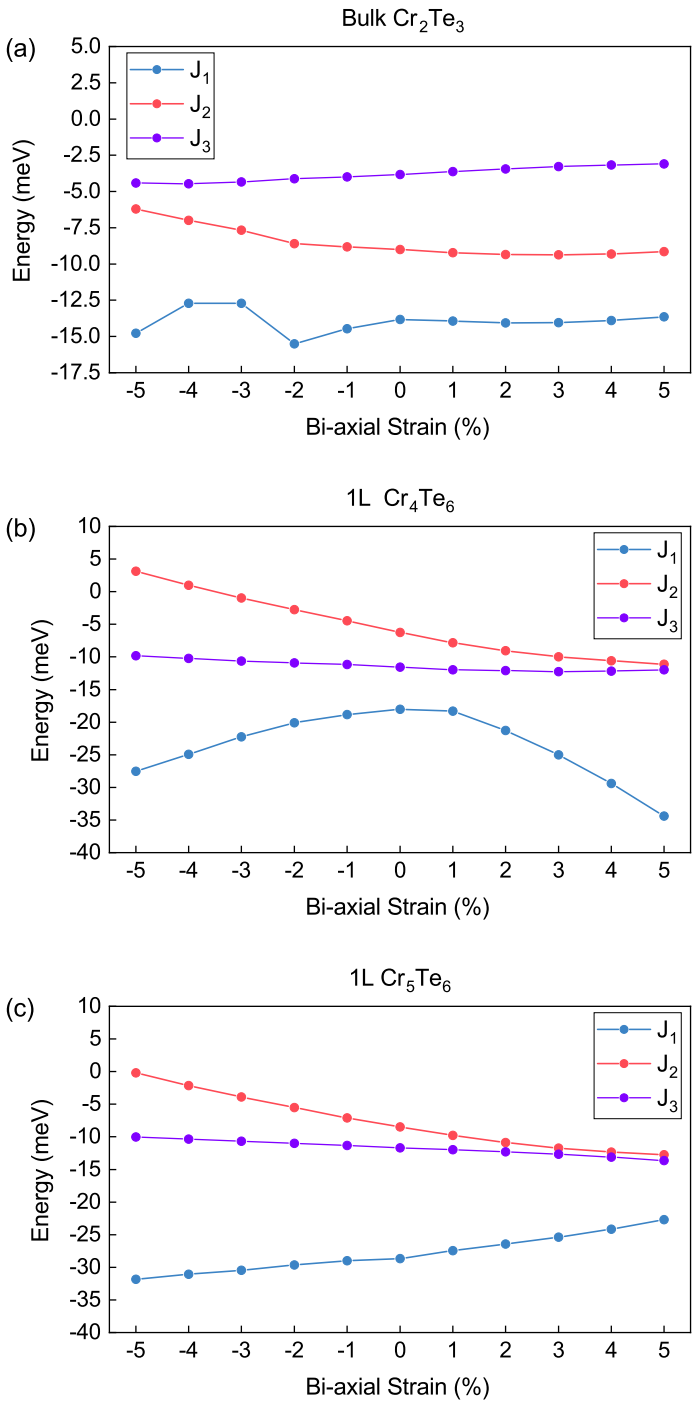

Figure 4.7: Strain dependent exchange coupling constants in bulk Cr_2Te_3, 1L Cr_4Te_6, and 1L Cr_5Te_6.

4.4 Conclusions

We have calculated the formation energy per atom in self-intercalated vdW material $Cr_{1+x}Te_2$ with different number of layers and surface type. It is found that the $Cr_{1+x}Te_2$ is more stable when both the top and bottom surfaces are $CrTe_2$ layers. The magnetic anisotropic energies have been studied by performing DFT calculation. The direction of magnetic easy axis depends on the inversion symmetry in $Cr_{1+x}Te_2$. When inversion symmetry exists, the $Cr_{1+x}Te_2$ has the in-plane magnetic anisotropy. When inversion symmetry is broken by the intercalated Cr atom on one surface, the $Cr_{1+x}Te_2$ has the perpendicular magnetic anisotropy. We have calculated the exchange coupling constants in bulk Cr_2Te_3, 1L Cr_4Te_6, Cr_5Te_6, and 2L Cr_7Te_{12}. All the exchange coupling constants in bulk Cr_2Te_3 is not sensitive to bi-axial strain. The exchange coupling constant J_1 in Cr_4Te_6 and Cr_5Te_6 respond to bi-axial strain in different ways, which is related to the different symmetries in these two structures. By comparison, the 1T-$CrTe_2$ studied in Ch. 3 does not have the inversion symmetry dependent magnetic anisotropy, which indicates the unique magnetic properties in $Cr_{1+x}Te_2$ are introduced by the intercalated Cr layers. To have more comprehensive understandings of the complex magnetism in $Cr_{1+x}Te_2$, the magnetic anisotropy in strained structures needs to be studied with the XXZ Spin Hamiltonian model that is used in Ch. 3.

4.5 Acknowledgments

This work used the Extreme Science and Engineering Discovery Environment (XSEDE) [89] which is supported by National Science Foundation Grant No. ACI-1548562 and allocation ID TG-DMR130081.

Chapter 5

Dopant's Effect on Ni Based Cathode Materials

5.1 Introduction

Li-ion batteries (LIB) have been widely used in portable electronic devices and electric vehicles. The high capacities (200 - 250 mAh g^{-1}), high-voltage operation (3.8 V vs Li_0/Li_+), and lower cost of a Ni-rich cathode make it the most promising candidate to replace the conventional $LiCoO_2$ based cathode, which has limited limited practical discharge capacity of around 170 - 180 mAhg−1 but with high cost and relative low energy density [92, 93]. However, the performance of a $LiNiO_2$ based cathode is limited by many factors: cation mixing, phase transition, lattice instability, and oxygen release, etc. Cation mixing is the presence of transition metal (TM) ions in the lithium layer. A large portion of the cation mixing in the Li layer may result in the formation of inactive $Li_2Ni_8O_{10}$, which

suppresses Li diffusion causing poor power capability. The phase transition from layered to spinel and further to rock salt is undesirable since it is always accompanied by irreversible capacity loss and volume change. During the charging process, Li^+ ions are continuously extracted from the cathode which can cause drastic shrink in the c-axis lattice parameter which is thought to be one of the factors that accelerate the rupture of active particles. The oxygen released from cathode not only affects the lattice structure, but also can cause the serious safety issue of violent exothermic reaction, i.e., explosion.

Substitutional cation doping has been pursued as a promising approach to improve the stability of $LiNiO_2$ based cathode material. For instance, Lee et al. reported that doping boron can suppress the structural degradation in $LiNi_{0.84}Co_{0.10}Mn_{0.06}O_2$ during charging [94]. Ghatak et al., found that doping Na in the Li site resists structural deformation during delithiation but decreases the energy density in a low-Co high-Ni cathod [95]. Tatsumi et al. found that Mg doping can enhance the ionic bond between O and Ni and therefore enhance the oxygen stability in $LiNiO_2$ [26]. Min et al. demonstrated that Al dopants in $LiNi_{0.8}Co_{0.1}Mn_{0.1}O_2$ (NCM811) can suppress the formation of oxygen vacancies [27]. Tina et al. observed in NCM811 that Zr, Al, and Ti dopants can improve the structural stability and electrochemical properties by decreasing the Ni/Li cation mixing [96]. They concluded that dopants with higher oxidation states and ionic radii similar to Li improve the structural and electrochemical properties.

Nevertheless, there is a lack of systematic, comprehensive theoretical studies on the properties of various dopants in $LiNiO_2$ including the preferred occupation site, dopant ion migration, and the mechanism of dopants to improve structural stability and suppress

oxygen evolution. Candidate dopants, selected based on previous experimental and theoretical investigations, include B [94], Na [95], Mg [26], Al [27, 96], Si [97], Ca [98], Ti [96, 99, 100, 28], V [100, 101], Cr [102, 103], Mn [104, 105], Fe [106, 107], Co [99, 106], Cu [108], Zn [109], Ga [101, 110], Ge [101], As, Y [111], Zr [100, 112], Nb [113, 114, 115], Mo [116], In [117], Sn [101, 118], Sb [28, 101, 119], La [120], Ce [120], Ta [96, 28, 121], and W [28, 122]. The ion migration from the Ni layer to the Li layer is most thermodynamically favored at x = 0.5 in Li_xNiO_2[123, 124, 125]. Thus, to study dopant ion migration, we use a 2×3×2 supercell of $Li_{0.5}NiO_2$ as the base model, which contains 12 Li, 24 Ni, and 48 O atoms. The chemical formula of our model can be approximated as $Li_{0.5}Ni_{0.96}D_{0.04}O_2$, where D represents the dopant species. We comprehensively investigate the preferred doping site, the dopant ion migration energy barrier, and the mechanism by which the dopant ion affects the geometry and oxygen release of the cathode.

5.2 Method

The first-principle calculations using spin-polarized density functional theory (DFT) with the projector augmented wave (PAW) [73, 74] method and a plane-wave basis are implemented in the Vienna ab initio simulation package (VASP) [67, 68]. The Perdew-Burke-Enzerhof's (PBE) [37] version of the generalized gradient approximation (GGA) is used to describe the exchange correlation density functional. A cutoff energy of 520 eV and a 4×4×4 Monkhorst-Pack k-grid mesh [80] are used for all calculations. The vdW corrections are described by the PBE+D3 method [75]. The total energy is converged within 10^{-7} eV. All lattices are fully relaxed until the force on each atom is smaller than 0.01 eV/Å. The

Methfessel-Paxton smearing method is employed with a width of 0.1 eV because Li_xNiO_2 has zero band gap. Bader analysis is employed to study the valence change and charge transfer [126, 127]. The NEB method is used to calculate the energy barriers of transition states [76, 77]. To obtain smooth energy profiles and accurate energy barriers, 7 images were interpolated between the initial and final phases. VASPKIT is used to post-process the VASP calculation result [128]. The oxygen vacancy formation energy is calculated by comparing the total energy before and after losing an oxygen atom.

5.3 Results

5.3.1 Dopant migration and preferred occupation site

To study the properties of various dopants and their effect on neighboring oxygen atoms, the first step is to determine whether the dopant ion prefers to locate in the Ni layer and be surrounded by an oxygen octahedron, i.e., octahedral site, or locate in the Li layer and be surrounded by an oxygen tetrahedron, i.e., tetrahedral site. Without knowing the preferred occupied site, we cannot correctly model the doped cathode, not to speak of obtaining reasonable simulation results.

During delithiation process, a Li vacancy forms in Li layer and the dopant is initially set at octahedral site in Ni layer in our model. The ion migration process is studied by calculating the energy along migration path from the octahedral site in Ni layer to the tetrahedral site in Li layer. The preferred occupation site can be determined by two factors, $E_{barrier}$ and ΔE, as shown in Fig. 5.1.

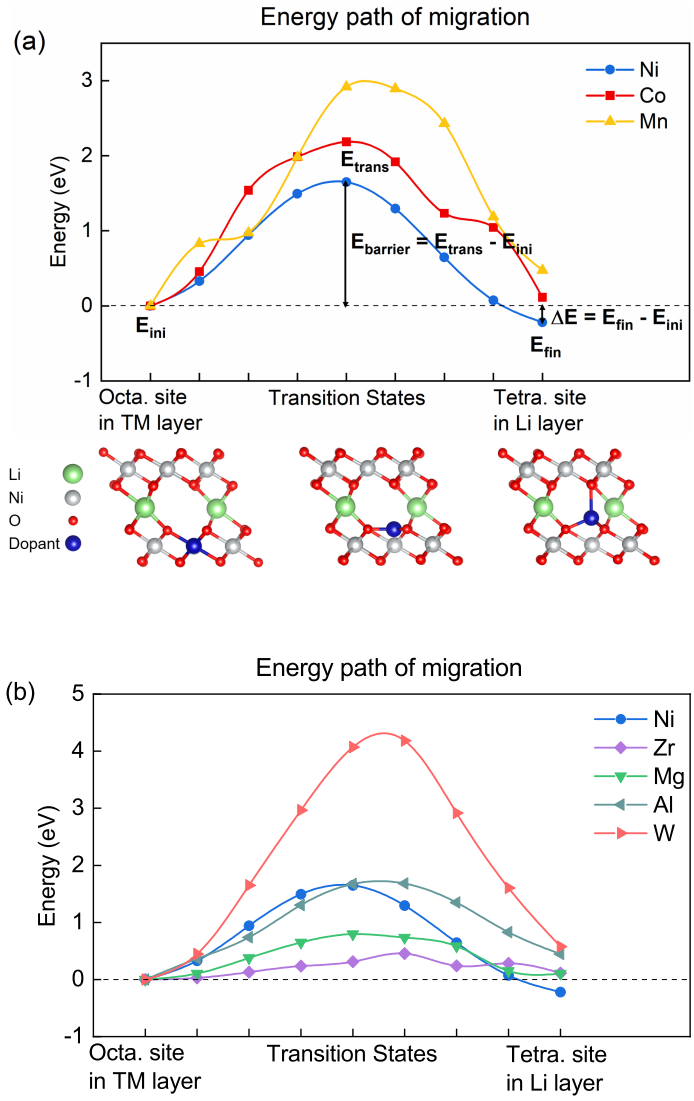

Figure 5.1: (a) Migration energy profiles of Co and Mn dopants using Ni as the undoped reference. Structures showing the initial phase (dopant ion occupies the octahedral site in TM layer), transition state phase (dopant ion passes through oxygen layer), and final phase (dopant ion occupies the tetrahedral site in Li layer) are illustrated below the plot. (b) Migration energy profiles of typical dopants, Zr, Mg, Al, and W using Ni as the undoped reference.

Table 5.1: Preferential occupation sites of various dopants in $Li_{0.5}NiO_2$

Preferential occupation site	**Dopant elements**
Octa. site in TM layer	Al, Si, Ti, V, Cr, Mn, Fe, Co, Ge, As, Nb, Mo, Sn, Sb, Ta, W
Tetra. site in Li layer	Na, Ca, Cu, Zn, Y, La, Ce, Tl
Both Octa. And Tetra. sites	Mg, Ga, Zr, In
Oxygen face center	B

The energy barrier $E_{barrier}$ is defined as the difference between the highest energy among all the transition states E_{trans} and the initial phase energy E_{ini}, i.e.

$$E_{barrier} = E_{trans} - E_{ini} \tag{5.1}$$

ΔE is the total energy change after the migration. It is defined as the energy different between the final phase and the initial phase , i.e.

$$\Delta E = E_{fin} - E_{ini} \tag{5.2}$$

The preferred occupation site is determined by the following rules:

(1) With high $E_{barrier}$ and $\Delta E > 0$, the migration is not favored at room temperature and the final phase is less stable than the initial phase. In this case, the dopant prefers to occupy the octahedral site in TM layer.

(2) With low $E_{barrier}$ and $\Delta E < 0$, the migration can happen spontaneously, and it becomes more stable after the dopant migrates. For this case, the preferred occupation site is the tetrahedral site in Li layer.

(3) With low $E_{barrier}$ and $\Delta E \approx 0$, the migration can happen when the temperature is high enough to activate it. The final phase is neither more nor less stable than the initial

phase. Thus, in this case the dopant is equally likely to exist in both the octahedral and tetrahedral sites.

In undoped $Li_{0.5}NiO_2$, $E_{barrier}$ of the Ni ion is 1.64 eV. The 3 most common TM elements used in the cathode, Ni, Co, and Mn are presented in Fig. 5.1(a). There are two reasons that Ni is more likely to migrate than Co and Mn. First, Ni has a smaller $E_{barrier}$ than the other two elements, which means that Ni ion migration can be activated by weaker thermal fluctuations. Secondly, for Ni, $\Delta E<0$, whereas for Co and Mn, $\Delta E>0$. Thus, the cathode material becomes more stable after Ni migration but less stable after Co or Mn migration.

Since Ni is well known to easily migrate from the TM layer to the Li layer, its $E_{barrier}$ is used as the threshold to measure whether a $E_{barrier}$ is high or low. The migration energy profiles of typical dopants Zr, Mg, Al, and W are plotted in Fig. 5.1(b). It is noteworthy that W has the highest energy barrier among all of the studied dopants. It was uncertain in a previous report [122] whether W prefers to stay in the TM layer or the Li layer. This result clearly shows that W strongly prefers the octahedral site in TM layer. Similarly, the calculation results showing that $E_{barrier}$ of Al is higher than that of Ni and $\Delta E>0$ are consistent with results from previous experimental studies [27, 96] finding that Al is stable in the Ni layer. In comparison, $\Delta E \approx 0$ for Mg and Zr and their values of $E_{barrier}$ are much lower than that of Ni. This indicates Mg and Zr ions can exist in both the octahedral and tetrahedral sites and migration between these sites much easier than for Ni, which is also consistent with previous studies [26, 112]. According to the three rules above, the preferred occupation sites of various dopant are summarized in Table 5.1. Rule

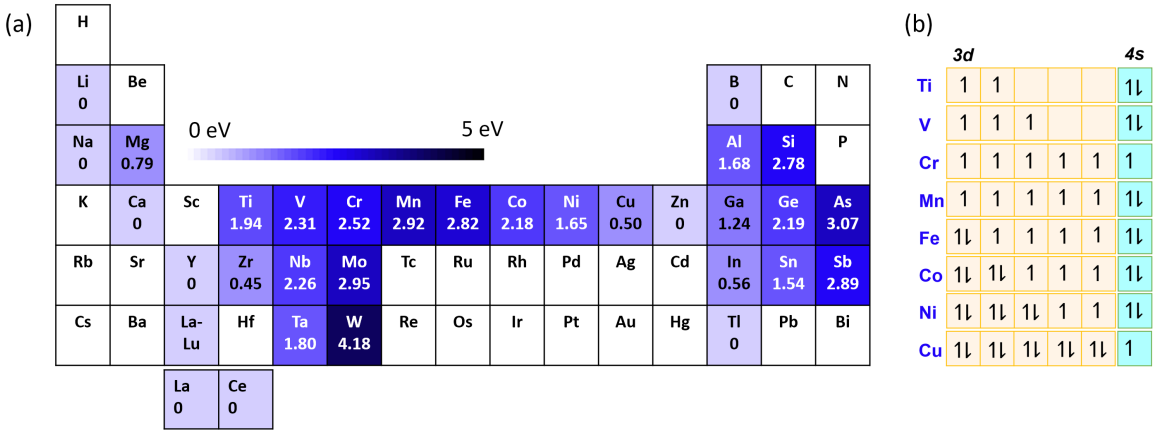

Figure 5.2: (a) Octahedral-tetrahedral migration energy barriers of dopant ions on the periodic table. (b) Valence electron orbitals of the 3d transition metal elements

No. 1 applies to Al, Si, Ti, V, Cr, Mn, Fe, Co. Ge, As, Nb, Mo, Sb, Sb, Ta, and W. Thus, these dopants prefer to occupy the octahedral site in the Ni layer. Na, Ca, Cu, Zn, Y, La, Ce, and Tl follow Rule No. 2, so these dopants occupy the tetrahedral site in the Li layer. Rule No. 3 describes the migration energy profiles of Mg, Ga, Zr, and In, which can occupy both the octahedral site in the Ni layer and the tetrahedral site in the Li layer and smoothly migrate between them. Boron is a special case: Its low $E_{barrier}$ and $\Delta E < 0$ correspond to Rule No. 2. However, boron prefers to be in the +3 state surrounded by 3 oxygen atoms, which means it only migrates to the oxygen face center and not to the tetrahedral site in the Li layer. Complete migration energy profiles of all the dopant candidates can be found in Fig. 5.8 in the **Supplementary Material** section.

To further investigate the mechanism determining the preferred occupation site, we show the studied dopants and their values for $E_{barrier}$ in the periodic table in the Fig. 5.2. Dopants with $E_{barrier} = 0$ do not stably exist in the Ni layer. During migration, the coordination number of the dopant ion starts at 6 in the octahedral site, transitions to 3 at

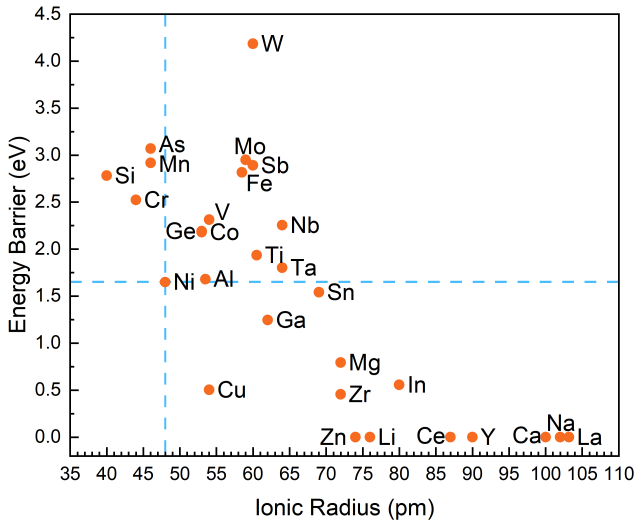

Figure 5.3: Migration energy barrier vs dopant ionic radius in $Li_{0.5}NiO_2$.

the highest energy point, and ends at 4 in the tetrahedral site. $E_{barrier}$ reflects how stable the 6-coordination structure is compared with the 3-coordinated structure. We found that the energy barrier governing dopant migration is related to the electronic structure and follows the rule of periodic table. It was believed the energy barrier to migration is related to the ionic radius. However, our calculations show the $E_{barrier}$ is not strongly correlated with the ionic radius as shown in Fig. 5.3. This is especially true for the sub-class of transition metal dopants. For the main group doping elements, $E_{barrier}$ decreases as the number of electron shells increases in the same group. This pattern can be found in (Mg, Ca), (Al, Ga, In, Tl), (Si, Ge, Sn), and (As, Sb). The reason is that for main-group elements with more electron shells, the valence **s** and **p** orbitals are far from the oxygen **2p** orbitals, which decreases the strength of the dopant-oxygen (D-O) bond leading to a lower value of $E_{barrier}$. Furthermore, $E_{barrier}$ increases as the number of electrons increase

in the same period. This pattern can be observed in (Na, Mg, Al, Si), (Ga, Ge, As), and (In, Sn, Sb). This is because more valence electrons allow for higher coordination, which stabilizes the 6-coordinated structure and increases $E_{barrier}$. For the **3d** transition metal elements, $E_{barrier}$ increases from Ti to Mn and then decreases from Mn to Zn. When a TM dopant is 6-coordinated with oxygen, only the unpaired **d** electrons can form a bond with oxygen, so $E_{barrier}$ of the TM dopant is strongly positively correlated to the number unpaired d electrons as shown in the Fig. 5.2(b). The **4d** and **5d** TM doping elements also have similar trends. The trend moving down a column of the transition metals is not clear, since $E_{barrier}$ decreases going from V to Ta, but it increases going from Cr to W.

5.3.2 Oxygen stability

Oxygen evolution is one of the main sources causing cathode instability [129]. In this process, the Ni^{3+} is reduced to Ni^{2+} and the O^{2-} in the lattice is oxidized to O^{-} simultaneously. Then, free O^{2-} and O are formed from the disproportionation reaction of O^{-}. Neutral O atoms can combine and form O_2 gas, which is also called oxygen release. This mechanism is described as follows:

$$Ni^{3+} + O^{2-}_{(\text{lattice})} = Ni^{2+} + O^{-} \tag{5.3}$$

$$2O^{-} = O^{2-}_{(\text{free})} + O \tag{5.4}$$

$$2O = O_2 \uparrow \tag{5.5}$$

To understand the effect and mechanism of various dopants on the oxygen evolution in a $LiNiO_2$ based cathode during delithiation, the oxygen vacancy formation energy $E_{vacancy}$

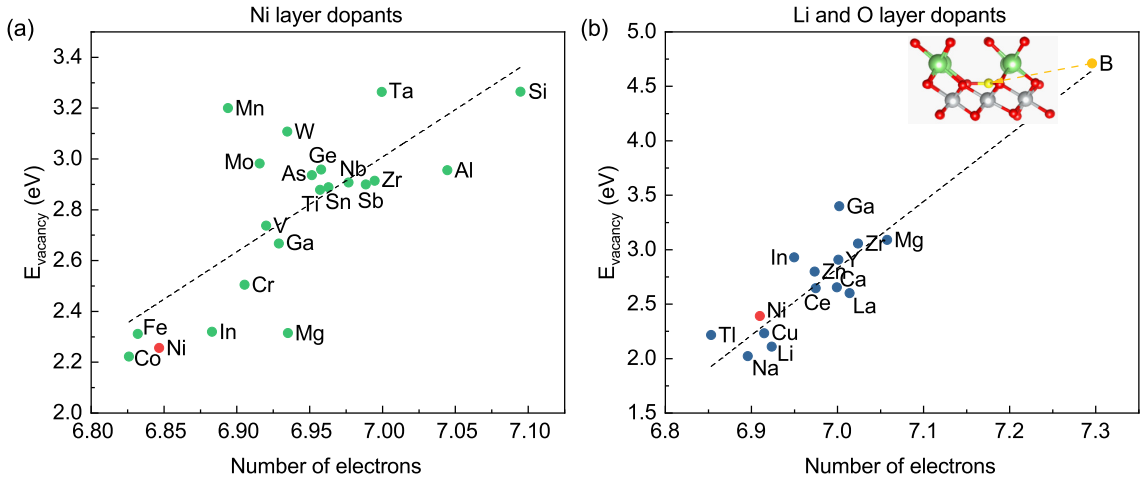

Figure 5.4: Oxygen vacancy formation energy of dopants in (a) the octahedral site in Ni layer and (b) the tetrahedral site in Li layer. The Ni element (colored in red) is used as the undoped reference. Notably boron dopant occupies the center of 3 oxygen atoms which is not in the Li layer.

is calculated by removing one oxygen atom from the supercell and determining the energy differences as shown in the following equation [25].

$$\mathrm{E_{vacancy}} = \mathrm{E(Li_{12}Ni_{23}D_1O_{47})} + \frac{1}{2}\mathrm{E(O_2)} - \mathrm{E(Li_{12}Ni_{23}D_1O_{48})} \tag{5.6}$$

The values of $E_{vacancy}$ for various dopants vs. the number of valence electrons of the oxygen atom obtained from a Bader charge analysis are plotted in the Fig. 5.4. A nearly linear correlation was found between $E_{vacancy}$ and oxygen's electron number. The valence of oxygen tends to O^{2-} with more surrounding electrons, which makes it difficult to be oxidized to a neutral O atom and form O_2 gas. Among all the dopants occupying an octahedral site in the Ni layer, Co is the worst dopant for $LiNiO_2$ in terms of oxygen stability as shown in Fig. 5.4(a). This finding supports previous studies showing that Co may be unnecessary in Ni-rich cathode materials [130, 131]. In comparison, Mn significantly enhances the oxygen stability by increasing $E_{vacancy}$ by approximately 40%. Remarkably,

boron stabilizes its neighboring oxygen atoms more than all the other dopants as shown in Fig. 5.4(b). Boron's small atomic radius (87 pm) and 3 valence electrons cause it to prefer a 3-coordinated state with oxygen atoms with strong and short B-O bonds (≈1.4 Å).

Among the 3d transition metal elements, Mn dopant has a larger $E_{vacancy}$ than others. The difference in $E_{vacancy}$ is originated from the different orbitals' response to losing oxygen atom. As shown in Fig. 5.5(a), in the undoped structure the spin-up channel of Ni **3d** orbitals shifts to higher energy but the spin-down channel shifts to lower energy after the oxygen atom is removed, which cancel each other in energy and results in a rather small $E_{vacancy}$. Co doped structure has a lower $E_{vacancy}$ than the undoped reference, which is because the Co **3d** orbitals are very insensitive to the oxygen loss, as shown in Fig. 5.5(b). By contrast, as shown in Fig. 5.5(c), in the Mn doped structure the spin-up Mn **3d** orbitals around -2 eV shift to 0.5 eV below the Fermi level after the oxygen atom is removed, which results in the large $E_{vacancy}$ of 3.2 eV.

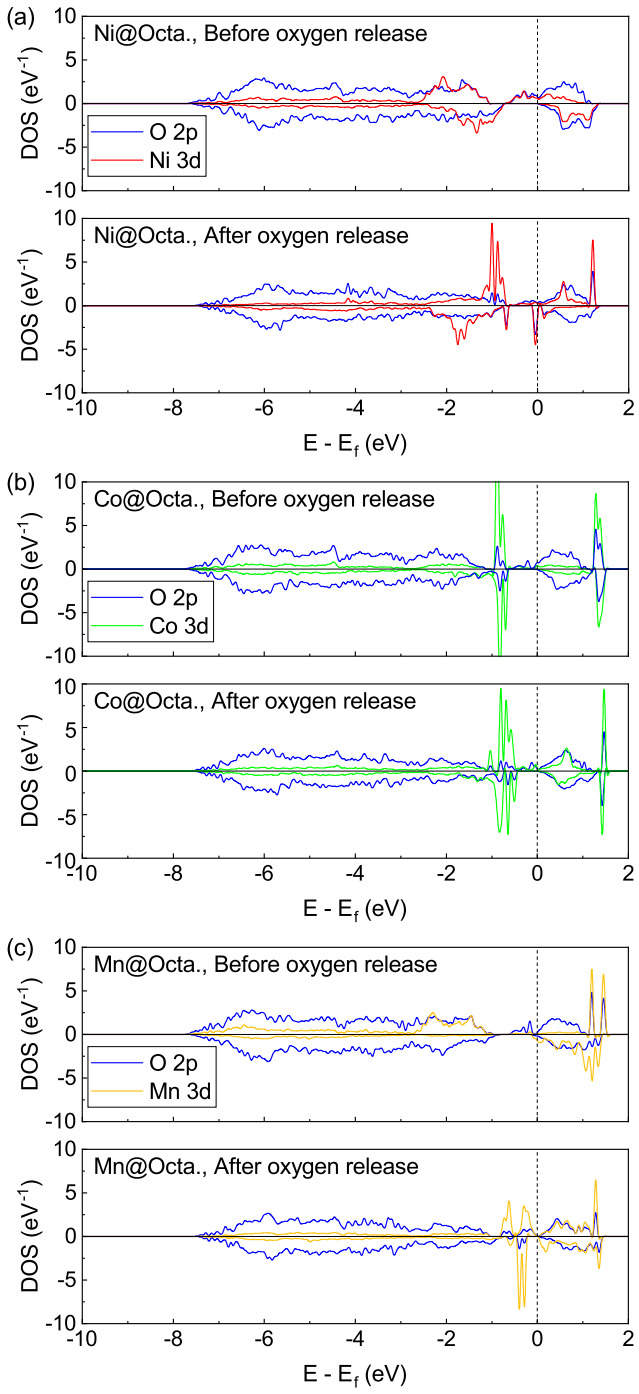

Figure 5.5: Projected density of states (PDOS) of the studied dopant (or Ni) atom and neighboring oxygen atoms in (a) undoped, (b) Co doped, and (c) Mn doped $Li_{12}Ni_{23}D_1O_{48}$ before and after one oxygen atom is removed. All studied dopant (or Ni) atoms are located at the octahedral site in the TM layer, which is denoted by @Octa.

5.3.3 Structural properties

The interlayer distance between two adjacent Ni layers is an important property affecting the Li-ion diffusion. A larger interlayer distance gives the Li ion more space and less impedance. Fig. 5.6 shows the optimized interlayer distance of $Li_{0.5}NiO_2$ with dopants occupying different sites. As shown in Fig. 5.6(a), all of the dopants occupying the octahedral site in the Ni layer shrink the interlayer distance compared to that of the undoped reference. The shrinking caused by doping is between -0.24% and -0.86%, which will not cause significant change to the layered structure. Similarly, all of the dopants occupying the tetrahedral site in the Li layer expand the interlayer distance as shown in Fig. 5.6(b). The interlayer distance expansion caused by doping with Na, La, Tl, and Ca can be more than 2%, which make them good candidates for introducing the pillar effect. Fig. 5.6(c) shows the interlayer distance with Zr, Ga, Mg, and In dopants. When occupying the octahedral site in the Ni layer, all these dopants cause the interlayer distance to shrink like the dopants that only occupy the Ni layer. Likewise, these dopants increase the interlayer distance when occupying the tetrahedral site in the Li layer similar to the other dopants that only occupy the Li layer. Therefore, the occupation site of the dopant is the key factor that determines whether the structure shrinks or expands. Fig. 5.7 shows the calculated formation energy of all the doped structures. We found most dopants decrease the formation energy, which means these dopants theoretically can be doped into the cathode material during synthesis.

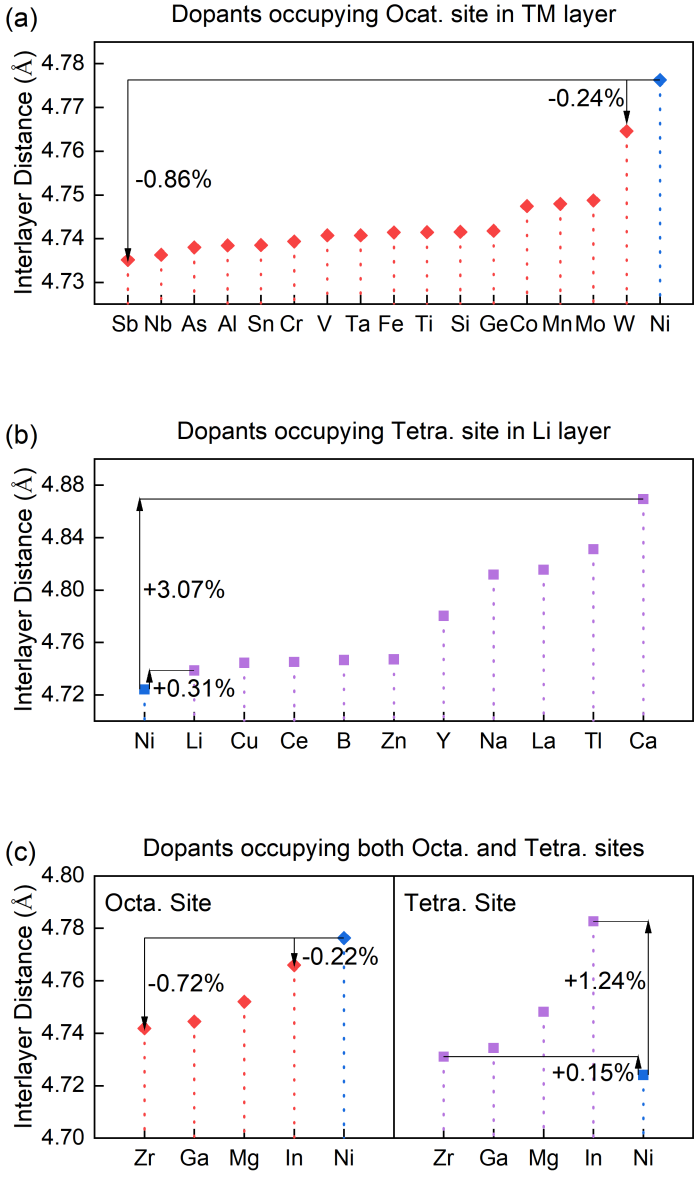

Figure 5.6: Interlayer distance between two adjacent Ni layers in $Li_{0.5}NiO_2$ with dopants occupying (a) the octahedral site in the Ni layer, (b) the tetrahedral site in Li layer, and (c) both sites with easy migration between the sites.

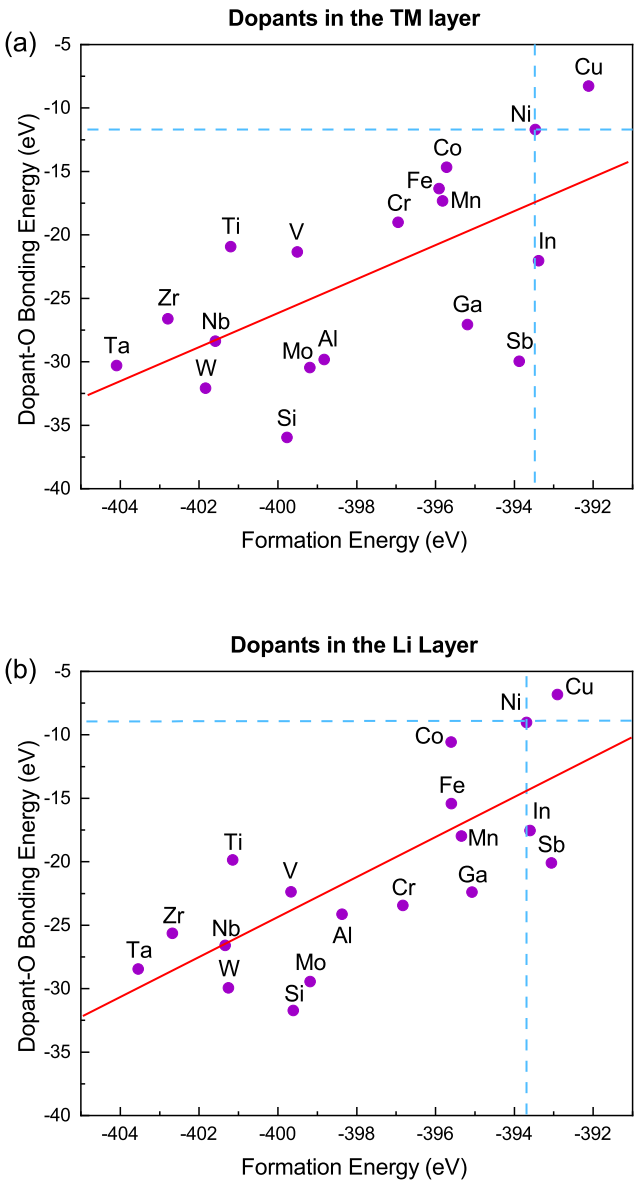

Figure 5.7: The dopant-O bonding energy and formation energy of doped $Li_{0.5}NiO_2$ with various dopants occupying (a) the octahedral site in TM layer and (b) the tetrahedral site in Li layer.

5.4 Conclusions

In summary, we investigated the dopant migration, dopants' occupation site, oxygen stability, and interlayer distance of half delithiated $Li_{0.5}NiO_2$ with various dopants using first-principles calculations. All the dopants except boron can be classified into three categories: (1) preferential occupation of the octahedral site in the Ni layer; (2) preferential occupation of the tetrahedral site in the Li layer; (3) equally probable occupation of both sites and easy migration between the sites. Boron does not fall into the three categories. It prefers to stay in the center of three oxygen atoms, i.e., 3-coordinated with oxygen. For the non-TM dopants, the migration energy barrier increases as one moves across a row of the periodic table, and it decreases as one moves down a column. For the TM dopants, the migration energy barrier is positively correlated with the number of unpaired valence electrons, and for each row of TMs, the barrier peaks near the center of the row. The oxygen vacancy formation energy is linearly correlated with the number of electrons surrounding the oxygen. Co doping damages the oxygen stability in $Li_{0.5}NiO_2$ more than that of any other dopant, so that Co is not a good doping candidate in terms of preventing oxygen release. Boron doping significantly enhances the stability of the oxygen atoms coordinated to it. The effect of a dopant on the interlayer distance is dependent on the dopant's occupation site. When occupying the Ni layer, all dopants cause the interlayer distance to shrink, and when occupying the Li layer, all dopants cause the interlayer distance to expand. This understanding of cathode doping should facilitate future work studying the promising dopant candidates and optimizing doping ratios to stabilize the structure and suppress cation mixing (Ni migration) in a $LiNiO_2$ based cathode.

5.5 Supplementary Material

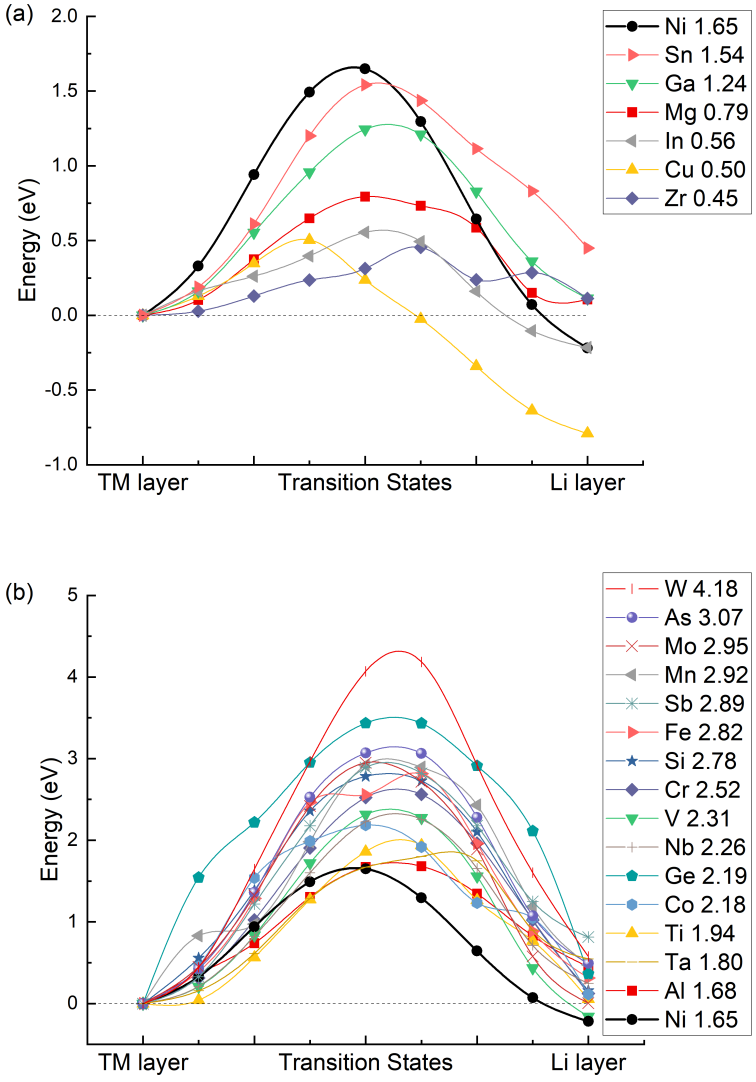

Figure 5.8: Complete migration energy profiles of all (a) dopant candidates with energy barriers lower than Ni, (b) dopant candidates with energy barriers higher than Ni.

5.6 Acknowledgments

This work used the Extreme Science and Engineering Discovery Environment (XSEDE) [89] which is supported by National Science Foundation Grant No. ACI-1548562 and allocation ID TG-DMR130081.

Chapter 6

Summary and Outlook

The critical results of this thesis are summarized as follows:

1. The calculated formation energies of $CrTe_2$ show that the 1T-$CrTe_2$ phase is the ground state. For the bulk and monolayer, the formation energy of the 1T phase lies at 0.30 eV and 0.11 eV per formula unit below the next metastable phase, respectively. The energy barriers separating the phases are large, on the order of 0.5 eV for both the bulk and monolayer. The calculated U value for the Cr atom in 1T-$CrTe_2$ is 5.8 eV. The magnetic anisotropy of 1T-$CrTe_2$ originates from the SOC of the Te atoms and the superexchange coupling between the Cr-3d and Te-5p orbitals. For any number of layers ($n \geq 2$) of 1T-$CrTe_2$, the magnetic moment lies in-plane, however for a monolayer, the magnetic moment is out-of-plane. Band filling with a sheet carrier concentration more than $n_s = 1.5 \times 10^{14}$ cm^{-2} or a tensile bi-axial strain of 3% can cause the magnetic easy axis of monolayer 1T-$CrTe_2$ to switch from out-of-plane to in-plane. A compressive bi-axial strain of -3% causes the magnetic easy axis of bilayer

1T-$CrTe_2$ to switch from in-plane to out-of-plane. PMA is favored in structures with smaller dihedral angles consistent with the trend identified previously for CrI_3. An RWST analysis using experimental values for magnetic anisotropy and T_c, provides a range of expected values for the nearest neighbor exchange constant lying between 3.1 meV and 5.2 meV for values of T_c in the range of 200 K and 300 K, respectively.

2. Our calculations show the $Cr_{1+x}Te_2$ is more stable when both the top and bottom surfaces are $CrTe_2$ layers. The magnetic anisotropic energies have been studied by performing DFT calculation. The direction of magnetic easy axis depends on the inversion symmetry in $Cr_{1+x}Te_2$. When inversion symmetry exists, the $Cr_{1+x}Te_2$ has the in-plane magnetic anisotropy. When inversion symmetry is broken by the intercalated Cr atom on one surface, the $Cr_{1+x}Te_2$ has the perpendicular magnetic anisotropy. We have calculated the exchange coupling constants in bulk Cr_2Te_3, 1L Cr_4Te_6, Cr_5Te_6, and 2L Cr_7Te_{12}. All the exchange coupling constants in bulk Cr_2Te_3 is not sensitive to bi-axial strain. The exchange coupling constant J_1 in Cr_4Te_6 and Cr_5Te_6 respond to bi-axial strain in different ways, which is related to the different symmetries in these two structures. By comparison, the 1T-$CrTe_2$ studied in Ch. 3 does not have the inversion symmetry dependent magnetic anisotropy, which indicates the unique magnetic properties in $Cr_{1+x}Te_2$ are introduced by the intercalated Cr layers. To have more comprehensive understandings of the complex magnetism in $Cr_{1+x}Te_2$, the magnetic anisotropy in strained structures needs to be studied with the XXZ Spin Hamiltonian model that is used in Ch. 3.

3. The dopant migration, dopant occupation site, oxygen stability, and interlayer dis-

tance of half delithiated $Li_{0.5}NiO_2$ with various dopants are investigated by using first-principles calculations. All the dopants except boron can be classified into three categories: (1) preferential occupation of the octahedral site in the Ni layer; (2) preferential occupation of the tetrahedral site in the Li layer; (3) equally probable occupation of both sites and easy migration between the sites. Boron does not fall into the three categories. It prefers to stay in the center of three oxygen atoms, i.e., 3-coordinated with oxygen. For the non-TM dopants, the migration energy barrier increases as one moves across a row of the periodic table, and it decreases as one moves down a column. For the TM dopants, the migration energy barrier is positively correlated with the number of unpaired valence electrons, and for each row of TMs, the barrier peaks near the center of the row. The oxygen vacancy formation energy is linearly correlated with the number of electrons surrounding the oxygen. Co doping damages the oxygen stability in $Li_{0.5}NiO_2$ more than that of any other dopant, thus Co is not a good doping candidate in terms of preventing oxygen release. Boron doping significantly enhances the stability of the oxygen atoms coordinated to it. The effect of a dopant on the interlayer distance is dependent on the dopant's occupation site. When occupying the Ni layer, all dopants cause the interlayer distance to shrink, and when occupying the Li layer, all dopants cause the interlayer distance to expand. This understanding of cathode doping should facilitate future work studying the promising dopant candidates and optimizing doping ratios to stabilize the structure and suppress cation mixing (Ni migration) in a $LiNiO_2$ based cathode.

Chapter 7

Appendices

7.1 Codes for modeling doped $Li_{0.5}NiO_2$

1. The python code for replacing one Ni atom with the dopant atom

```
import numpy as np
# Define a distance function
print("Creating POSCAR, the Li tri-vacancy is created, one Ni atom
    is replaced by dopant atom")
def dist(i, j, pos):
    distance = np.sqrt((pos[i][0] - pos[j][0])** 2 + (pos[i][1] -
        pos[j][1])** 2 + (pos[i][2] - pos[j][2])** 2)
    return distance

print("Input the file name of your supercell POSCAR/CONTCAR:")
inputfile = input()

```

```
with open(inputfile,'r') as file:
    CONTCAR = file.readlines() # Read the whole file
    elements = CONTCAR[5].split() # Read the line of elements
    num_of_elements = CONTCAR[6].split() # Read the line of number
       of atoms for each element
    for i in range(len(num_of_elements)):
        num_of_elements[i] = int(num_of_elements[i])
    print("Elements  ",elements)
    print("Number of atoms  ",num_of_elements)
    total_num = 0
    for num in num_of_elements:
        total_num += num
    print(total_num,"atoms in total")

    # Get lattice vectors
    base_vector = [0] * 3
    for i in range(3):
        base_vector[i] = CONTCAR[2+i].split()
    for i in range(3):
        for j in range(3):
            base_vector[i][j] = float(base_vector[i][j])
    base_vector = np.array(base_vector)

    # Read all atomic positions
    position = [[0.0,0.0,0.0]] * total_num
```

```
35      for i in range(total_num):
36          position[i] = CONTCAR[i + 8].split()
37      rows = len(position)
38      cols = 3
39      for i in range(rows):
40          for j in range(cols):
41              position[i][j] = float(position[i][j])
42          # Make all the atoms in the range from -0.25 to 0.9 in x,
              y, z
43      for i in range(rows):
44          if (position[i][0] > 0.9):
45              position[i][0] -= 1
46          if (position[i][1] > 0.9):
47              position[i][1] -= 1
48          if (position[i][2] > 0.9):
49              position[i][2] -= 1
50      for i in range(rows):
51          if (position[i][0] < -0.25):
52              position[i][0] += 1
53          if (position[i][1] < -0.25):
54              position[i][1] += 1
55          if (position[i][2] < -0.25):
56              position[i][2] += 1
57      position = np.array(position)
58      position_Direct = position
```

```
59      position = np.dot(position, base_vector)
60  #     print("Position: ")
61  #     for i in range(len(position)):
62  #         print(i+8)
63  #         print(position[i])
64      # Search the Ni atom, dopant site, Li-tricancy site
65      Ni_index = 0
66      NN_Ni_index = 0 # The nearest negihbor of the Ni that will be
            studied, we will change this Ni to dopant element
67      NN_Ni_dist = 10
68
69      # locate the Ni site at (0 0 0)
70      for i in range(rows):
71          if (abs(position[i][0]) < 0.1) and (abs(position[i][1]) <
                0.1) and (abs(position[i][2]) < 0.1):
72              Ni_index = i
73
74      # locate the nearest neighbor Ni site
75      for i in range(rows):
76          if (position[i][0] > 0) and (position[i][1] > 0) and
                (abs(position[i][2]) < 0.01) and (i != Ni_index): #The
                Ni sites on the 001 plane
77              if dist(i,Ni_index,position) < NN_Ni_dist:
78                  NN_Ni_dist = dist(i, Ni_index,position)
79                  NN_Ni_index = i
```

```
80      print("The TM atom being studied is the atom No.",
            Ni_index+1,"The index should not be 1")
81      print("The TM atom being changed to dopant is No.",
            NN_Ni_index+1)
82
83      # Search the position of Li-trivacancy
84      NN_Li_index = 0;
85      NN_Li_dist = 10;
86      for i in range(num_of_elements[0]):
87          if (position[i][2] >= 0):
88              if (dist(i, Ni_index, position) < NN_Li_dist):
89                  NN_Li_dist = dist(i, Ni_index, position)
90                  NN_Li_index = i
91      print("The Li atom being moved to create a Li-trivacancy is
            No.", NN_Li_index+1)
92      print("The cartesian position of this Li atom
            is",position[NN_Li_index])
93      Li_x_index = 1000
94      Li_x_dist = 10
95      Li_y_index = 1000
96      Li_y_dist = 10
97      for i in range(num_of_elements[0]):
98          if (i != NN_Li_index):
99              if (abs(position[i][2] - position[NN_Li_index][2]) <
                    0.2):
```

```
100                 if (position[i][0] > position[NN_Li_index][0]) and
                        (abs(position[i][1] - position[NN_Li_index][1])
                        < 0.1):
101                     if ((position[i][0] - position[NN_Li_index][0])
                            < Li_x_dist):
102                         Li_x_index = i;
103                         Li_x_dist = position[i][0] -
                                position[NN_Li_index][0]
104                 if (position[i][1] > position[NN_Li_index][1]) and
                        (abs(position[i][0] - position[NN_Li_index][0] <
                        0.1)):
105                     if ((position[i][1] -
                            position[NN_Li_index][1])) < Li_y_dist:
106                         Li_y_index = i;
107                         Li_y_dist = position[i][1] -
                                position[NN_Li_index][1]
108     print("The Li atom No.", NN_Li_index+1, "is being moved to the
            middle of No.",Li_x_index+1,"and No.",Li_y_index+1)
109     print("The cartesian
            positions:",position[Li_x_index],position[Li_y_index])
110     position_Direct[NN_Li_index] = (position_Direct[Li_x_index] +
            position_Direct[Li_y_index])/2
111
112 ## Output part
113 print("Please input the dopant element:",end=" ")
```

```
dopant = input()
output_filename = inputfile + "_int_"+dopant
with open(output_filename,'w') as output:
    title = CONTCAR[:5]
    new_elements = list()
    new_elements.append(elements[0])
    num_before_dopant = NN_Ni_index+1 - num_of_elements[0]-1
    new_num_of_elements = list()
    new_num_of_elements.append(num_of_elements[0])
    if (num_before_dopant == 0):
        new_elements.append(dopant)
        new_elements.append(elements[1])
        new_elements.append(elements[2])
        new_num_of_elements.append(1)
        new_num_of_elements.append(num_of_elements[1] - 1)
        new_num_of_elements.append(num_of_elements[2])
    elif (num_before_dopant != 0):
        new_elements.append(elements[1])
        new_elements.append(dopant)
        new_elements.append(elements[1])
        new_elements.append(elements[2])
        new_num_of_elements.append(num_before_dopant)
        new_num_of_elements.append(1)
        new_num_of_elements.append(num_of_elements[1] - 1 -
            num_before_dopant)
```

```
        new_num_of_elements.append(num_of_elements[2])
    output.writelines(title)
    output.write("    ")
    for element in new_elements:
        output.write(element)
        output.write("   ")
    output.write("\n")
    output.write("    ")
    for num in new_num_of_elements:
        output.write(str(num))
        output.write("   ")
    output.write('\n')
    output.write("Direct\n")
    for i in range(rows):
        for j in range(cols):
            output.write("     ")
            output.write(str(format(position_Direct[i][j], '.8f')))
            output.write("     ")
        output.write('\n')
    print("Work Done!")
    print("The result is stored in ",output_filename)
```

2. The python code for creating POSCARs with dopant occupying the oxygen face center and tetrahedral site in the Li layer respectively.

```
import numpy as np
```

```
# Define a distance function
print("Creating 2 POSCARs, 1: dopant atom is located at the face
    center of 3 oxygen atoms. 2: dopant atom is located at the
    tetrahedral site.")
def dist(i, j, pos):
    distance = np.sqrt((pos[i][0] - pos[j][0])** 2 + (pos[i][1] -
        pos[j][1])** 2 + (pos[i][2] - pos[j][2])** 2)
    return distance
print("Input the file name of your POSCAR/CONTCAR:")
inputfile = input()
with open(inputfile,'r') as file:
    CONTCAR = file.readlines() # Read the whole file
    elements = CONTCAR[5].split() # Read the line of elements
    num_of_elements = CONTCAR[6].split() # Read the line of number
        of atoms for each element
    for i in range(len(num_of_elements)):
        num_of_elements[i] = int(num_of_elements[i])
    print("Elements  ",elements)
    print("Number of atoms  ",num_of_elements)
    total_num = 0
    for num in num_of_elements:
        total_num += num
    print(total_num,"atoms in total")

    # Get lattice vectors
```

```
23      base_vector = [0] * 3
24      for i in range(3):
25          base_vector[i] = CONTCAR[2+i].split()
26      for i in range(3):
27          for j in range(3):
28              base_vector[i][j] = float(base_vector[i][j])
29      base_vector = np.array(base_vector)
30
31      # Read all atomic positions
32      position = [[0.0,0.0,0.0]] * total_num
33      for i in range(total_num):
34          position[i] = CONTCAR[i + 8].split()
35      rows = len(position)
36      cols = len(position[0])
37      for i in range(rows):
38          for j in range(cols):
39              position[i][j] = float(position[i][j])
40          # Make all the atoms in the range from -0.7 to 0.7 in x, y,
              z
41      for i in range(rows):
42          if (position[i][0] > 0.7):
43              position[i][0] -= 1
44          if (position[i][1] > 0.7):
45              position[i][1] -= 1
46          if (position[i][2] > 0.9):
```

```
47              position[i][2] -= 1
48      for i in range(rows):
49          if (position[i][0] < -0.7):
50              position[i][0] += 1
51          if (position[i][1] < -0.7):
52              position[i][1] += 1
53          if (position[i][2] < -0.9):
54              position[i][2] += 1
55      position = np.array(position)
56      position_Direct = position
57      position = np.dot(position, base_vector)
58
59      # Search the Ni atom, dopant site, Li-tricancy site
60      Ni_index = 0
61      NN_Ni_index = 0 # The nearest negihbor of the Ni that will be
            studied, we will change this Ni to dopant element
62      NN_Ni_dist = 10
63
64      # locate the Ni site at (0 0 0)
65      for i in range(rows):
66
67          if (abs(position[i][0]) < 1) and (abs(position[i][1]) < 1)
                and (abs(position[i][2]) < 1):
68              Ni_index = i
69
```

```
70      # Search the 4 Oxygen atoms by sorting the distance to the
            studied Ni site
71      print("Ni atom No.",Ni_index+1,'!!The index cannot be 1')
72      O1_index = 0
73      O2_index = 0
74      O3_index = 0
75      O4_index = 0
76      O_dist = list()
77      for i in range(num_of_elements[-1]):
78          if(position[i+total_num-num_of_elements[-1]][2] > 0 ):
79              O_dist.append([dist(i+total_num-num_of_elements[-1],
80              Ni_index,position),
81              i+total_num-num_of_elements[-1]])
82      O_dist.sort()
83      O1_index = O_dist[0][1]
84      O2_index = O_dist[1][1]
85      O3_index = O_dist[2][1]
86      print("The 3 Oxygen atoms forming a face:")
87      print(O1_index+1)
88      print(O2_index+1)
89      print(O3_index+1)
90      O_dist = list()
91      for i in range(num_of_elements[-1]):
92          if(abs(position[i+total_num-num_of_elements[-1]][1]) < 0.5
93          and abs(position[i+total_num-num_of_elements[-1]][0]) < 0.5
```

```
94          and position[i+total_num-num_of_elements[-1]][2] > 0 ):
95              O_dist.append([dist(i+total_num-num_of_elements[-1],
96              Ni_index,position),
97              i+total_num-num_of_elements[-1]])
98      O_dist.sort()
99      O4_index = O_dist[0][1]
100     print("The 4th Oxygen atoms forming a tetrahedron with the
            frist 3 Oxygen atoms:")
101     print(O4_index+1)
102     face_pos = (position_Direct[O1_index] +
            position_Direct[O2_index] + position_Direct[O3_index])/3
103     print("The fractional position of face center
            is:(",format(face_pos[0],'.8f'),
104     format(face_pos[1],'.8f'),format(face_pos[2],'.8f'),')')
105     tetra_pos = (position_Direct[O1_index] +
            position_Direct[O2_index] + position_Direct[O3_index] +
            position_Direct[O4_index])/4
106     print("The fractional position of tetra-site
            is:(",format(tetra_pos[0],'.8f'),
107     format(tetra_pos[1],'.8f'),format(tetra_pos[2],'.8f'),')')
108     Car_face_pos = (position[O1_index] + position[O2_index] +
            position[O3_index])/3
109     print("The cartesian position of face center
            is:(",format(Car_face_pos[0],'.8f'),
110     format(Car_face_pos[1],'.8f'),format(Car_face_pos[2],'.8f'),')',
```

```
111     'it should be around 0.9')
112     Car_tetra_pos = (position[O1_index] + position[O2_index] +
            position[O3_index] + position[O4_index])/4
113     print("The cartesian position of tetra-site
            is:(",format(Car_tetra_pos[0],'.8f'),
114          format(Car_tetra_pos[1],'.8f'),
115          format(Car_tetra_pos[2],'.8f'),')',
116          'it should be around 1.7')
117
118 #Output the POSCARs
119 output_face = inputfile + "_face"
120 with open(output_face,'w') as face:
121    face.writelines(CONTCAR[:8])
122    position_Direct[Ni_index] = face_pos
123    for i in range(rows):
124        for j in range(cols):
125            face.write("    ")
126            face.write(str(format(position_Direct[i][j], '.8f')))
127            face.write("    ")
128        face.write('\n')
129 output_tetra = inputfile + "_tetra"
130 with open(output_tetra,'w') as tetra:
131     tetra.writelines(CONTCAR[:8])
132     position_Direct[Ni_index] = tetra_pos
133     for i in range(rows):
```

```
134         for j in range(cols):
135             tetra.write("    ")
136             tetra.write(str(format(position_Direct[i][j], '.8f')))
137             tetra.write("    ")
138         tetra.write('\n')
```

Bibliography

[1] Yuhang Liu, Sohee Kwon, George J. de Coster, Roger K. Lake, and Mahesh R. Neupane. Structural, electronic, and magnetic properties of $crte_2$. *Phys. Rev. Materials*, 6:084004, Aug 2022.

[2] K. S. Novoselov, A. K. Geim, S. V. Morozov, D. Jiang, Y. Zhang, S. V. Dubonos, I. V. Grigorieva, and A. A. Firsov. Electric field effect in atomically thin carbon films. *Science*, 306(5696):666–669, 2004.

[3] K. S. Novoselov, A. Mishchenko, A. Carvalho, and A. H. Castro Neto. 2d materials and van der waals heterostructures. *Science*, 353(6298):aac9439, 2016.

[4] Igor Žutić, Jaroslav Fabian, and S. Das Sarma. Spintronics: Fundamentals and applications. *Rev. Mod. Phys.*, 76:323–410, Apr 2004.

[5] Magnetic Gibertini, Maciej Koperski, Alberto F Morpurgo, and Konstantin S Novoselov. Magnetic 2d materials and heterostructures. *Nature nanotechnology*, 14(5):408–419, 2019.

[6] Kin Fai Mak, Jie Shan, and Daniel C Ralph. Probing and controlling magnetic states in 2d layered magnetic materials. *Nature Reviews Physics*, 1(11):646–661, 2019.

[7] N. D. Mermin and H. Wagner. Absence of ferromagnetism or antiferromagnetism in one- or two-dimensional isotropic Heisenberg models. *Phys. Rev. Lett.*, 17(22):1133–1136, 1966.

[8] Hui Li, Shuangchen Ruan, and Yu-Jia Zeng. Intrinsic van der waals magnetic materials from bulk to the 2d limit: New frontiers of spintronics. *Advanced Materials*, 31(27):1900065, 2019.

[9] Bevin Huang, Genevieve Clark, Efrén Navarro-Moratalla, Dahlia R Klein, Ran Cheng, Kyle L Seyler, Ding Zhong, Emma Schmidgall, Michael A McGuire, David H Cobden, et al. Layer-dependent ferromagnetism in a van der waals crystal down to the monolayer limit. *Nature*, 546(7657):270–273, 2017.

[10] Tiancheng Song, Zaiyao Fei, Matthew Yankowitz, Zhong Lin, Qianni Jiang, Kyle Hwangbo, Qi Zhang, Bosong Sun, Takashi Taniguchi, Kenji Watanabe, et al. Switching 2d magnetic states via pressure tuning of layer stacking. *Nature materials*, 18(12):1298–1302, 2019.

[11] Tingxin Li, Shengwei Jiang, Nikhil Sivadas, Zefang Wang, Yang Xu, Daniel Weber, Joshua E Goldberger, Kenji Watanabe, Takashi Taniguchi, Craig J Fennie, et al. Pressure-controlled interlayer magnetism in atomically thin cri3. *Nature materials*, 18(12):1303–1308, 2019.

[12] Daniele C Freitas, Ruben Weht, André Sulpice, Gyorgy Remenyi, Pierre Strobel, Frédéric Gay, Jacques Marcus, and Manuel Núñez-Regueiro. Ferromagnetism in layered metastable 1T-$CrTe_2$. *Journal of Physics: Condensed Matter*, 27(17):176002, apr 2015.

[13] Xingdan Sun, Wanying Li, Xiao Wang, Qi Sui, Tongyao Zhang, Zhi Wang, Long Liu, Da Li, Shun Feng, Siyu Zhong, et al. Room temperature ferromagnetism in ultra-thin van der waals crystals of 1T-$CrTe_2$. *Nano Research*, 13(12):3358–3363, 2020.

[14] Yao Wen, Zhehong Liu, Yu Zhang, Congxin Xia, Baoxing Zhai, Xinhui Zhang, Guihao Zhai, Chao Shen, Peng He, Ruiqing Cheng, Lei Yin, Yuyu Yao, Marshet Getaye Sendeku, Zhenxing Wang, Xubing Ye, Chuansheng Liu, Chao Jiang, Chongxin Shan, Youwen Long, and Jun He. Tunable room-temperature ferromagnetism in two-dimensional Cr2Te3. *Nano Letters*, 20(5):3130–3139, 2020. PMID: 32338924.

[15] Y. Fujisawa, M. Pardo-Almanza, J. Garland, K. Yamagami, X. Zhu, X. Chen, K. Araki, T. Takeda, M. Kobayashi, Y. Takeda, C. H. Hsu, F. C. Chuang, R. Laskowski, K. H. Khoo, A. Soumyanarayanan, and Y. Okada. Tailoring magnetism in self-intercalated $Cr_{1+\delta}Te_2$ epitaxial films. *Phys. Rev. Materials*, 4:114001, Nov 2020.

[16] Meng Huang, Zongwei Ma, Sheng Wang, Si Li, Miao Li, Junxiang Xiang, Ping Liu, Guojing Hu, Zengming Zhang, Zhe Sun, Yalin Lu, Zhigao Sheng, Gong Chen, Yu-Lun Chueh, Shengyuan A Yang, and Bin Xiang. Significant perpendicular magnetic anisotropy in room-temperature layered ferromagnet of cr-intercalated CrTe2. *2D Materials*, 8(3):031003, may 2021.

[17] Hongxi Li, Linjing Wang, Junshu Chen, Tao Yu, Liang Zhou, Yang Qiu, Hongtao He, Fei Ye, Iam Keong Sou, and Gan Wang. Molecular beam epitaxy grown cr2te3 thin films with tunable curie temperatures for spintronic devices. *ACS Applied Nano Materials*, 2(11):6809–6817, 2019.

[18] In Hak Lee, Byoung Ki Choi, Hyuk Jin Kim, Min Jay Kim, Hu Young Jeong, Jong Hoon Lee, Seung-Young Park, Younghun Jo, Chanki Lee, Jun Woo Choi, Seong Won Cho, Suyoun Lee, Younghak Kim, Beom Hyun Kim, Kyeong Jun Lee, Jin Eun Heo, Seo Hyoung Chang, Fengping Li, Bheema Lingam Chittari, Jeil Jung, and Young Jun Chang. Modulating curie temperature and magnetic anisotropy in

nanoscale-layered cr2te3 films: Implications for room-temperature spintronics. *ACS Applied Nano Materials*, 4(5):4810–4819, 2021.

[19] Luo-Zhao Zhang, An-Lei Zhang, Xiu-De He, Xin-Wei Ben, Qi-Ling Xiao, Wen-Lai Lu, Fei Chen, Zhenjie Feng, Shixun Cao, Jincang Zhang, and Jun-Yi Ge. Critical behavior and magnetocaloric effect of the quasi-two-dimensional room-temperature ferromagnet Cr_4Te_5. *Phys. Rev. B*, 101:214413, Jun 2020.

[20] Yu Liu, Milinda Abeykoon, Eli Stavitski, Klaus Attenkofer, and C. Petrovic. Magnetic anisotropy and entropy change in trigonal cr_5te_8. *Phys. Rev. B*, 100:245114, Dec 2019.

[21] Yihao Wang, Jian Yan, Junbo Li, Shasha Wang, Meng Song, Jiangpeng Song, Zhihao Li, Ke Chen, Yongliang Qin, Langsheng Ling, Haifeng Du, Liang Cao, Xuan Luo, Yimin Xiong, and Yuping Sun. Magnetic anisotropy and topological hall effect in the trigonal chromium tellurides cr_5te_8. *Phys. Rev. B*, 100:024434, Jul 2019.

[22] Luo-Zhao Zhang, Xiu-De He, An-Lei Zhang, Qi-Ling Xiao, Wen-Lai Lu, Fei Chen, Zhenjie Feng, Shixun Cao, Jincang Zhang, and Jun-Yi Ge. Tunable curie temperature in layered ferromagnetic cr5+xte8 single crystals. *APL Materials*, 8(3):031101, 2020.

[23] Guixin Cao, Qiang Zhang, Matthias Frontzek, Weiwei Xie, Dongliang Gong, George E. Sterbinsky, and Rongying Jin. Structure, chromium vacancies, and magnetism in a $Cr_{12-x}Te_{16}$ compound. *Phys. Rev. Materials*, 3:125001, Dec 2019.

[24] M. E. Arroyo y de Dompablo, A. Van der Ven, and G. Ceder. First-principles calculations of lithium ordering and phase stability on li_xnio_2. *Phys. Rev. B*, 66:064112, Aug 2002.

[25] Fantai Kong, Chaoping Liang, Luhua Wang, Yongping Zheng, Sahila Perananthan, Roberto C. Longo, John P. Ferraris, Moon Kim, and Kyeongjae Cho. Kinetic stability of bulk linio2 and surface degradation by oxygen evolution in linio2-based cathode materials. *Advanced Energy Materials*, 9(2):1802586, 2019.

[26] Kazuyoshi Tatsumi, Yusuke Sasano, Shunsuke Muto, Tomoko Yoshida, Tsuyoshi Sasaki, Kayo Horibuchi, Yoji Takeuchi, and Yoshio Ukyo. Local atomic and electronic structures around mg and al dopants in $linio_2$ electrodes studied by xanes and elnes and first-principles calculations. *Phys. Rev. B*, 78:045108, Jul 2008.

[27] Kyoungmin Min, Seung-Woo Seo, You Young Song, Hyo Sug Lee, and Eunseog Cho. A first-principles study of the preventive effects of al and mg doping on the degradation in lini0.8co0.1mn0.1o2 cathode materials. *Phys. Chem. Chem. Phys.*, 19:1762–1769, 2017.

[28] Jianli Cheng, Linqin Mu, Chunyang Wang, Zhijie Yang, Huolin L. Xin, Feng Lin, and Kristin A. Persson. Enhancing surface oxygen retention through theory-guided doping selection in li1-xnio2 for next-generation lithium-ion batteries. *J. Mater. Chem. A*, 8:23293–23303, 2020.

[29] P. Hohenberg and W. Kohn. Inhomogeneous electron gas. *Phys. Rev.*, 136:B864–B871, Nov 1964.

[30] W. Kohn and L. J. Sham. Self-consistent equations including exchange and correlation effects. *Phys. Rev.*, 140:A1133–A1138, Nov 1965.

[31] P. A. M. Dirac. Note on exchange phenomena in the thomas atom. *Mathematical Proceedings of the Cambridge Philosophical Society*, 26(3):376–385, 1930.

[32] Murray Gell-Mann and Keith A. Brueckner. Correlation energy of an electron gas at high density. *Phys. Rev.*, 106:364–368, Apr 1957.

[33] W. J. Carr and A. A. Maradudin. Ground-state energy of a high-density electron gas. *Phys. Rev.*, 133:A371–A374, Jan 1964.

[34] E. Wigner. On the interaction of electrons in metals. *Phys. Rev.*, 46:1002–1011, Dec 1934.

[35] J. P. Perdew and Alex Zunger. Self-interaction correction to density-functional approximations for many-electron systems. *Phys. Rev. B*, 23:5048–5079, May 1981.

[36] D. M. Ceperley and B. J. Alder. Ground state of the electron gas by a stochastic method. *Phys. Rev. Lett.*, 45:566–569, Aug 1980.

[37] John P. Perdew, Kieron Burke, and Matthias Ernzerhof. Generalized gradient approximation made simple. *Phys. Rev. Lett.*, 77:3865–3868, Oct 1996.

[38] John P. Perdew and Yue Wang. Accurate and simple analytic representation of the electron-gas correlation energy. *Phys. Rev. B*, 45:13244–13249, Jun 1992.

[39] S. L. Dudarev, G. A. Botton, S. Y. Savrasov, C. J. Humphreys, and A. P. Sutton. Electron-energy-loss spectra and the structural stability of nickel oxide: An LSDA+U study. *Phys. Rev. B*, 57:1505–1509, Jan 1998.

[40] E. Abate and M. Asdente. Tight-binding calculation of $3d$ bands of fe with and without spin-orbit coupling. *Phys. Rev.*, 140:A1303–A1308, Nov 1965.

[41] Bevin Huang, Genevieve Clark, Efrén Navarro-Moratalla, Dahlia R. Klein, Ran Cheng, Kyle L. Seyler, Ding Zhong, Emma Schmidgall, Michael A. McGuire, David H. Cobden, Wang Yao, Di Xiao, Pablo Jarillo-Herrero, and Xiaodong Xu. Layer-dependent ferromagnetism in a van der Waals crystal down to the monolayer limit. *Nature*, 546(7657):270–273, 2017.

[42] Cheng Gong, Lin Li, Zhenglu Li, Huiwen Ji, Alex Stern, Yang Xia, Ting Cao, Wei Bao, Chenzhe Wang, Yuan Wang, Z. Q. Qiu, R. J. Cava, Steven G. Louie, Jing Xia, and Xiang Zhang. Discovery of intrinsic ferromagnetism in two-dimensional van der Waals crystals. *Nature*, 546(7657):265–269, 2017.

[43] In Jun Park, Sohee Kwon, and Roger K. Lake. Effects of filling, strain, and electric field on the Néel vector in antiferromagnetic CrSb. *Phys. Rev. B*, 102:224426, Dec 2020.

[44] Lucas Webster and Jia-An Yan. Strain-tunable magnetic anisotropy in monolayer $CrCl_3$, $CrBr_3$, and CrI_3. *Phys. Rev. B*, 98:144411, Oct 2018.

[45] Yan Song, Xiaocha Wang, and Wenbo Mi. Role of electron filling in the magnetic anisotropy of monolayer WSe_2 doped with 5*d* transition metals. *Phys. Rev. Materials*, 1:074408, Dec 2017.

[46] Xiangru Kong, Hongkee Yoon, Myung Joon Han, and Liangbo Liang. Switching interlayer magnetic order in bilayer CrI_3 by stacking reversal. *Nanoscale*, 13:16172–16181, 2021.

[47] Yufang Xie, Ye Yuan, Magdalena Birowska, Chenhui Zhang, Lei Cao, Mao Wang, Joerg Grenzer, Dominik Kriegner, Petr Doležal, Yu-Jia Zeng, Xixiang Zhang, Manfred Helm, Shengqiang Zhou, and Slawomir Prucnal. Strain-induced switching between noncollinear and collinear spin configuration in magnetic Mn_5Ge_3 films. *Phys. Rev. B*, 104:064416, Aug 2021.

[48] Meiling Xu, Chengxi Huang, Yinwei Li, Siyu Liu, Xin Zhong, Puru Jena, Erjun Kan, and Yanchao Wang. Electrical control of magnetic phase transition in a Type-I multiferroic double-metal trihalide monolayer. *Phys. Rev. Lett.*, 124:067602, Feb 2020.

[49] Hua Wang, Jingshan Qi, and Xiaofeng Qian. Electrically tunable high curie temperature two-dimensional ferromagnetism in van der Waals layered crystals. *Applied Physics Letters*, 117(8):083102, 2020.

[50] Kyle L. Seyler, Ding Zhong, Bevin Huang, Xiayu Linpeng, Nathan P. Wilson, Takashi Taniguchi, Kenji Watanabe, Wang Yao, Di Xiao, Michael A. McGuire, Kai-Mei C. Fu, and Xiaodong Xu. Valley manipulation by optically tuning the magnetic proximity effect in WSe_2/CrI_3 heterostructures. *Nano Letters*, 18(6):3823–3828, 2018.

[51] Jieyi Liu and Thorsten Hesjedal. Magnetic topological insulator heterostructures: A review. *Advanced Materials*, page 2102427, 2021.

[52] Mauro Och, Marie-Blandine Martin, Bruno Dlubak, Pierre Seneor, and Cecilia Mattevi. Synthesis of emerging 2D layered magnetic materials. *Nanoscale*, 13:2157–2180, 2021.

[53] C. Ataca, H. Sahin, and S. Ciraci. Stable, single-layer MX_2 transition-metal oxides and dichalcogenides in a honeycomb-like structure. *The Journal of Physical Chemistry C*, 116(16):8983–8999, 2012.

[54] Hongyan Guo, Ning Lu, Lu Wang, Xiaojun Wu, and Xiao Cheng Zeng. Tuning electronic and magnetic properties of early transition-metal dichalcogenides via tensile strain. *The Journal of Physical Chemistry C*, 118(13):7242–7249, 2014.

[55] Xiaoqian Zhang, Qiangsheng Lu, Wenqing Liu, Wei Niu, Jiabao Sun, Jacob Cook, Mitchel Vaninger, Paul F Miceli, David J Singh, Shang-Wei Lian, et al. Room-temperature intrinsic ferromagnetism in epitaxial $CrTe_2$ ultrathin films. *Nature communications*, 12:2492, 2021.

[56] Lingjia Meng, Zhang Zhou, Mingquan Xu, Shiqi Yang, Kunpeng Si, Lixuan Liu, Xingguo Wang, Huaning Jiang, Bixuan Li, Peixin Qin, et al. Anomalous thickness dependence of curie temperature in air-stable two-dimensional ferromagnetic 1T-$CrTe_2$ grown by chemical vapor deposition. *Nature communications*, 12:809, 2021.

[57] Yizhe Sun, Pengfei Yan, Jiai Ning, Xiaoqian Zhang, Yafei Zhao, Qinwu Gao, Moorthi Kanagaraj, Kunpeng Zhang, Jingjing Li, Xianyang Lu, Yu Yan, Yao Li, Yongbing Xu, and Liang He. Ferromagnetism in two-dimensional crte2 epitaxial films down to a few atomic layers. *AIP Advances*, 11(3):035138, 2021.

[58] Carlos M. O. Bastos, Rafael Besse, Juarez L. F. Da Silva, and Guilherme M. Sipahi. Ab initio investigation of structural stability and exfoliation energies in transition metal dichalcogenides based on Ti-, V-, and Mo-group elements. *Phys. Rev. Materials*, 3:044002, Apr 2019.

[59] Jing-Jing Xian, Cong Wang, Jin-Hua Nie, Rui Li, Mengjiao Han, Junhao Lin, Wen-Hao Zhang, Zhen-Yu Liu, Zhi-Mo Zhang, Mao-Peng Miao, Yangfan Yi, Shiwei Wu, Xiaodie Chen, Junbo Han, Zhengcai Xia, Wei Ji, and Ying-Shuang Fu. Spin mapping of intralayer antiferromagnetism and field-induced spin reorientation in monolayer crte2. *Nature Communications*, 13(1):257, 2022.

[60] H. Y. Lv, W. J. Lu, D. F. Shao, Y. Liu, and Y. P. Sun. Strain-controlled switch between ferromagnetism and antiferromagnetism in 1T-$CrTe_2$ (X=Se, Te) monolayers. *Phys. Rev. B*, 92:214419, Dec 2015.

[61] Karlheinz Schwarz and Peter Blaha. Solid state calculations using WIEN2k. *Computational Materials Science*, 28(2):259–273, 2003. Proceedings of the Symposium on Software Development for Process and Materials Design.

[62] Adolfo Otero Fumega, Jan Phillips, and Victor Pardo. Controlled two-dimensional ferromagnetism in 1T-$CrTe_2$: The role of charge density wave and strain. *The Journal of Physical Chemistry C*, 124(38):21047–21053, 2020.

[63] Si Li, Shan-Shan Wang, Bo Tai, Weikang Wu, Bin Xiang, Xian-Lei Sheng, and Shengyuan A. Yang. Tunable anomalous hall transport in bulk and two-dimensional 1T-$CrTe_2$: A first-principles study. *Phys. Rev. B*, 103:045114, Jan 2021.

[64] Aolin Li, Wenzhe Zhou, Shenglin Peng, Yunpeng Wang, Mengqiu Long, and Fangping Ouyang. Half-metallicity and enhanced magnetism in monolayer 1T-$CrTe_2$ by lithium adsorption. *Physics Letters A*, 394:127195, 2021.

[65] Pengfei Gao, Xingxing Li, and Jinlong Yang. Thickness dependent magnetic transition in few layer 1T phase $CrTe_2$. *The Journal of Physical Chemistry Letters*, 12(29):6847–6851, 2021.

[66] Ji ří Klimeš, David R. Bowler, and Angelos Michaelides. Van der waals density functionals applied to solids. *Phys. Rev. B*, 83:195131, May 2011.

[67] G. Kresse and J. Furthmüller. Efficient iterative schemes for ab initio total-energy calculations using a plane-wave basis set. *Phys. Rev. B*, 54:11169–11186, Oct 1996.

[68] G. Kresse and J. Hafner. Ab initio molecular dynamics for liquid metals. *Phys. Rev. B*, 47:558–561, Jan 1993.

[69] Qiu-Qiu Li, Si Li, Dan Wu, Zhong-Ke Ding, Xuan-Hao Cao, Lin Huang, Hui Pan, Bo Li, Ke-Qiu Chen, and Xi-Dong Duan. Magnetic properties manipulation of $CrTe_2$ bilayer through strain and self-intercalation. *Applied Physics Letters*, 119(16):162402, 2021.

[70] J. L. Lado and J. Fernández-Rossier. On the origin of magnetic anisotropy in two dimensional CrI_3. *2D Materials*, 4(3):035002, jun 2017.

[71] Dong-Hwan Kim, Kyoo Kim, Kyung-Tae Ko, JunHo Seo, Jun Sung Kim, Tae-Hwan Jang, Younghak Kim, Jae-Young Kim, Sang-Wook Cheong, and Jae-Hoon Park. Giant magnetic anisotropy induced by ligand ls coupling in layered Cr compounds. *Phys. Rev. Lett.*, 122:207201, May 2019.

[72] Micheline Bloch. Magnon renormalization in ferromagnets near the Curie point. *Phys. Rev. Lett.*, 9(7):286–287, 1962.

[73] P. E. Blöchl. Projector augmented-wave method. *Phys. Rev. B*, 50:17953–17979, Dec 1994.

[74] G. Kresse and D. Joubert. From ultrasoft pseudopotentials to the projector augmented-wave method. *Phys. Rev. B*, 59:1758–1775, Jan 1999.

[75] Stefan Grimme, Jens Antony, Stephan Ehrlich, and Helge Krieg. A consistent and accurate ab initio parametrization of density functional dispersion correction (DFT-D) for the 94 elements H-Pu. *The Journal of Chemical Physics*, 132(15):154104, 2010.

[76] Graeme Henkelman, Blas P. Uberuaga, and Hannes Jonsson. A climbing image nudged elastic band method for finding saddle points and minimum energy paths. *The Journal of Chemical Physics*, 113(22):9901–9904, 2000.

[77] Xin Chen, Yuhang Liu, and Biplab Sanyal. Manipulation of electronic and magnetic properties of 3d transition metal (Cr, Mn, Fe) hexamers on graphene with vacancy defects: Insights from first-principles theory. *The Journal of Physical Chemistry C*, 124(7):4270–4278, 2020.

[78] Matteo Cococcioni and Stefano de Gironcoli. Linear response approach to the calculation of the effective interaction parameters in the LDA + U method. *Phys. Rev. B*, 71:035105, Jan 2005.

[79] Junyi Liu, Qiang Sun, Yoshiyuki Kawazoe, and Puru Jena. Exfoliating biocompatible ferromagnetic Cr-trihalide monolayers. *Phys. Chem. Chem. Phys.*, 18(13):8777–8784, 2016.

[80] Hendrik J. Monkhorst and James D. Pack. Special points for brillouin-zone integrations. *Phys. Rev. B*, 13:5188–5192, Jun 1976.

[81] Liangxu Lin, Peter Sherrell, Yuqing Liu, Wen Lei, Shaowei Zhang, Haijun Zhang, Gordon G. Wallace, and Jun Chen. Engineered 2D transition metal dichalcogenides-a vision of viable hydrogen evolution reaction catalysis. *Advanced Energy Materials*, 10(16):1903870, 2020.

[82] Maria S. Sokolikova and Cecilia Mattevi. Direct synthesis of metastable phases of 2D transition metal dichalcogenides. *Chem. Soc. Rev.*, 49(12):3952–3980, 2020.

[83] Jun Chang, Jize Zhao, and Yang Ding. Anisotropic superexchange through nonmagnetic anions with spin-orbit coupling. *The European Physical Journal B*, 93(8):159, Aug 2020.

[84] E. E. Reinehr and W. Figueiredo. Anisotropic heisenberg ferromagnetic model in two dimensions. *Phys. Rev. B*, 52:310–312, Jul 1995.

[85] T. Holstein and H. Primakoff. Field dependence of the intrinsic domain magnetization of a ferromagnet. *Phys. Rev.*, 58:1098–1113, 1940.

[86] Daniel Stanek, Oleg P. Sushkov, and Götz S. Uhrig. Self-consistent spin-wave theory for a frustrated Heisenberg model with biquadratic exchange in the columnar phase and its application to iron pnictides. *Phys. Rev. B*, 84:064505, Aug 2011.

[87] M. T. Johnson, P. J. H. Bloemen, F. J. A. den Broeder, and J. J. de Vries. Magnetic anisotropy in metallic multilayers. *Reports on Progress in Physics*, 59(11):1409–1458, nov 1996.

[88] Xiaobo Lu, Ruixiang Fei, and Li Yang. Curie temperature of emerging two-dimensional magnetic structures. *Phys. Rev. B*, 100:205409, Nov 2019.

[89] John Towns, Timothy Cockerill, Maytal Dahan, Ian Foster, Kelly Gaither, Andrew Grimshaw, Victor Hazlewood, Scott Lathrop, Dave Lifka, Gregory D. Peterson, Ralph Roskies, J. Ray Scott, and Nancy Wilkins-Diehr. XSEDE: Accelerating scientific discovery. *Computing in Science Engineering*, 16(5):62–74, 2014.

[90] S Mangin, D Ravelosona, JA Katine, MJ Carey, BD Terris, and Eric E Fullerton. Current-induced magnetization reversal in nanopillars with perpendicular anisotropy. *Nature materials*, 5(3):210–215, 2006.

[91] Naoki Nishimura, Tadahiko Hirai, Akio Koganei, Takashi Ikeda, Kazuhisa Okano, Yoshinobu Sekiguchi, and Yoshiyuki Osada. Magnetic tunnel junction device with perpendicular magnetization films for high-density magnetic random access memory. *Journal of Applied Physics*, 91(8):5246–5249, 2002.

[92] Qi Liu, Xin Su, Dan Lei, Yan Qin, Jianguo Wen, Fangmin Guo, Yimin A Wu, Yangchun Rong, Ronghui Kou, Xianghui Xiao, et al. Approaching the capacity limit of lithium cobalt oxide in lithium ion batteries via lanthanum and aluminium doping. *Nature Energy*, 3(11):936–943, 2018.

[93] Jiaxun Zhang, Peng-Fei Wang, Panxing Bai, Hongli Wan, Sufu Liu, Singyuk Hou, Xiangjun Pu, Jiale Xia, Weiran Zhang, Zeyi Wang, Bo Nan, Xiyue Zhang, Jijian Xu, and Chunsheng Wang. Interfacial design for a 4.6 v high-voltage single-crystalline licoo2 cathode. *Advanced Materials*, 34(8):2108353, 2022.

[94] Seung-Hwan Lee, Bong-Soo Jin, and Hyun-Soo Kim. Superior performances of b-doped lini0. 84co0. 10mn0. 06o2 cathode for advanced libs. *Scientific Reports*, 9(1):1–7, 2019.

[95] Kamalika Ghatak, Swastik Basu, Tridip Das, Vidushi Sharma, Hemant Kumar, and Dibakar Datta. Effect of cobalt content on the electrochemical properties and structural stability of nca type cathode materials. *Phys. Chem. Chem. Phys.*, 20:22805–22817, 2018.

[96] Tina Weigel, Florian Schipper, Evan M. Erickson, Francis Amalraj Susai, Boris Markovsky, and Doron Aurbach. Structural and electrochemical aspects of lini0.8co0.1mn0.1o2 cathode materials doped by various cations. *ACS Energy Letters*, 4(2):508–516, 2019.

[97] Bo Zong, Ziyao Deng, Shuhao Yan, Yaqiang Lang, Jiajia Gong, Jianling Guo, Li Wang, and Guangchuan Liang. Effects of si doping on structural and electrochemical performance of lini0.5mn1.5o4 cathode materials for lithium-ion batteries. *Powder Technology*, 364:725–737, 2020.

[98] Chiwei Wang, Xiaoling Ma, Jinguo Cheng, Liqun Zhou, Jutang Sun, and Yunhong Zhou. Effects of ca doping on the electrochemical properties of lini0.8co0.2o2 cathode material. *Solid State Ionics*, 177(11):1027–1031, 2006.

[99] B.V.R Chowdari, G.V Subba Rao, and S.Y Chow. Cathodic behavior of (co, ti, mg)-doped linio2. *Solid State Ionics*, 140(1):55–62, 2001.

[100] Chaoping Liang, Fantai Kong, Roberto C. Longo, Chenxi Zhang, Yifan Nie, Yongping Zheng, and Kyeongjae Cho. Site-dependent multicomponent doping strategy for ni-rich lini1-2ycoymnyo2 (y = 1/12) cathode materials for li-ion batteries. *J. Mater. Chem. A*, 5:25303–25313, 2017.

[101] Yan-Hui Chen, Jing Zhang, Yu-Rong Ren, Yi Li, Yong-Fan Zhang, Shu-Ping Huang, Wei Lin, and Wen-Kai Chen. Understanding the role of various dopant metals (sb, sn, ga, ge, and v) in the structural and electrochemical performances of lini0.5co0.2mn0.3o2. *The Journal of Physical Chemistry C*, 125(36):19600–19608, 2021.

[102] Sung Bin Park, Won Sob Eom, Won Il Cho, and Ho Jang. Electrochemical properties of lini0.5mn1.5o4 cathode after cr doping. *Journal of Power Sources*, 159(1):679–684, 2006.

[103] S. Zhang, C. Deng, B.L. Fu, S.Y. Yang, and L. Ma. Effects of cr doping on the electrochemical properties of li2fesio4 cathode material for lithium-ion batteries. *Electrochimica Acta*, 55(28):8482–8489, 2010.

[104] Tao Xu, Fanghui Du, Ling Wu, Zhongxu Fan, Lina Shen, and Junwei Zheng. Boosting the electrochemical performance of linio2 by extra low content of mn-doping and its mechanism. *Electrochimica Acta*, 417:140345, 2022.

[105] Yongseon Kim. First principles investigation of the structure and stability of linio2 doped with co and mn. *Journal of materials science*, 47(21):7558–7563, 2012.

[106] C.P. Laisa, A.K. Nanda Kumar, S. Selva Chandrasekaran, P. Murugan, N. Lakshminarasimhan, R. Govindaraj, and K. Ramesha. A comparative study on electrochemical cycling stability of lithium rich layered cathode materials li1.2ni0.13m0.13mn0.54o2 where m = fe or co. *Journal of Power Sources*, 324:462–474, 2016.

[107] Kaiyue Zhu, Tao Wu, Yue Zhu, Xuning Li, Mingrun Li, Ruifeng Lu, Junhu Wang, Xuefeng Zhu, and Weishen Yang. Layered fe-substituted linio2 electrocatalysts for high-efficiency oxygen evolution reaction. *ACS Energy Letters*, 2(7):1654–1660, 2017.

[108] Xiang-Ze Kong, Dong-Lin Li, Katja Lahtinen, Tanja Kallio, and Xu-Qiang Ren. Effect of copper-doping on linio2 positive electrode for lithium-ion batteries. *Journal of The Electrochemical Society*, 167(14):140545, nov 2020.

[109] Zehao Cui, Qiang Xie, and Arumugam Manthiram. Zinc-doped high-nickel, low-cobalt layered oxide cathodes for high-energy-density lithium-ion batteries. *ACS Applied Materials & Interfaces*, 13(13):15324–15332, 2021. PMID: 33760578.

[110] David Kitsche, Simon Schweidler, Andrey Mazilkin, Holger Geßwein, François Fauth, Emmanuelle Suard, Pascal Hartmann, Torsten Brezesinski, Jürgen Janek, and Matteo Bianchini. The effect of gallium substitution on the structure and electrochemical performance of linio2 in lithium-ion batteries. *Mater. Adv.*, 1:639–647, 2020.

[111] Yanwen TIAN, Xiaoxue KANG, Liying LIU, Chaqing XU, and Tao QU. Research on cathode material of li-ion battery by yttrium doping. *Journal of Rare Earths*, 26(2):279–283, 2008.

[112] Florian Schipper, Mudit Dixit, Daniela Kovacheva, Michael Talianker, Ortal Haik, Judith Grinblat, Evan M. Erickson, Chandan Ghanty, Dan T. Major, Boris Markovsky, and Doron Aurbach. Stabilizing nickel-rich layered cathode materials by a high-charge cation doping strategy: zirconium-doped lini0.6co0.2mn0.2o2. *J. Mater. Chem. A*, 4:16073–16084, 2016.

[113] Tomohiro Yoshida, Kenta Hongo, and Ryo Maezono. First-principles study of structural transitions in linio2 and high-throughput screening for long life battery. *The Journal of Physical Chemistry C*, 123(23):14126–14131, 2019.

[114] Qi Hao, Fanghui Du, Tao Xu, Qun Zhou, Haishang Cao, Zhongxu Fan, Chengxiang Mei, and Junwei Zheng. Evaluation of nb-doping on performance of linio2 in wide temperature range. *Journal of Electroanalytical Chemistry*, 907:116034, 2022.

[115] Guo-Xin Huang, Ruo-Heng Wang, Xiao-Yan Lv, Jing Su, Yun-Fei Long, Zu-Zeng Qin, and Yan-Xuan Wen. Effect of niobium doping on structural stability and electrochemical properties of linio2 cathode for li-ion batteries. *Journal of The Electrochemical Society*, 169(4):040533, apr 2022.

[116] Jin-Hwan Park, Jinsub Lim, Jaegu Yoon, Kyu-Sung Park, Jihyeon Gim, Jinju Song, Hyosun Park, Dongmin Im, Minsik Park, Docheon Ahn, Younkee Paik, and Jaekook Kim. The effects of mo doping on 0.3li[li0.33mn0.67]o2·0.7li[ni0.5co0.2mn0.3]o2 cathode material. *Dalton Trans.*, 41:3053–3059, 2012.

[117] Z. Su, Z.W. Lu, X.P. Gao, P.W. Shen, X.J. Liu, and J.Q. Wang. Preparation and electrochemical properties of indium- and sulfur-doped limno2 with orthorhombic structure as cathode materials. *Journal of Power Sources*, 189(1):411–415, 2009. Selected Papers presented at the 14th INTERNATIONAL MEETING ON LITHIUM BATTERIES (IMLB-2008).

[118] Xiaoling Ma, Chiwei Wang, Jinguo Cheng, and Jutang Sun. Effects of sn doping on the structural and electrochemical properties of lini0.8co0.2o2 cathode materials. *Solid State Ionics*, 178(1):125–129, 2007.

[119] Zhenhua Yang, Zhijuan Zhang, Yanjun Pan, Shu Zhao, Yunqing Huang, Xianyou Wang, Xiaoying Chen, and Shuangying Wei. First-principles investigation of the effects of sb doping on the linio2. *Journal of Solid State Chemistry*, 244:52–60, 2016.

[120] Fanghua Ning, Bo Xu, Jing Shi, Musheng Wu, Yinquan Hu, and Chuying Ouyang. Structural, electronic, and li migration properties of re-doped (re = ce, la) licoo2 for li-ion batteries: A first-principles investigation. *The Journal of Physical Chemistry C*, 120(33):18428–18434, 2016.

[121] Binbin Chu, Siyang Liu, Longzhen You, Da Liu, Tao Huang, Yangxing Li, and Aishui Yu. Enhancing the cycling stability of ni-rich lini0.6co0.2mn0.2o2 cathode at a high cutoff voltage with ta doping. *ACS Sustainable Chemistry & Engineering*, 8(8):3082–3090, 2020.

[122] Hoon-Hee Ryu, Geon-Tae Park, Chong S. Yoon, and Yang-Kook Sun. Suppressing detrimental phase transitions via tungsten doping of linio2 cathode for next-generation lithium-ion batteries. *J. Mater. Chem. A*, 7:18580–18588, 2019.

[123] J. Reed, G. Ceder, and A. Van Der Ven. Layered-to-spinel phase transition in lixmno2. *Electrochemical and Solid-State Letters*, 4(6):A78, 2001.

[124] Gerbrand Ceder and Anton Van der Ven. Phase diagrams of lithium transition metal oxides: investigations from first principles. *Electrochimica Acta*, 45(1):131–150, 1999.

[125] C. Wolverton and Alex Zunger. First-principles prediction of vacancy order-disorder and intercalation battery voltages in li_xcoo_2. *Phys. Rev. Lett.*, 81:606–609, Jul 1998.

[126] W Tang, E Sanville, and G Henkelman. A grid-based bader analysis algorithm without lattice bias. *Journal of Physics: Condensed Matter*, 21(8):084204, jan 2009.

[127] Min Yu and Dallas R. Trinkle. Accurate and efficient algorithm for bader charge integration. *The Journal of Chemical Physics*, 134(6):064111, 2011.

[128] Vei Wang, Nan Xu, Jin-Cheng Liu, Gang Tang, and Wen-Tong Geng. Vaspkit: A user-friendly interface facilitating high-throughput computing and analysis using vasp code. *Computer Physics Communications*, 267:108033, 2021.

[129] H. S. Liu, Z. R. Zhang, Z. L. Gong, and Y. Yang. Origin of deterioration for LiNiO[sub 2] cathode material during storage in air. *Electrochemical and Solid-State Letters*, 7(7):A190, 2004.

[130] Hongyang Li, Marc Cormier, Ning Zhang, Julie Inglis, Jing Li, and J. R. Dahn. Is cobalt needed in ni-rich positive electrode materials for lithium ion batteries? *Journal of The Electrochemical Society*, 166(4):A429–A439, 2019.

[131] Tongchao Liu, Lei Yu, Jiajie Liu, Jun Lu, Xuanxuan Bi, Alvin Dai, Matthew Li, Maofan Li, Zongxiang Hu, Lu Ma, et al. Understanding co roles towards developing co-free ni-rich cathodes for rechargeable batteries. *Nature Energy*, 6(3):277–286, 2021.

[132] Fariborz Kargar, Ece A. Coleman, Subhajit Ghosh, Jonathan Lee, Michael J. Gomez, Yuhang Liu, Andres Sanchez Magana, Zahra Barani, Amirmahdi Mohammadzadeh, Bishwajit Debnath, Richard B. Wilson, Roger K. Lake, and Alexander A. Balandin. Phonon and thermal properties of quasi-two-dimensional $FePS_3$ and $MnPS_3$ antiferromagnetic semiconductors. *ACS Nano*, 14(2):2424–2435, 2020. PMID: 31951116.

[133] Soner Steiner, Sergii Khmelevskyi, Martijn Marsmann, and Georg Kresse. Calculation of the magnetic anisotropy with projected-augmented-wave methodology and the case study of disordered $fe_{1-x}co_x$ alloys. *Phys. Rev. B*, 93:224425, Jun 2016.

[134] Xiao-Liang Qi and Shou-Cheng Zhang. Topological insulators and superconductors. *Rev. Mod. Phys.*, 83:1057–1110, Oct 2011.

[135] Weidong Luo and Xiao-Liang Qi. Massive dirac surface states in topological insulator/magnetic insulator heterostructures. *Phys. Rev. B*, 87:085431, Feb 2013.

[136] Kenneth S Burch, David Mandrus, and Je-Geun Park. Magnetism in two-dimensional van der waals materials. *Nature*, 563(7729):47–52, 2018.

[137] Cheng Gong and Xiang Zhang. Two-dimensional magnetic crystals and emergent heterostructure devices. *Science*, 363(6428):eaav4450, 2019.